Journal of Materials Chemistry A

ROYAL SOCIETY OF CHEMISTRY

REVIEW

View Article Online
View Journal | View Issue

Cite this: J. Mater. Chem. A, 2023, 11, 512

3D fibrous aerogels from 1D polymer nanofibers for energy and environmental applications

Guodong Zhao,[ab] Lei Shi,[b] Guang Yang, [b] Xupin Zhuang [*ab] and Bowen Cheng*[c]

Aerogels are highly porous structures produced by replacing the liquid solvent of a gel with air without causing the collapse of the solid network. Recently, 1D polymer nanofibers have been widely researched as building blocks to develop a new species of 3D fibrous aerogels with a physically entangled and/or chemically crosslinked fibrous network. 3D fibrous aerogels not only hold intrinsic aerogel properties such as an open-cell pore structure, low density, high specific surface area, and large porosity, but also benefit from the inherent features of polymer nanofibers including excellent mechanical flexibility and toughness, a wide range of material selection, and additional functionality. In this review, recent research progress in the fabrication and application of 3D fibrous aerogels is systematically summarized. Relevant strategies for constructing 3D fibrous aerogels, including electrospinning, solution blow spinning, freeze-drying, thermally induced self-agglomeration, and carbonization, are presented. Typical applications in energy (*e.g.*, pressure sensors, triboelectric nanogenerators, electromagnetic interference shielding, *etc.*) and the environment (*e.g.*, air filtration, thermal insulation, interfacial solar vapor generation, *etc.*) are highlighted. Finally, challenges in the fabrication of 3D fibrous aerogels, limitations for their use, and trends for future developments are discussed.

Received 28th July 2022
Accepted 18th November 2022

DOI: 10.1039/d2ta05984c

rsc.li/materials-a

1. Introduction

Aerogels are commonly described as high surface area substances that are nanostructured (mostly mesoporous with a few micropores) and consist of a porous solid network.[1,2] Generally, aerogels are gels in which the liquid is supplanted by gas while the pores and networks are well preserved.[2] A special drying technique is used to remove the liquid in gels and avoids apparent volume shrinkage.[3] The resultant aerogels exhibit a mainly air-containing three-dimensional (3D) structure with many unique characteristics, including ultralow bulk density (<0.5 g cm^{-3}), high surface area (>50 m^2 g^{-1}), large porosity (>85%), and thermal-insulating properties, widely applied in many fields like sensors, energy storage, catalysis, and biomedical scaffolds for tissue engineering.[4–7]

The origin of aerogels dates back to 1931 when Kistler reported on the replacement of the liquid in inorganic/organic gels by gas with negligible shrinkage using a supercritical-drying process.[8] This original work did not pay much attention to aerogels until the 1980s when silica aerogels found practical use as Cherenkov detectors in particle accelerators and superinsulators in double-pane windows.[9] Since then, more researchers have tried to assemble crystalline nanoparticles (*e.g.*, oxides, metal sulfides, carbon materials, *etc.*) into macroscopic porous 3D networks by a sol–gel chemistry process, followed by a supercritical-drying or freeze-drying process,[6,10] which endows aerogels with tunable morphologies and enlarge application properties of aerogels.[11,12] Brock's group first reported nanoparticle aerogels by assembling metal chalcogenide nanocrystals into 3D networks *via* the partial removal of coating ligands on the nanoparticles.[13] Afterwards, various metal chalcogenide, metal, and metal oxide nanoparticle-based aerogels have also been prepared by controllable destabilization of the corresponding concentrated nanoparticle suspensions.[14,15] This approach of assembling preformed nanoparticles into aerogels has made it possible to control the compositions and structures of aerogels by tuning the compositions, sizes and morphologies of primary nanobuilding blocks and by engineering the gel structures. However, most of the aerogels were produced by using zero-dimensional (0D) spherical nanoparticles as building blocks and the weak interparticle force throughout the nanoparticle networks made the resultant aerogels too fragile to be integrated into a practical device without destroying their structural integrity.[15]

In this decade, to address the fragility of the aerogels based on 0D nanoparticles, large efforts have been made to develop aerogels using one-dimensional (1D) anisotropic nanostructures with high aspect ratios such as polymer nanofibers as building blocks.[16–18] Nanofibers, as a typical 1D nanostructured material, have been concerned in recent years due to their good

[a]State Key Laboratory of Separation Membranes and Membrane Processes, Tiangong University, Tianjin 300387, P. R. China
[b]School of Textile Science and Engineering, Tiangong University, Tianjin 300387, P. R. China. E-mail: zhxupin@tiangong.edu.cn
[c]Tianjin University of Science & Technology, Tianjin 300222, P. R. China. E-mail: bowen15@tiangong.edu.cn

mechanical flexibility, with remarkable tolerance against mechanical bending and exceptionally low flexural rigidities. Apart from excellent mechanical flexibility and toughness, nanofibers also have the characteristics of a high possibility of surface functionalization, a large surface area, a wide range of material selection and tunable porosity, overcoming the inherent property limitations of conventional active materials.[19,20] Based on the above advantages, 1D polymer nanofibers have been extensively researched as building blocks to develop a new species of 3D fibrous aerogels with a physically entangled and/or chemically crosslinked fibrous network, unlike the interconnected framework constructed by colloidal particles in inorganic aerogels. The "necks" do not exist in the skeletons of 3D fibrous aerogels, which can considerably avoid stress concentration and show mechanical and flexible behavior. 1D polymer nanofiber-assembled 3D fibrous aerogels exhibit many attractive properties including low density, high specific area, large porosity, and tunable pore size on varied length scales.[21,22] Also, the high continuity and open-cell fibrous networks can allow excellent access of fluids, such as low transport limitations for gases and liquids. Therefore, this unique combination of properties makes 1D polymer nanofiber-assembled 3D fibrous aerogel structures highly interesting in the fields of energy and environmental applications.

Given the rapid progress in this field, a complete overview of the structuring of aerogels should be desirably reported. However, nanoparticle-based aerogels composed of semiconductors, metals and metal oxides have already been reviewed somewhere else,[14,15] and also aerogels based on inorganic nanowires have recently been discussed.[10] Therefore, this review aims to focus on fibrous aerogels from 1D polymer nanofibers, because they offer complementary properties like mechanical stability. We emphasize the structural design concepts and controllable synthesis strategies of 3D fibrous aerogels, which mainly include electrospinning, solution blow spinning, freeze-drying, thermally induced self-agglomeration, and carbonization. We systematically highlight the multifunctional applications of 3D fibrous aerogels in various fields, involving energy (*e.g.*, pressure sensors, triboelectric nanogenerators, supercapacitors, electromagnetic interference shielding, *etc.*) and the environment (*e.g.*, air filtration, thermal insulation, oil–water separation, interfacial solar vapor generation, *etc.*) (Fig. 1). Finally, the challenges and future opportunities of 3D fibrous aerogels are described. We hope that this review illustrates different strategies to design, fabricate, and use 3D fibrous aerogels for specific applications and inspires researchers to tackle future challenges in this area.

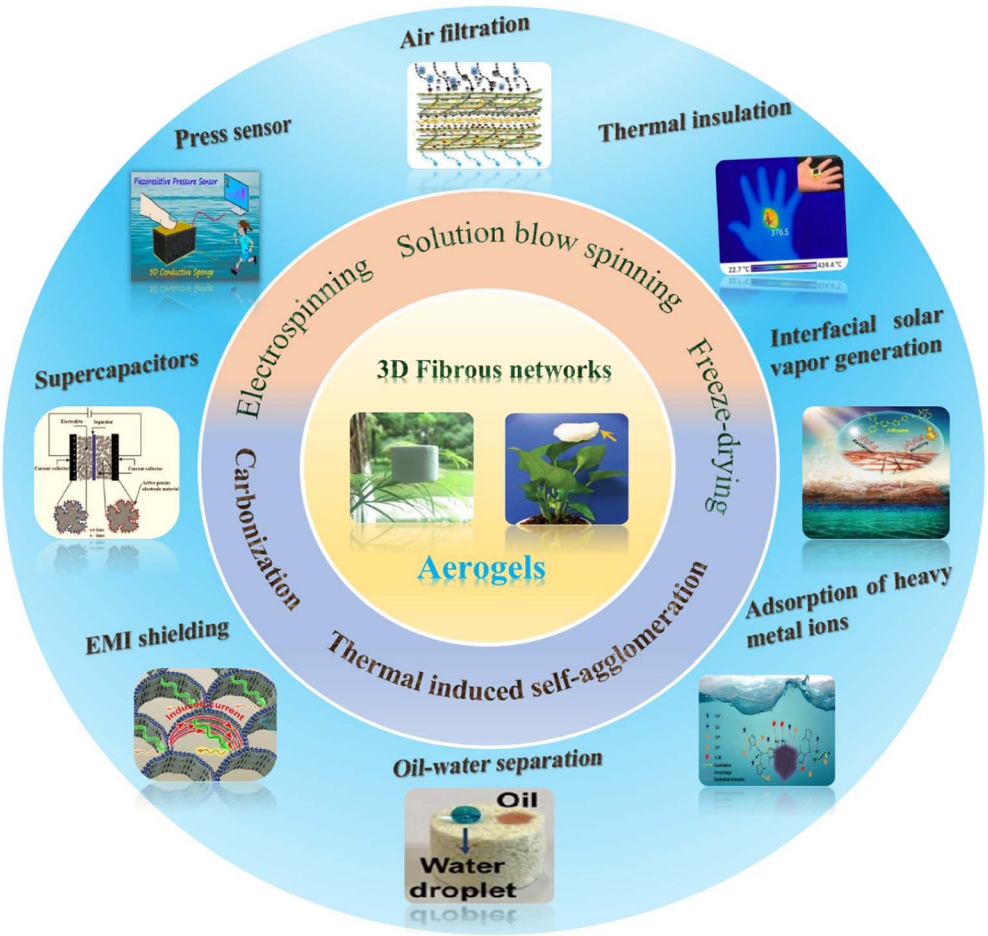

Fig. 1 Schematic illustration of the preparation process and potential use of 3D fibrous aerogels in energy and environmental applications.

2. Strategies to synthesize 3D fibrous aerogels

Until now, various methods have been explored to prepare 3D fibrous aerogels. Generally, 3D fibrous aerogels with different structural characteristics can be prepared by using different approaches to assemble nanofibers in the states of single fibers or aggregation. The mechanical and other functional properties of 3D fibrous aerogels are highly dependent on their microstructures. In this section, we mainly introduce the process and characters of recently reported fabrication strategies, involving electrospinning, solution blow spinning, freeze-drying, thermally induced self-agglomeration, and carbonization techniques.

2.1 Electrospinning

2.1.1 Formation mechanism. Electrospinning technology is a powerful way to fabricate nanofibers with consistent diameters of tens of nanometers to a few micrometers, diverse structures, and tunable compositions. The overall

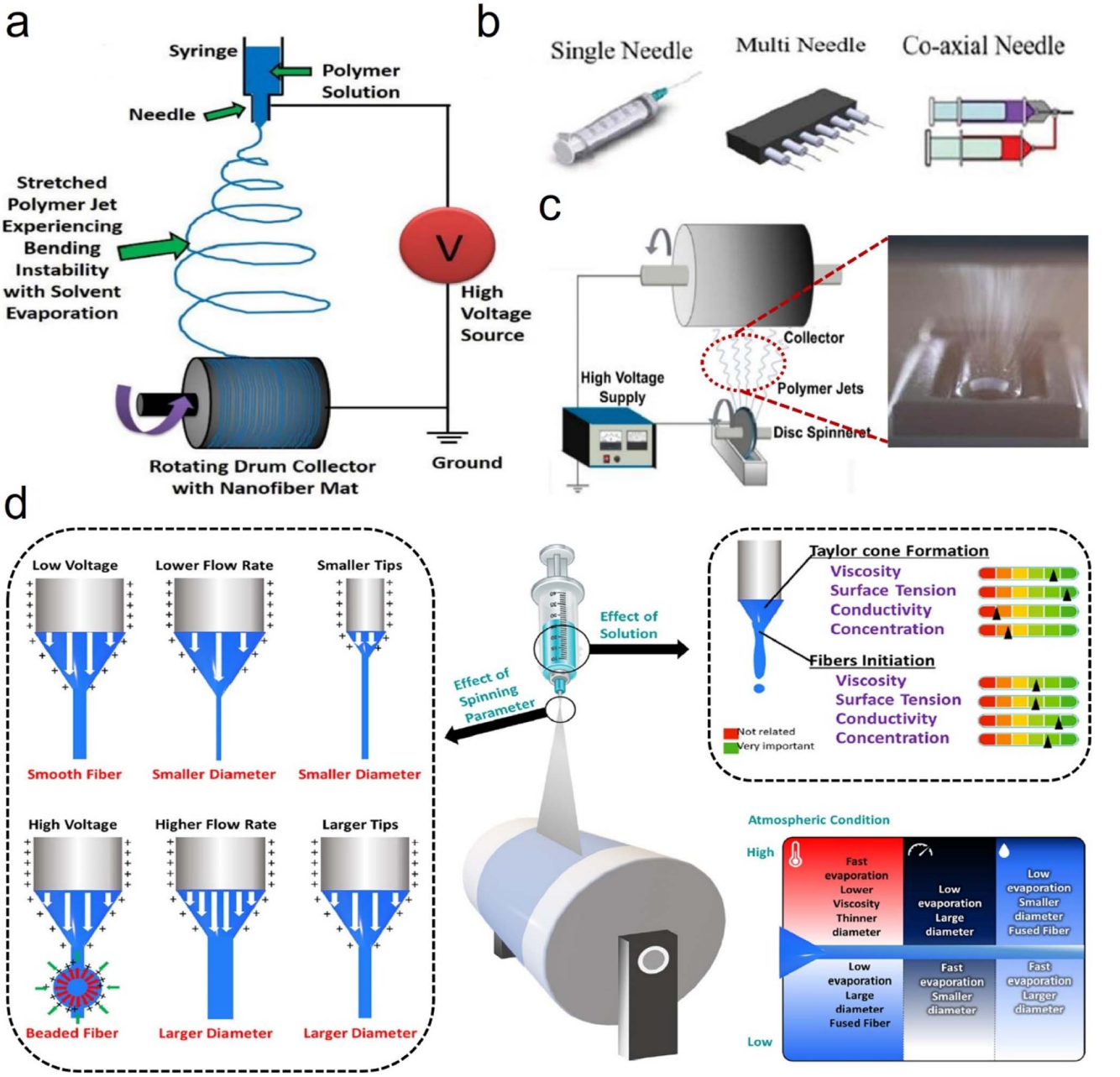

Fig. 2 Electrospinning process design and parameters. (a) Schematic representation of the electrospinning process. Reproduced with permission.[25] Copyright from 2010, American Chemical Society. (b) Different types of syringes. Reproduced with permission.[26] Copyright from 2019, Elsevier. (c) Schematic representation of the needleless electrospinning process. Reproduced with permission.[23] Copyright from 2014, Elsevier. (d) Summary of the effects of various processing parameters on the morphology and diameter of electrospun nanofibers. Reproduced with permission.[27] Copyright 2022, AIP.

electrospinning process includes three aspects: high voltage power supply, spinning solution, and collector (Fig. 2a). When a high voltage field is applied, the droplet of polymer solution at the tip of the needle will become highly electrified, and the charges induced will be evenly distributed over the polymer solution surface.[23–26] The droplet will be subjected to two types of electrostatic forces, including electrostatic repulsion between the charges on the surface and coulombic forces in the external field. Under the effect of these two forces, the droplet will be elongated and finally distorted into a so-called Taylor cone.[25,26] As the voltage further increases, the electrostatic forces will become stronger and eventually overcome the surface tension, and a charged jet of fluid will be ejected. This process leads to an increment of travel time and the distance of the fiber jet to the collector, thus aiding the formation of a long and thin fiber. As depicted in Fig. 2b and c, several different types of syringes (*e.g.*, single, multi, co-axial needle, and needleless) can be used to design the desired structure of electrospun nanofibers. Generally, the intricate interplay between all key electrospinning parameters determines the morphology and diameter of electrospun nanofibers. For example, with a higher flow rate, the critical voltage, and the working distance between the tip of the spinneret and the collector, the need to be increased is to ensure the full extension and solidification of the jet. Fig. 2d summarizes the effects of these key electrospinning parameters on the morphology and diameter of electrospun nanofibers. These parameters are divided into three main categories: (1) solution parameters such as concentration, molecular weight, viscosity, surface tension, and conductivity; (2) processing conditions such as voltage, nature of collectors, flow rate, and syringe-to-collector distance; (3) ambient parameters such as humidity and temperature.[27–29] Therefore, critically optimizing these parameters is pretty crucial in mass-producing high-quality electrospun nanofibers for meeting various application requirements.

Due to the simplicity of the assembly process and the facile availability of electrospun nanofibers, some researchers have tried to develop and modify electrospinning processes to directly generate 3D fibrous aerogels. The main goal of this design is to construct mechanically robust homogeneous structures capable of forming a 3D cellular architecture, while preserving the inherent functionality of nanofibers. Compared with the 2D compact structure of electrospun mats/membranes, 3D fibrous aerogels with light weight, large porosity, high mechanical strength, and superior sorption properties will be mostly desirable in various fields, such as thermal insulation, adsorption, air filtration, and so on.[30,31]

2.1.2 Morphology and pore structure. Lately, fibrous aerogels formed *via* electrospinning with a 3D structure have attracted much attention because of their highly curved pore structure, high specific surface area, high porosity, and low density. The electrospinning process parameters and environmental conditions can directly determine the fiber morphology and diameter of 3D fibrous aerogels.[28–30] For example, when electrospinning in low relative humidity (RH), the water in the atmosphere has little influence on the solidification rate of jets, and the forces caused by the jet instability are larger than the viscoelastic stresses, thus resulting in the formation of a dense morphology and small fiber diameter for 3D fibrous aerogels. In contrast, when electrospinning under high-RH conditions, the water in the atmosphere would penetrate into the spinning jets and induce the thermodynamic instability of the solution; meanwhile, the evaporation of solvent increases the polymer concentration in the spinning jets. Thus, the viscoelastic forces would be strengthened, and a fluffy structure could be obtained. Typically, Zhao *et al.*[30] reported a humidity-assisted electrospinning method to prepare 3D polysulfone/polyurethane (PSU/PU) fibrous aerogels (Fig. 3a). The fluffy hierarchical structure endowed the 3D fibrous aerogels with ultralight properties (Fig. 3b), which could freely stand on the top of the flower. Under a high humidity, 3D PSU fibrous aerogels had a highly fluffy structure, which was mainly ascribed to the humidity-induced phase separation of the spinning jets. The fluffy structure remained steady, while the PU concentration increased from 0 to 40 wt% (Fig. 3c). However, the material changed from a fluffy stacked to a dense fibrous structure when the concentration of PU was 60 wt%. As the solution viscosity increased with the increase of the mass content of PU, the average fiber diameter of the 3D PSU/PU fibrous aerogels decreased first and then increased. As shown in Fig. 3d, the volume densities and porosities of the material with various contents of PU (0, 20, 40, and 60 wt%) were 2.63, 3.21, 4.93, and 610.70 mg cm^{-3} and 99.71, 99.62, 99.55, and 50.18%, respectively. Similarly, Wu *et al.*[31] prepared an ultralight and superelastic photo-thermal convertible 3D fibrous aerogel by assembling fiber containing zirconium carbide (ZrC) nanoparticles into 3D PSU aerogels through combining humidity-induced electrospinning and thermal crosslinking technology (Fig. 3e). The obtained 3D PSU/ZrC fibrous aerogels could stand freely on the tip of a leaf, exhibiting ultralight properties (density = 2.8 mg cm^{-3}) due to the high porosity of 99.8% (Fig. 3f). Abundant bridging fibers are randomly interspersed and entangled through fiber nets to connect every lamellar fiber net (Fig. 3g). Besides, the 3D PSU/ZrC fibrous aerogels with a ZrC nanoparticle content of 12 wt% could be rolled-up, knotted, and even winded without breakage, indicating excellent toughness and softness (Fig. 3h).

2.1.3 Mechanical properties. The mechanical properties of aerogels are generally considered as a critical factor for their practical applications. For 3D fibrous aerogels, nanofibers can serve as building blocks to form a physically entangled and/or chemically crosslinked 3D fibrous network, which can avoid stress concentration and show mechanical and flexible behavior.[18] Moreover, these excellent mechanical properties can endow the 3D electrospun fibrous aerogels with promising structural integrity, which is conducive to their maximum functionality. To better characterize the mechanical properties of 3D fibrous aerogels, more researchers have tried to demonstrate them by compression resilience. As shown in Fig. 4a, the compressive σ–ε curves for a FR PSU/PU-20 fibrous aerogel were obtained under various strains of 20%, 40%, 60%, and 80%. The results demonstrated that the FR PSU/PU-20 fibrous aerogel had only a very small plastic deformation under 80% compression deformation, indicating that the aerogel had

excellent compressive resilience. Then, the FR PSU/PU-20 fibrous aerogel was subjected to 100 cyclic compression tests at 25 °C to study its fatigue resistance ability. Fig. 4b shows that the FR PSU/PU-20 fibrous aerogel only produced 3.6% negligible plastic deformation after 100 compression cycle tests. The elasticity test of the FR PSU/PU-20 fibrous aerogel was further emphasized. Surprisingly, the FR PSU/PU-20 fibrous aerogel (310 mg) could return to the original shape quickly after being compressed by a weight of 500 g (Fig. 4c), which proved its excellent compression resilience. The FR PSU/PU-20 fibrous aerogel still maintained the compression recovery performance with more than 90% of the initial value, showing little change in the energy loss coefficient (Fig. 4d). Similarly, Wu *et al.*[31] reported electrospun 3D fibrous aerogels with superelasticity, which could withstand over 10 000 times their weight (Fig. 4e). Furthermore, an *in situ* compression process was observed to reveal the resilience mechanism of 3D fibrous aerogels. The large distance between the lamellar fiber nets gradually decreased and the lamellar fiber nets became densified as the strain increased. After releasing the load, the compact fiber nets could recover to the initial positions without any break (Fig. 4f). The bridging fibers gradually deformed along the loading direction, and after removing the load, the bridging fibers recovered their original shape without breakage (Fig. 4g). These

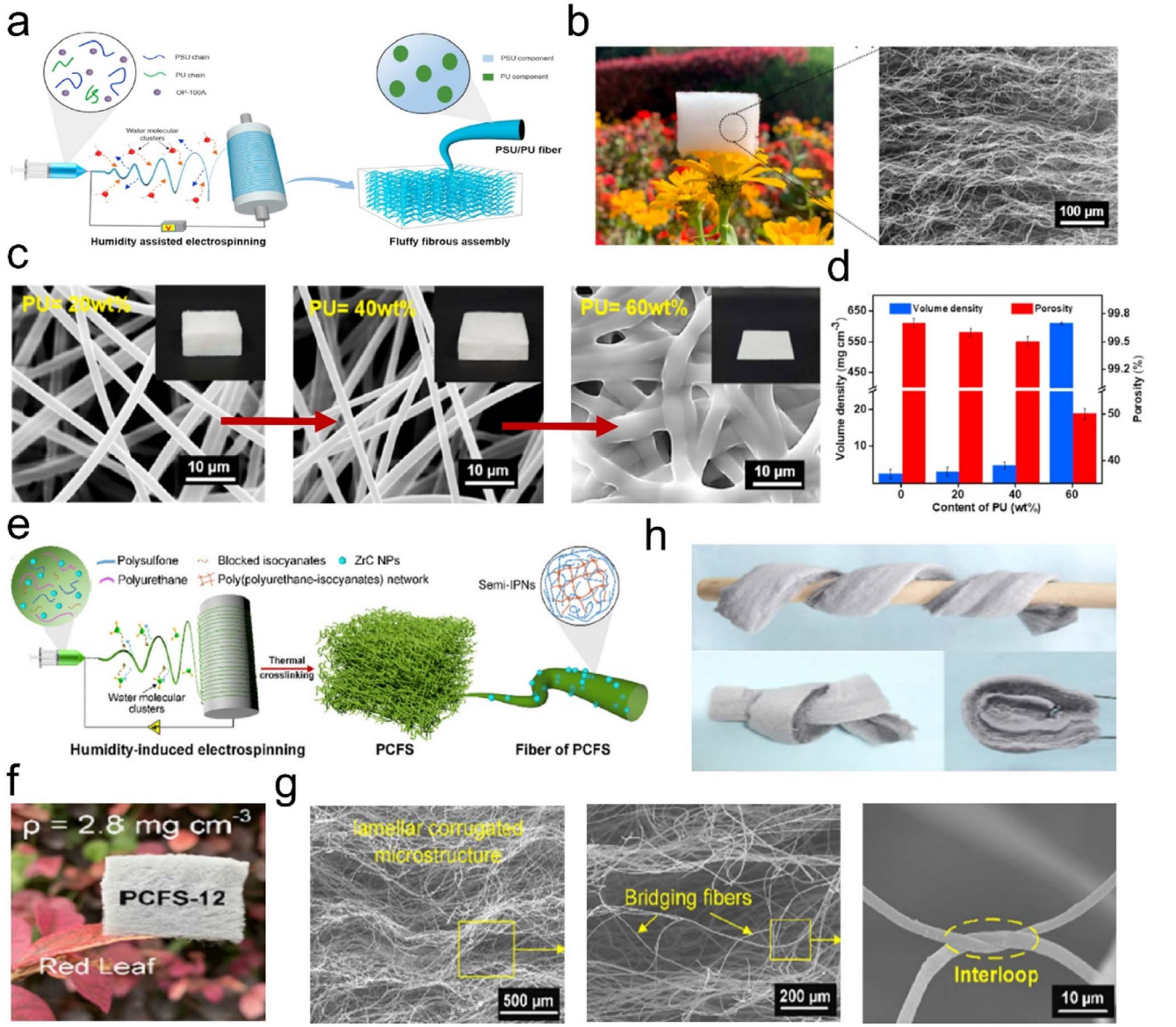

Fig. 3 Microstructure of 3D fibrous aerogels prepared by the electrospinning process. (a) Schematic illustration for the fabrication of 3D PSU/PU fibrous aerogels. (b) Photograph and scanning electron microscopy (SEM) image showing the lamellar corrugated microstructure of 3D PSU/PU fibrous aerogels. (c) SEM images, and (d) volume and porosity density of the 3D PSU/PU fibrous aerogels with different contents of PU. Reproduced with permission.[30] Copyright 2021, Elsevier. (d) Preparation of the 3D PSU/ZrC fibrous aerogels. (e) Presentation of the synthetic steps for the 3D PSU/ZrC fibrous aerogels. (f) Images showing the softness and toughness of the 3D PSU/ZrC fibrous aerogels. (g) Photographs showing the ultralight properties of the 3D PSU/ZrC fibrous aerogels. (h) Microscopic architecture of the 3D PSU/ZrC-12 fibrous aerogels at various magnifications. Reproduced with permission.[31] Copyright 2019, Elsevier.

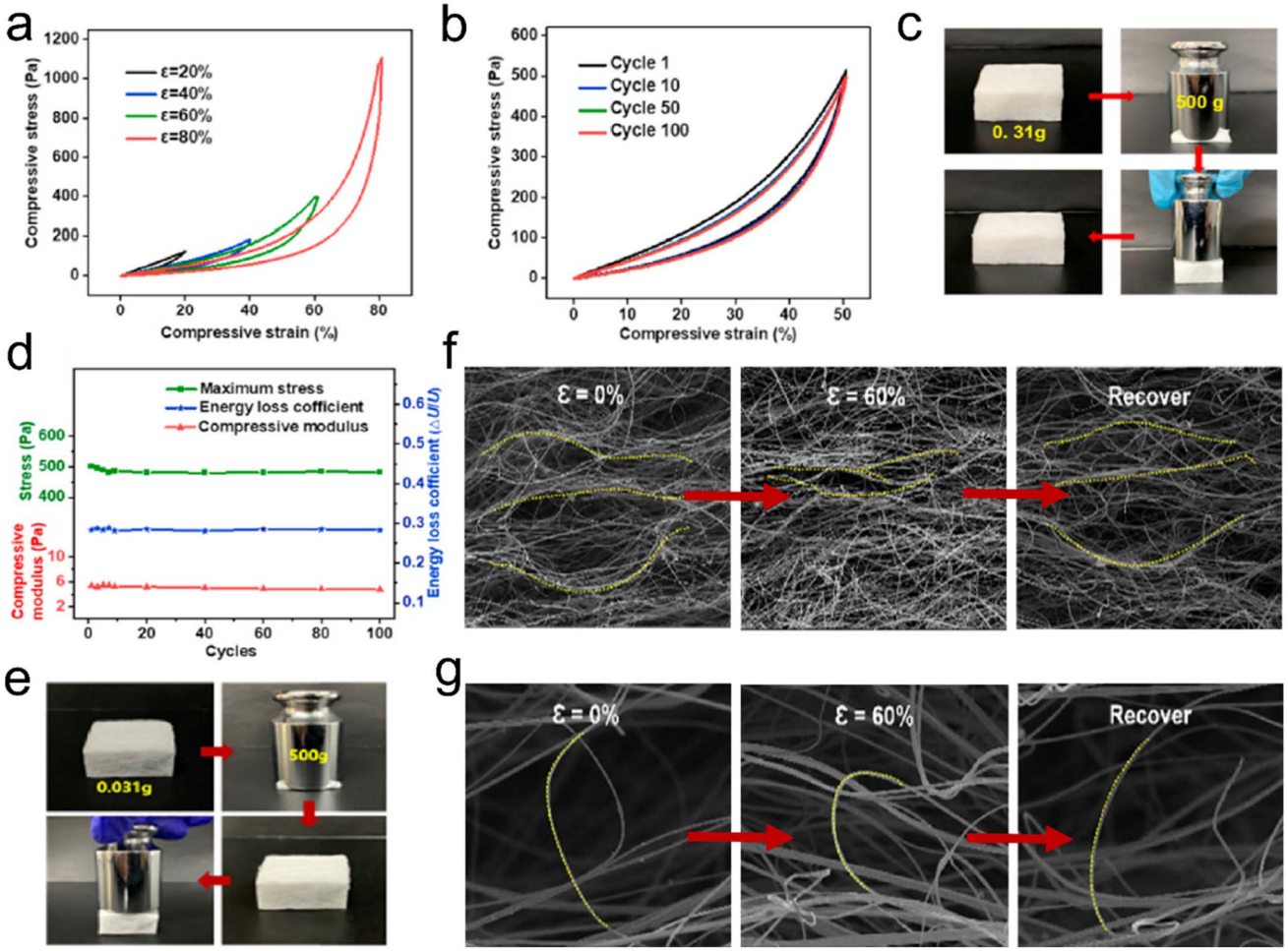

Fig. 4 Reversible compressibility of 3D fibrous aerogels prepared by the electrospinning process. (a) Compressive $\sigma-\varepsilon$ curves for the FR PSU/PU-20 fibrous aerogel with various strains of 20%, 40%, 60%, and 80%. (b) A 100-cycle fatigue compression test with $\varepsilon = 50\%$ of the FR PSU/PU-20 fibrous aerogel. (c) Images showing that the FR PSU/PU-20 fibrous aerogel could quickly recover from large compressive distortion. (d) Maximum stress, compressive modulus, and energy loss coefficient *versus* compressive cycles. Reproduced with permission.[30] Copyright 2021, Elsevier. (e) Images showing that the 3D PSU/ZrC-12 fibrous aerogel could quickly recover from large compressive distortion. *In situ* observation of the microstructure evolution of (f) lamellar fiber nets and (g) bridging fibers. Reproduced with permission.[31] Copyright 2019, Elsevier.

results have demonstrated that introducing elastomer materials or adding some crosslinking agent with heat treatment can effectively improve the mechanical properties of 3D electrospun fibrous aerogels.

2.2 Solution blow spinning

2.2.1 Formation mechanism. Solution blow spinning (SBS) is an attractive nanofiber technology that combines electrospinning and traditional melt blowing technologies. The working mechanisms are shown in Fig. 5a. As high-pressure gas stream leaves the outer nozzle, the pressure drops to atmos, at which time the jet flow energy increases and the gas velocity increases, which in turn promotes a drop in the pressure at the center of the jet, forming the driving force to accelerate polymer solution extrusion.[32–34] The high-velocity gas flow also causes shearing force at the gas/solution interface, thereby deforming the polymer solution from a droplet to a conical shape. When this shearing force overcomes the surface tension of polymer solution, a solution jet is generated.[35] Compared with the electrospinning technique, the SBS process has some apparent advantages: (I) a wide range of raw materials and strong material suitability; for instance, abundant polymer materials are soluble in non-toxic and volatile solutions, which can be applied as a raw component. (II) Conductivity and high-voltage electrostatic field support are not required; therefore, the safety is relatively higher, and the device requirement is lower. (III) Using a high-velocity gas flow at room temperature as the driving force can effectively prevent the thermal degradation of the polymer.

Besides, researchers have found some key elements which can affect the fiber formation when using the SBS process, such as solution influence (viscosity, polymer solution concentration, surface tension, and solvent evaporation), process influence (gas pressure, receiving distance, and liquid intake), system influence (nozzle size and collector category), and ambient influence (atmospheric pressure, temperature, humidity, and

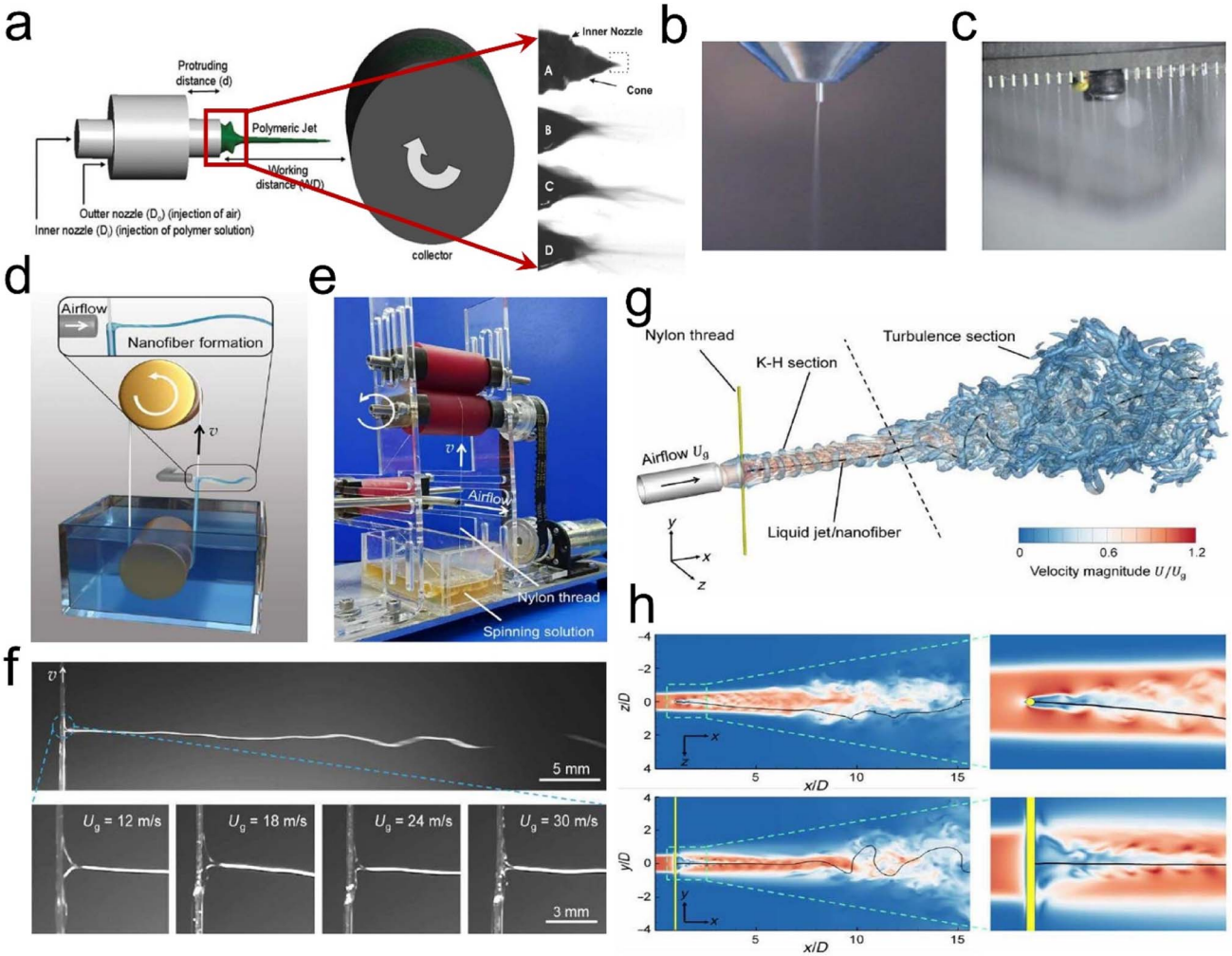

Fig. 5 SBS process design strategy. (a) Drum collection schematic. Reproduced with permission.[35] Copyright 2020, Royal Society of Chemistry. (b) SBS apparatus with a single-needle spinning die. Reproduced with permission.[40] Copyright 2018, Wiley-VCH. (c) SBS apparatus with a multi-needle spinning die. Reproduced with permission.[41] Copyright 2017, Royal Society of Chemistry. (d) Illustration of the KV-SBS process. (e) Photograph of a running KV-SBS equipment. (f) The ejected solution captured by using a high-speed camera in the KV-SBS process. (g and h) CFD simulation results of the airflow velocity magnitude coupled with the swing patterns of the fiber in 3D space. Reproduced with permission.[42] Copyright 2022, American Association for the Advancement of Science.

atmospheric pressure).[36–39] Wu *et al.*[40] utilized the SBS process with a single needle (Fig. 5b) to produce various ceramic nanofibers (*e.g.*, TiO_2, ZrO_2, and $BaTiO_3$). Our groups[41] have also developed a multi-needle SBS process (Fig. 5c) to produce some different types of micro/nanofibers, including cellulose, polyacrylonitrile (PAN), polylactic acid, (PLA), and sulfonated polyether ether ketone (SPEEK), which all exhibited excellent fiber morphology and porous structure characteristics. To further prepare fine fibers with a high throughput, Wu *et al.*[42] demonstrated a needleless Kármán vortex (KV)-SBS system to realize high-throughput production of nanofibers. As shown in Fig. 5d–f, the spinning system was assembled by using a roller, a vessel filled with spinning solution, a loop-locked nylon thread, and a gas pipeline set vertically to the thread to provide high-speed air blowing. Driven by the high-speed airflow, the solution was shaped into a Taylor cone and ejected at a high speed, forming nanofibers by fast stretching and swinging. The formation mechanism of nanofibers was studied by fluidic theory analysis, high-fidelity computational fluid dynamics (CFD) simulations, and a bead-spring model for simulating the fiber behavior (Fig. 5g and h). The tailor-made flow configuration combines an airflow and a KV street. The high-speed airflow passing across the nylon thread generated a strong shear stress and KV on the leeward side of the thread, which was beneficial for high-quality nanofiber production.

Based on the relatively proficient SBS process, more research attention has been paid to utilizing the SBS process to prepare 3D fibrous aerogels like ceramic nanofibers. Specifically, within the SBS process, the solidified fibers can be directly collected by using an air-permeable cage-like collector, thereby forming the desired highly porous aerogels. Moreover, the shaped 3D fibrous aerogels by the SBS process show excellent flexibility. Therefore, the SBS process is regarded as a flexible and robust strategy to prepare 3D ceramic fibrous aerogels with a randomly

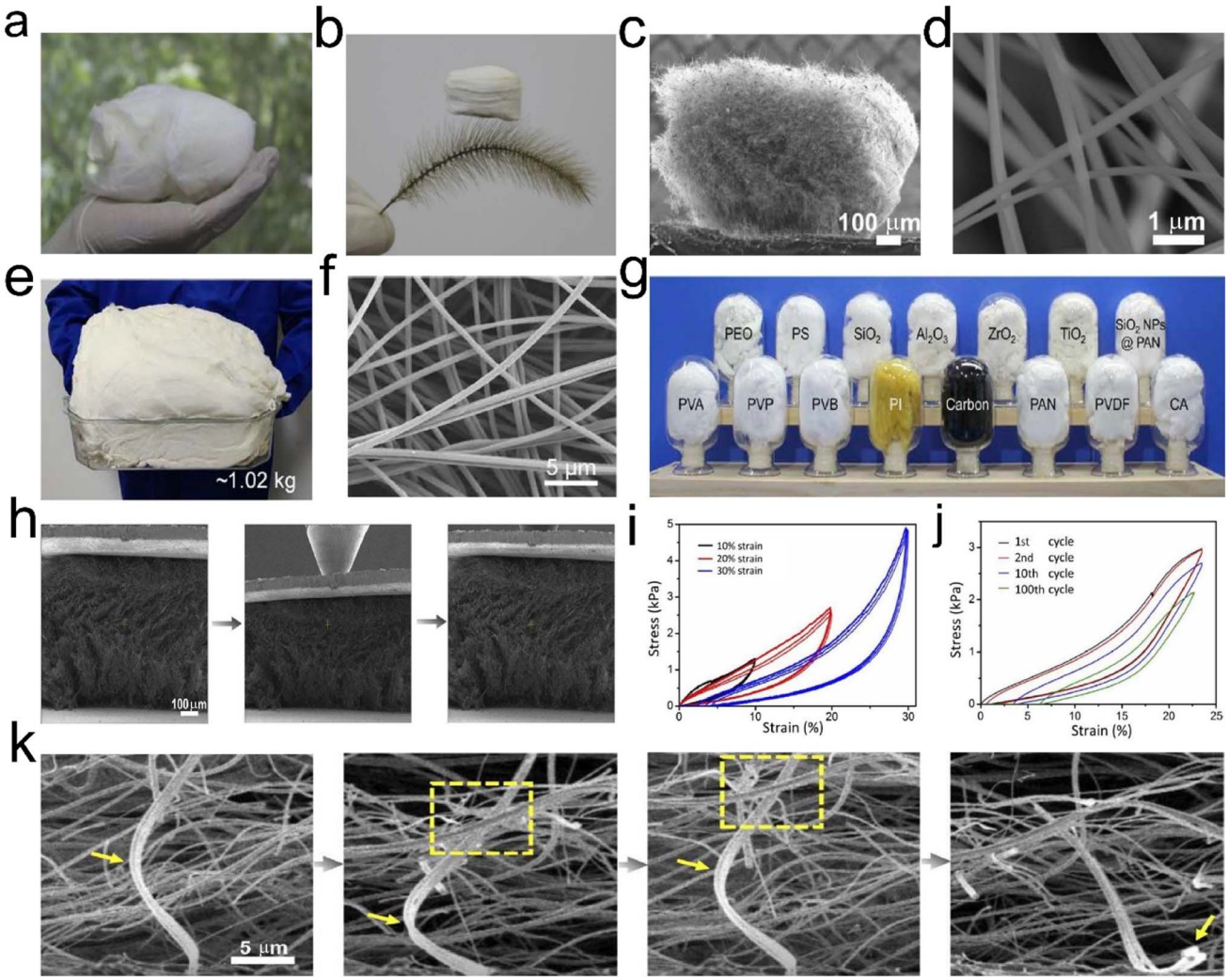

Fig. 6 Microstructure of 3D fibrous aerogels prepared by the SBS process. (a) An optical photograph of TiO_2 fibrous aerogels. (b) Ultralight TiO_2 fibrous aerogel standing on a Setaria viridis. (c and d) SEM image of TiO_2 fibrous aerogels with different magnifications. Reproduced with permission.[43] Copyright 2019, Elsevier. (d) Photograph of kilogram-scale PS nanofibers fabricated *via* the KV-SBS process. (e and f) An optical photograph and SEM image of the PS fibrous aerogels. (g) Photographs of various aerogels prepared by the KV-SBS process. Reproduced with permission.[42] Copyright 2022, American Association for the Advancement of Science. (h) *In situ* SEM images of the compressive process of TiO_2 fibrous aerogels. (i) Cyclic compressive stress–strain curves of TiO_2 fibrous aerogels under 10% to 30% strain. (j) Cyclic compressive stress–strain curves of TiO_2 fibrous aerogels under 23% strain for 100 cycles. (k) Zoomed-in SEM images during the compression process. Reproduced with permission.[43] Copyright 2019, Elsevier.

distributed microstructure by changing the initial ceramic precursors.

2.2.2 Morphology and pore structure. Some developed studies have shown that ceramic nanocrystalline nanofibers are highly flexible because of their high aspect ratios and nanometersized grains, which can be an ideal candidate for building blocks for 3D elastic assemblies.[42,43] For example, Huang *et al.*[43] utilized the SBS process to produce TiO_2 fibrous aerogels. Macro-sized tetrabutyl titanate ($Ti(OBu)_4$)/polyvinyl pyrrolidone (PVP) fibrous aerogels (Fig. 6a) were first prepared by SBS technology. After calcination for 200 min at 450 °C, the PVP was removed, and $Ti(OBu)_4$ was then hydrolyzed into pure TiO_2 fibrous aerogels (Fig. 6b) with ultralow density, typically ranging from 8 to 40 mg cm^{-3}, depending on the fiber diameter and aerogel porosity. This density range was comparable to that of ceramic aerogels and nanolattices. Fig. 6c shows a SEM image of a piece of TiO_2 aerogel, where uniform nanofibers with a diameter of ~180 nm interweave with each other, leading to a cellular architecture with an open-cell geometry and porosity above 99.7% (Fig. 6d). Similarly, by using different ceramic precursors, some other fibrous aerogels (*e.g.*, ZrO_2, $BaTiO_3$, *etc.*) have been fabricated. Besides, taking advantage of the high-throughput production of nanofibers with a KV-SBS system, Wu *et al.*[42] prepared kilogram-scale PS nanofibers with a porous and interlaced 3D structure (Fig. 6e and f) in a highly efficient manner. To verify the versatility of the KV-SBS process, multifarious nanofibers including PAN, polyvinyl alcohol (PVA), polyvinyl pyrrolidone (PVP), polyvinyl butyral (PVB), polyimide

(PI), polyvinylidene fluoride (PVDF), cellulose acetate (CA), polyethylene oxide (PEO), carbon, ceramics, and their composites could be all successfully prepared and collected to form 3D fibrous aerogels (Fig. 6g).

2.2.3 Mechanical properties. The microstructures described above have indicated that the ceramic fibrous aerogel is an open-cell bending-dominated structure, and therefore, it is capable of retaining its stiffness and resilience even at high external compression. Specifically, the 3D ceramic fibrous aerogels prepared by the SBS process can be repeatedly compressed to large strains, with marked recoverability after each compression. To reveal the underlying mechanism, Wang *et al.*[43] performed *in situ* monotonic and cyclic uniaxial compression tests using an SEM on fibrous aerogels at room temperature. During testing, the specimen was glued *via* silver paste between the Si loading stage and a light metal sheet and was subjected to compression by using a conical nanoindenter with a 100 mm diameter flat tip (Fig. 6h). Fig. 6i shows a series of cyclic compressive stress–strain curves of 3D TiO_2 fibrous aerogels with a density of ~35 mg cm^{-3} at room temperature under different strains of 10%, 20%, and 30%. From the linear elastic regime of the stress–strain curve during the first cycle of compression, the compressive modulus of the TiO_2 fibrous aerogels was approximately 12.25 kPa. The compressive modulus of TiO_2 fibrous aerogels follows the scaling law $E \sim (\rho/\rho_s)^2$ with respect to the relative density, similar to fibrous aerogels composed of PAN and SiO_2 nanofibers. This indicates that 3D ceramic fibrous aerogels have an open-cell bending-dominated structure. After 100 cycles of compression at 23% strain and room temperature, the TiO_2 fibrous aerogels had a residual strain of only 7% and a maximum stress of nearly 73% of its original value (Fig. 6j). Furthermore, SEM images during the compression process in Fig. 6k illustrated the energy absorption mechanisms including plastic deformation and fracture of individual nanofibers as well as friction between adjacent nanofibers for the ceramic fibrous aerogels under study. Therefore, 3D ceramic fibrous aerogels are capable of retaining their stiffness and resilience, indicating potential applications in various fields.

2.3 Freeze-drying

2.3.1 Formation mechanism. Freeze-drying (also known as lyophilization) is a dehydration process, in which the frozen solvent in a substance sublimes directly from the solid phase to the gas phase under reduced surrounding pressure.[44,45] In 2006, Deville *et al.*[46] first proposed that the physics of ice formation could be used to develop multiform porous and layered-hybrid materials. Since then, the freeze-drying technique has been widely used to prepare 3D fibrous aerogels of nanocellulose, ceramics, metals, carbon nanotubes (CNTs), graphene, graphene oxide (GO), and biopolymers.[47–55] Subsequently, Ding's group[56] first reported to use shortened electrospun nanofibers as the building blocks to prepare 3D fibrous aerogels by the freeze-drying technique. The formation mechanism of interconnected and hierarchically structured pores of 3D fibrous aerogels is shown in Fig. 7a. During the freezing stage, the homogeneously dispersed nanofibers are enriched among the solvent crystals (Fig. 7b). With the growth of ice crystals, the nanofibers are confined among the crystals and become intertwined due to the expansion of ice crystals. Consequently, the nanofibers are locked into a 3D solid network. After the drying stage, the solidified solvent sublimes, and the constructed 3D fibrous aerogels can be well obtained. The structure of 3D fibrous aerogels is a replica of that solidified solvent. The large pores are determined by the solidified solvent crystals, and the small pores are formed by the shortened electrospun nanofibers.[45]

2.3.2 Morphology and pore structure. First, the dispersion solvent for preparing the suspension has an essential impact on the formation of morphologically 3D fibrous aerogels, and the melting point is a critical factor in choosing the solvent. Typically, water (with a melting point of 0 °C) is generally selected as a low-cost freeze-drying solvent, while other organic solvents such as dioxane (12 °C), dimethyl sulfoxide (DMSO) (19 °C), *tert*-butanol (~25 °C), and camphene (~50 °C) can also be used. However, water is a familiar solvent for the freeze-drying process, which can form relatively large and non-uniform ice crystals at a slow freezing rate of 0.5–3 °C min^{-1}, resulting in cracks on both outer and inner surfaces, and poor integrity of the 3D structure. As a result, adding a small amount of ethanol to the suspension can effectively improve the size and uniformity of ice crystals, while ethanol alone is not a suitable solvent for freeze-drying (due to the low melting point).[57] Significantly, those organic solvents are suitable for freeze-drying and can also be used to tailor the size and uniformity of ice crystals. For example, *tert*-butanol can be mixed with water to control the volume and shape of the frozen samples (Fig. 7b).[56] The shapes of 3D fibrous aerogels (Fig. 7c) can be controlled, and the fabrication is possible to be scaled up by simply using a large shaping mold. Within the freeze-drying process, the dispersed nanofibers were enriched and entrapped among the solvent crystals. The structure of the 3D architecture was a replica of that of the solidified solvent, and the size distribution of large pores was determined by the size of solvent crystals. The assembly of shortened electrospun nanofibers could form small pores. The cellular structures showed an open-cell architecture with major cellular pores (10–30 μm) and these cells were interconnected with each other by triangular junctions, which consisted of numerous minor cellular pores with sizes of 1–2 μm (Fig. 7d–g). Second, the large pores can be adjusted by controlling the freezing rate. Fong *et al.*[57] investigated the effects of the freezing rate on pore structures. During the freezing process, a fast cooling rate would lead to a rapid homogeneous nucleation process that could generate many nuclei, and small crystals were then grown in the sample. Correspondingly, the 3D fibrous aerogels formed by fast freezing had small pores (<2 μm) and narrow pore size distribution, while the 3D fibrous aerogels formed by slow freezing had hierarchical pores combining large pores (~100 μm) and small pores (<2 μm). Besides, Adlhart *et al.*[58] investigated the effect of freezing conditions on these structures and found similar results. By increasing the freezing-front velocity from 2

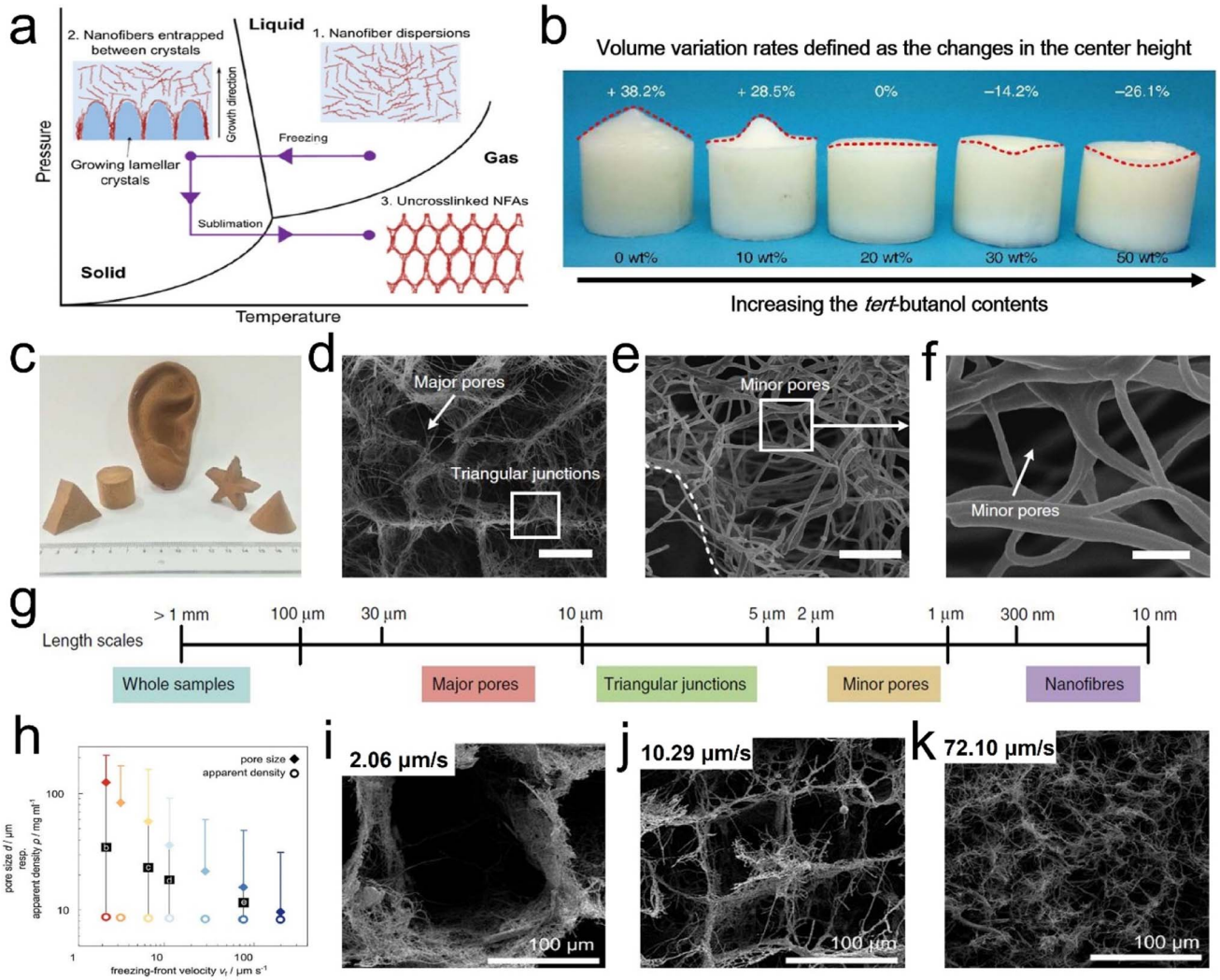

Fig. 7 Formation mechanism and microstructure of a hierarchical cellular structure by the freeze-drying process. (a) Mechanism for the formation of the hierarchical cellular structure. (b) Photograph showing the frozen nanofiber dispersions with different concentrations in *tert*-butanol. The top values indicate the volume variations. (c) An optical photograph of 3D fibrous aerogels with diverse shapes. (d–f) SEM images of 3D fibrous aerogels at various magnifications. (g) Schematic representation of the dimensions of relevant structures. Reproduced with permission.[56] Copyright 2022, Springer Nature. (h) Effect of freezing conditions on the aerogel microstructure. (i–k) SEM images showing the cross sections of the respective aerogels at a center height of 7.5 mm obtained with different v_f. Reproduced with permission.[58] Copyright 2016, Wiley-VCH.

to 200 μm s^{-1}, the pore size decreased from 123 to 9.5 μm (Fig. 7h–k).

2.3.3 Mechanical properties. The solid network in a 3D structure composed of shortened nanofibers alone is generally fragile after freeze-drying due to a lack of robust bonding or interaction (*e.g.*, only topological entanglements and weak van de Waals interactions are present) among the shortened nanofibers. Therefore, adding some compatible crosslinking or binding agents such as poly(amic acid) (PAA), glutaraldehyde, konjac glucomannan (KGM), alginate/Al^{3+}, GO, citric acid, or PVA into the dispersion solvent during the preparation of nanofiber suspension is the most commonly adopted method to improve the mechanical properties of 3D fibrous aerogels.[57,59,60] For instance, PVA was added into cellulose nanofiber suspension before freeze-drying as a binding agent to enhance the mechanical stability and elasticity of cellulose aerogels.[57] During the stabilization at a temperature of 230 °C, PVA macromolecules would undergo chemical changes to form dehydrated structures, which could conglutinate nanofibers together in the 3D fibrous aerogels (Fig. 8a and b). The resultant 3D cellulose fibrous aerogel pieces could fully recover to their original shapes after release of the compression force and bending force, respectively (Fig. 8c).

Besides, by regulating the growth direction of ice crystals in the freeze stage, unique honeycomb-like structures can be obtained, which is beneficial to strengthen the mechanical properties of 3D fibrous aerogels. For example, Fu *et al.*[59] developed super-elastic SiO_2/polyvinyl alcohol/citric acid (SiO_2/PVA/CCA) nanofibrous aerogels with an ordered honeycomb-like structure (Fig. 8d–g). The prepared nanofibrous aerogels showed

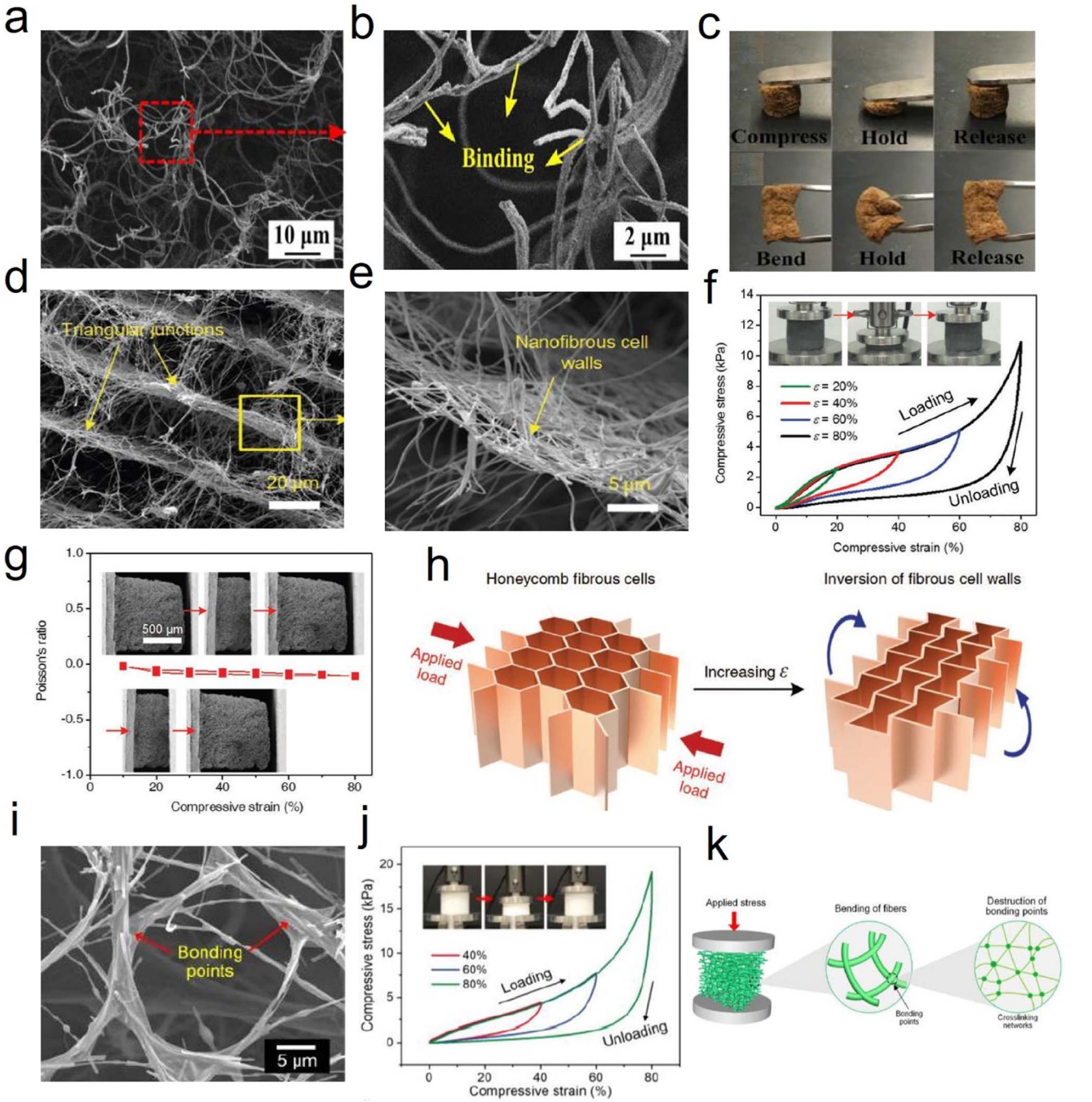

Fig. 8 Reversible compressibility of 3D fibrous aerogels prepared by the freeze-drying process. (a and b) SEM images showing the binding of cellulose nanofibers with PVA. (c) A photograph demonstrating the elasticity of a 3D cellulose nanofiber aerogel under compression and bending forces/conditions. Reproduced with permission.[57] Copyright 2017, Elsevier. (d–g) SEM images of SiO_2/PVA/CCA fibrous aerogels at various magnifications. (h) Compressive stress, and (i) 1000 loading–unloading compression cycle measurement of the SiO_2/PVA/CCA fibrous aerogels. Reproduced with permission.[59] Copyright 2019, Wiley-VCH. (i) SEM image of the SNF aerogel. (j) Compressive σ–ε curves of aerogels with increasing ε. (k) Schematic showing the compressive process of the aerogels at three levels of the structure: silica nanofiber aerogel, individual nanofiber, and crosslinking network. Reproduced with permission.[62] Copyright 2020, Wiley-VCH.

excellent mechanical properties, and the structure could endure large compressive deformations without cracks, similar to honeycomb-structured materials. Three obvious regions including an elastic linear region (ε < 10%), a plateau region (10% < ε < 60%), and a densification region (ε > 60%) were observed (Fig. 8h). Besides, the SiO_2/PVA/CCA nanofibrous aerogels presented nearly no plastic deformation after 1000 compressive cycles at 60% strain (Fig. 8i). Similarly, Qin *et al.*[61] demonstrated a strategy for controlling the growth of ice crystals in both directions that could control the assembly of

cellulose nanofibers into sub-micrometer fibers by extremely low-temperature freezing (−196 °C), which could further assemble into an elastic aerogel with interconnected submicron fibers by freezer freezing (−20 °C) and freeze-drying. The prepared cellulose fibrous aerogels had isotropic superelastic behavior that could recover from over 80% compressive strain along both longitudinal and cross-sectional directions, even in an extremely cold liquid nitrogen environment. Wang *et al.*[62] developed an *in situ* synthesis strategy for creating silica nanofiber aerogels with a superelastic biomimetic framework through the combination of flexible SiO_2 nanofibers and rubber-like Si–O–Si bonding networks (Fig. 8i). This approach allows the *in situ* construction of an elastic bonding structure in the biomimetic fibrous framework during the freeze-shaping process. The stress–strain (σ–ε) curves of the prepared aerogels (Fig. 8j) revealed excellent resilience when released from compression. Furthermore, three characteristic regions could be identified in the loading–unloading curves: a nearly linear elastic region for $\varepsilon < 10\%$, a relatively flat stress plateau for $10\% < \varepsilon < 50\%$, and a subsequent densification region for $\varepsilon > 50\%$ with a rapid increase in σ. The maximum σ was 19.2 kPa at a strain of 80%, demonstrating that the aerogel could withstand more than 16 000 times its weight without collapsing, which was comparable to that of polymeric aerogels with a similar density. Fig. 8k demonstrates how the compressive process could be classified into three levels of hierarchy on different scales: silica nanofiber aerogel, individual nanofiber, and crosslinking network. At the top level, the silica nanofiber aerogel was assembled into a highly ordered biomimetic framework to enhance the elastic modulus and stress. With the increase in compressive strain, the bending of individual nanofibers occurred at the building block level. Finally, the destruction of bonding points consisting of the crosslinking networks is a decisive factor in determining the mechanical properties of the aerogel, which also represents damage at the molecular level. The strength and flexibility of the crosslinking networks would have an immediate effect on the maximum stress and elastic recovery of the silica nanofiber aerogels. Besides, Yang *et al.*[63] reported a combined method of vacuum-assisted filtration (VAF) and freeze-drying processes to prepare 3D MXene/aramid nanofiber (ANF) hybrid aerogels with a hierarchical and "mortar-brick" porous structure. The 3D hierarchical porous network could afford intrinsic power and particular interspacing along with the greatest effect to release the external forces and deformations depending on the merit of a controllable process, which convincingly demonstrated that all hybrid aerogels showed credible compressive resilience and high strength to meet the requirement of a piezoresistance sensor well.[64]

2.4 Thermally induced self-agglomeration

2.4.1 Formation mechanism. The thermally induced self-agglomeration (TISA) method was firstly proposed by Fong' group,[65] which is used to assemble shortened polycaprolactone (PCL) nanofiber membranes into 3D fibrous aerogels. Specifically, by immersing a mixture of uniformly dispersed short nanofibers and tiny pieces of PCL into a water bath with a temperature close to the PCL melting point of 55 °C, these building blocks would voluntarily assemble into a 3D fibrous aerogel with interconnected and hierarchical pores. After the subsequent freeze-drying process, stable 3D fibrous aerogels can be obtained. Instead of using some additional binding agents, PCL itself was able to bind nanofibers. Furthermore, the formation process of 3D PCL nanofiber agglomerates through the TISA method was detailed recorded by using a digital camera with an interval of 30 s (Fig. 9a). Before the thermal treatment (Fig. 9a1), shortened PCL nanofibers were homogeneously dispersed in the suspension. After immersing the glass bottle into a water bath at 55 °C for 180 s, the PCL nanofibers would gradually self-agglomerate and form stable 3D fibrous aerogels (Fig. 9a2–a7). This was because the melting point of PCL was 60 °C, and the surface of the PCL nanofibers would become sticky at 55 °C. Then, the bottle was immediately taken out of the water bath and inundated in ice water to avoid further shrinkage and agglomeration (Fig. 9a7). Compared to the conventional freeze-drying or ice-template method to prepare 3D PCL fibrous aerogels, in which the porous structure is generated through the solidified solvent, the porous structure in the 3D PCL fibrous aerogels is formed upon the random self-agglomeration of shortened nanofibers.

2.4.2 Morphology and pore structure. To keep a reasonable fiber morphology, gelatin aqueous solution is generally incorporated into PCL ethanol suspension to promote the uniform dispersion of short nanofibers/tiny pieces of PCL and keep good control of nanofiber self-agglomeration within the process of thermal treatment.[65] The superior features of biodegradability, biocompatibility, and commercial availability have made gelatin widely used to increase the viscosity of the suspension system, while distilled water is added to improve the solubility of gelatin in the mixture system. Then, short nanofibers/tiny pieces of PCL are stabilized by gelatin molecules, and could be uniformly dispersed. Although the samples were rinsed with distilled water several times, some gelatin could remain on the surface of nanofibers, making the nanofibers and the resulting 3D structures hydrophilic. Besides, instead of using additional binding agents, PCL itself can act as a binder during the TISA process. PCL is a cost-effective, biocompatible, and biodegradable polymer. Due to the low degradation rate, PCL serves as a steady binder to stabilize the 3D structure (Fig. 9b–d) in a long tissue regeneration period. PCL also has good spinnability and the ability to blend with various polymers. Besides, owing to the low glass-transition temperature (−60 °C) and melting temperature (60 °C), PCL possesses good mechanical stability. In principle, the TISA method can be applied to other types of polymer nanofibers, if only the heat treatment temperature is close to their melting point. However, the melting temperatures of most polymers are very high (>160 °C), and high boiling point solvents are needed to partially melt or soften the nanofibers. These solvents are usually hard to remove entirely, and the residual solvent may be toxic to cells. In addition, even if high boiling point solvents are used, shortened nanofibers can self-agglomerate together but cannot retain a stable structure because of their high stiffness. Hence, blending PCL with other

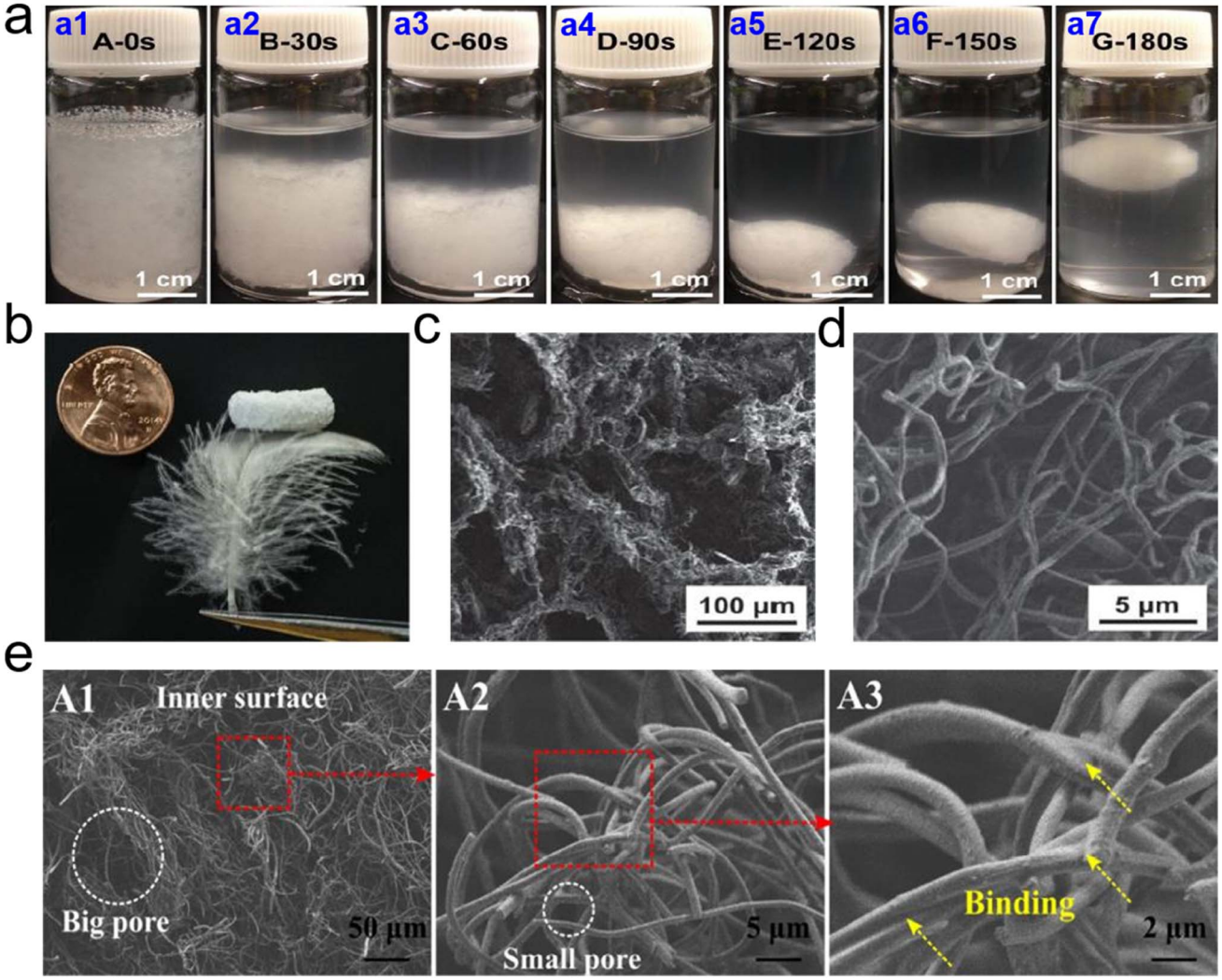

Fig. 9 Microstructure of 3D PCL based fibrous aerogels prepared by TISA process. (a) Photographs of 3D PCL fibrous agglomerate prepared by TISA process: (a1) uniform suspension of short nanofibers and tiny pieces of PCL before thermal treatment; and the suspension after being heated at 55 °C for (a2) 30 s, (a3) 60 s, (a4) 90 s, (a5) 120 s (a6) 150 s, and (a7) 180 s, respectively. (b) Macroscopic morphology, and (c and d) SEM images of 3D PCL fibrous aerogels. Reproduced with permission.[65] Copyright 2015, Wiley-VCH. (e) SEM images showing typical morphologies of the inner surface of 3D CA/PCL fibrous aerogels. Reproduced with permission.[66] Copyright 2018, Elsevier.

polymers and using it as the binding agent to fabricate 3D fibrous aerogels is a promising approach to solve the above problem, thus expanding the application of the TISA method. To further confirm the feasibility of applying PCL as a biodegradable and biocompatible binding agent, 3D CA/PCL fibrous aerogels were successfully fabricated (Fig. 9e).[66] The 3D CA/PCL (mass ratio: 75/25) fibrous aerogels did not contain any toxic crosslinking agent. It is morphologically similar to the natural extracellular matrix, and thus well suitable for cell functions and tissue formation. Therefore, blending PCL with other polymers and using the PCL as the binding agent to develop 3D fibrous aerogels can be an effective approach to expand the application of TISA method, which might considerably enlarge the applications of 3D fibrous aerogels in many tissue engineering areas.

2.4.3 Mechanical properties. As shown in Fig. 10a, the prepared 3D PCL fibrous aerogels showed good mechanical properties, which mainly benefited from PCL that could act as a binder during the TISA process. As mentioned by Fong,[66] in the field of tissue engineering, polymeric biomaterials which possess excellent overall properties are highly desired, whereas no single available polymer can fulfill all the requirements. Therefore, blending two or more polymers could be a promising approach to fulfill these demands and fabricate innovative and highly efficient biomaterials. For example, Yao *et al.*[67] modified PCL with more bioactive PLA and developed 3D PCL/PLA blend (weight ratio: 4/1) fibrous aerogels *via* the TISA method. The resulting scaffolds had high porosity (~95.8%) with interconnected and hierarchically structured pores having sizes ranging from sub-micrometers to ~300 μm (Fig. 10b). Compared to 3D PCL fibrous aerogels, the 3D PCL/PLA blend

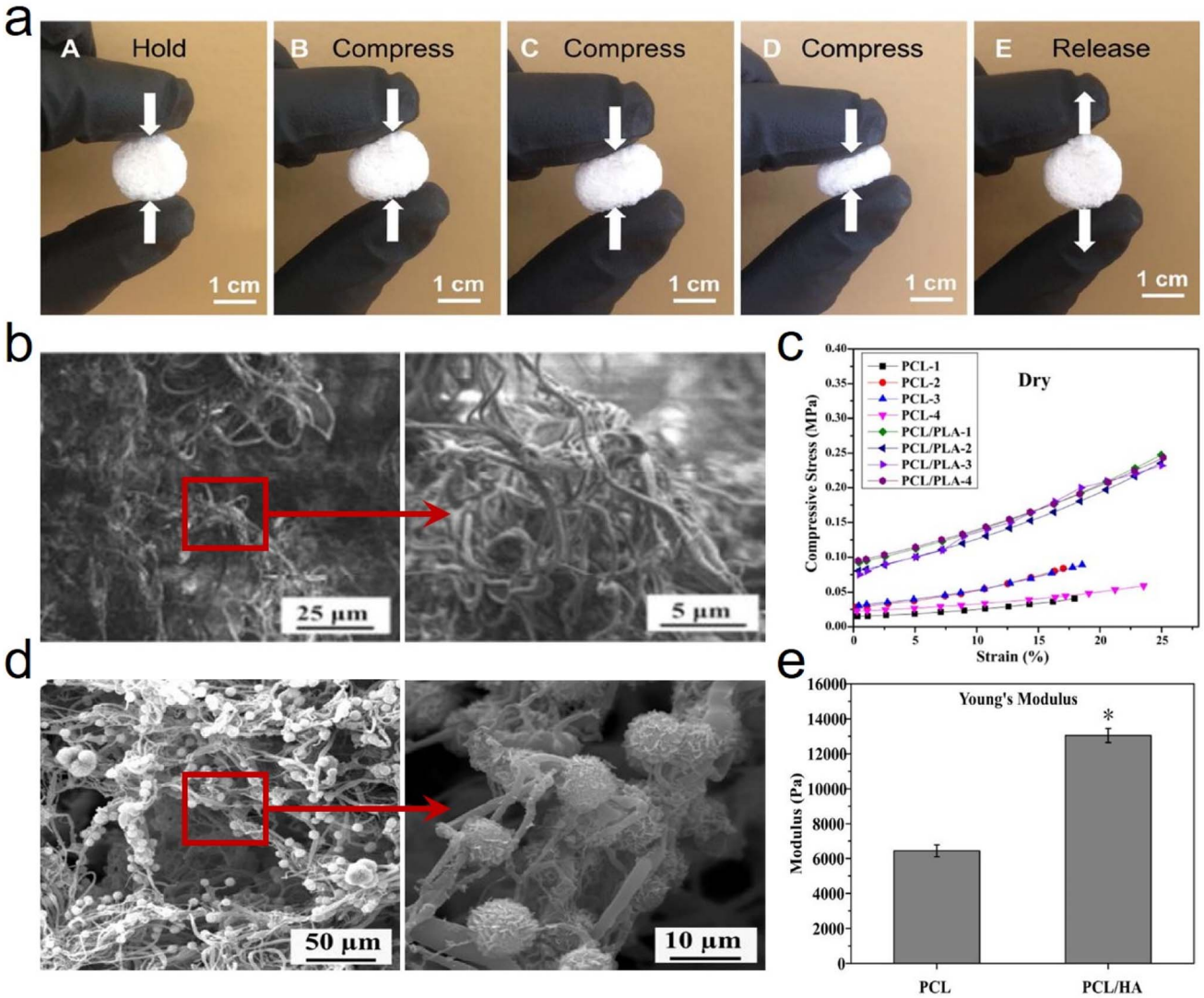

Fig. 10 Reversible compressibility and microstructure of 3D PCL based fibrous aerogels prepared by the TISA process. (a) High compressibility and elasticity of 3D PCL fibrous aerogels. Reproduced with permission.[65] Copyright 2015, Wiley-VCH. (b) SEM images showing the typical morphologies of a 3D electrospun PCL/PLA fibrous scaffold. (c) Compressive stress–strain curves acquired from PCL-3D and PCL/PLA-3D fibrous aerogels under both dry conditions. Reproduced with permission.[67] Copyright 2018, Elsevier. (d) SEM images showing the representative morphologies of PCL/HA coated fibrous aerogels. (e) Young's modulus of PCL/HA-3D fibrous aerogels. Reproduced with permission.[68] Copyright 2017, Elsevier.

fibrous aerogels had higher mechanical properties (Fig. 10c) and *in vitro* bioactivity. To date, various biologically derived polymers (including proteins, polysaccharides, and polyhydroxyalkanoates) and synthetic polymers (including polyesters, water-soluble polymers, and conductive polymers) have been blended with PCL for making electrospun polymer blend nanofibers.[68] It is envisioned that all of these polymers could be fabricated into 3D fibrous aerogels by first making blend nanofibers with PCL followed by processing *via* the TISA method; hence, a large number of electrospun 3D fibrous aerogels would be available for various tissue engineering applications.

Besides, cells interact with scaffolds primarily through the surface of scaffold materials, which can be controlled/tailored upon adjusting the surface chemical properties. Furthermore, incorporating functional fillers directly into the scaffold nanofibers as a surface modification is another effective approach to achieve chemical specificity and recognition, which can lead to desired specific intracellular signaling. Fong *et al.*[68] functionalized 3D PCL fibrous aerogels with hydroxyapatite (HA) (Fig. 10d) and bone morphogenic protein (BMP)2 signaling activator phenamil, which provided a favorable osteogenic niche for bone formation at low doses of BMP2. The Young's modulus was measured after PCL fibrous aerogels were modified with HA, yielding an increase from 6438 ± 342 N to 13 032 ± 404 N (Fig. 10e). This increased Young's modulus was mainly ascribed to the incorporation of HA which would increase the stiffness/modulus and would not distinguishably vary the ductility/elasticity of the resulting PCL/HA-3D fibrous aerogels. Correspondingly, it's believed that several other surface

modification methods on PCL nanofibers, including surface activation, chemical grafting copolymerization, and biomimetic modification, could also be adopted to modify 3D PCL fibrous aerogels and improve many performance characteristics including mechanical properties.

2.5 Carbonization

2.5.1 Formation mechanism. Ultralight carbonaceous aerogels are attractive because of their excellent advantages of low density, a large surface area, high porosity, good electrical conductivity, and chemical inertness, which have been widely studied in electrical, biomedical, and energy applications.[69–72] Correspondingly, the developed shaped 3D fibrous aerogels can undergo an extra processing step of "carbonization" to obtain 3D carbon nanofiber aerogels (CNFAs). During this process, the 3D fibrous aerogel is exposed to high temperature (600–1450 °C) and ambient pressure with an inert atmosphere of N_2 or Ar to decompose oxygen and hydrogen moieties in a polymeric chain and enriches the fibrous networks with pure carbon moieties.[71–75] Until now, there have been three major approaches to converting shaped 3D fibrous aerogels into CNFAs. The first one is adding some adhesive, which acted as a "solder" to "weld" adjacent nanofibers to improve the mechanical properties of CNFAs.[76] The second one is utilizing thermostable fibrous aerogel frameworks as templates to

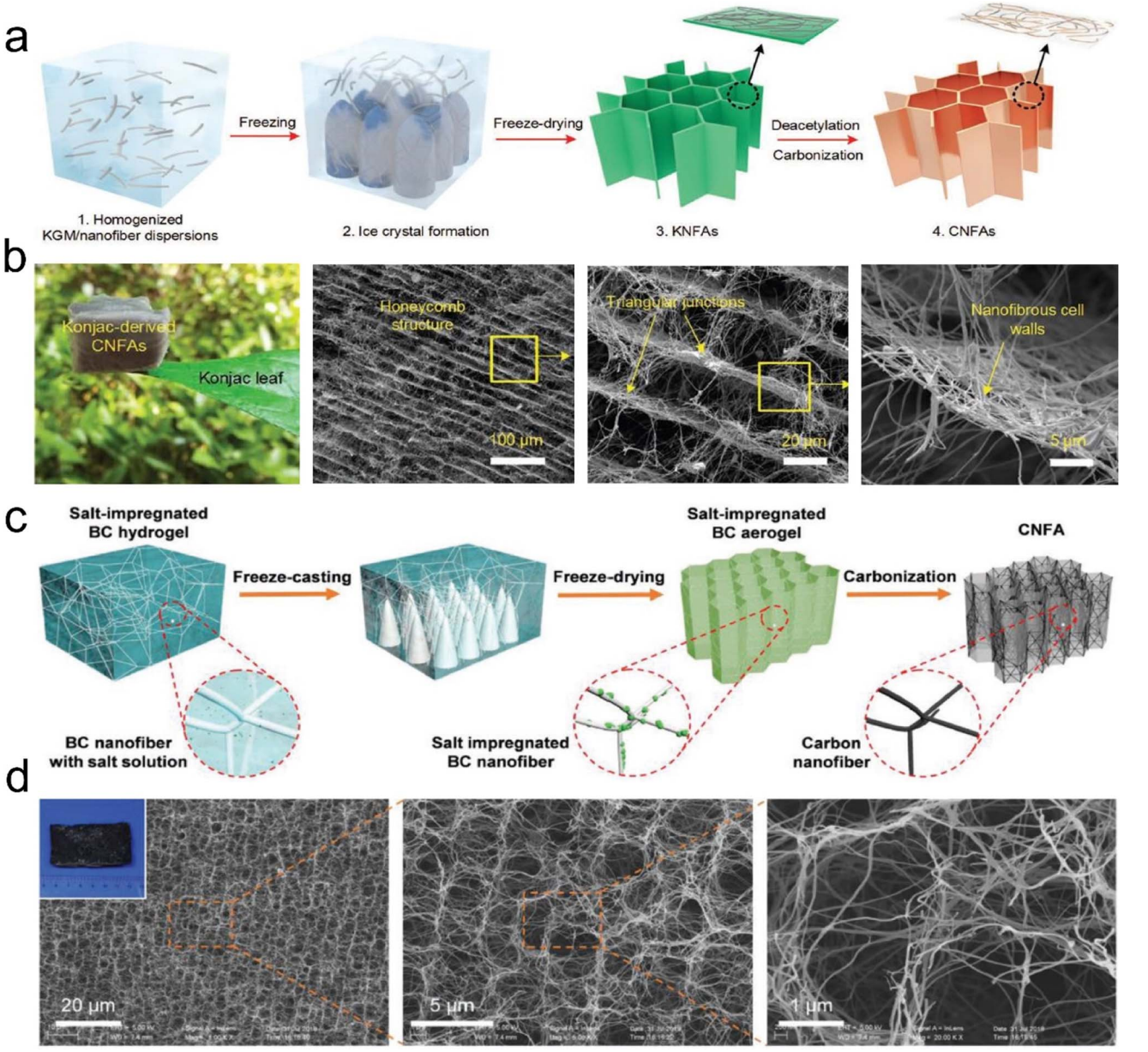

Fig. 11 Preparation process and microstructure of CNFAs. (a) Schematic showing the synthetic steps for preparing CNFAs. (b) SEM images of CNFAs at various magnifications. Reproduced with permission.[60] Copyright 2017, Wiley-VCH. (c) Schematic illustration of the fabrication processes of CNFAs. (d) SEM images of CNFAs, demonstrating that the CNFAs fully inherited the hierarchical structure from BC. Reproduced with permission.[77] Copyright 2019, Wiley-VCH.

achieve the non-agglomerated assembly of carbonaceous biomass on the fiber and enhance the mechanical and elastic resilience of CNFAs.[59] The third one is incorporating some inorganic salts to improve the char yield and thermal stability of CNFAs.[77] In the following section, we will explain these processes with some representative cases.

2.5.2 Morphology and pore structure. The effective properties of carbonaceous aerogels are dictated both by their cellular architectures (*i.e.*, the spatial geometry of voids and the solid) and the structure of the carbonaceous constituents (*e.g.*, scale and continuity). A large number of studies show that 3D fibrous aerogels can keep a relatively stable internal network structure through high-temperature carbonization.[73–75] For example, Zhang *et al.*[76] reported PAN/PVP derived CNFAs. The freeze-dried PAN/PVP fibrous aerogels were oxidized at 240 C for 1 h, and carbonized in nitrogen at 700, 800, 900, and 1000 °C for 2 h to fabricate CNFAs. PVP acted as an adhesive to bond adjacent nanofibers, and improve the mechanical stability of CNFAs. Si *et al.*[60] demonstrated a sustainable strategy for creating superelastic CNFAs with an ordered honeycomb-like structure using a novel biomass KGM and flexible SiO_2 nanofibers (Fig. 11a). The KGM precursor was converted to 1D carbonaceous nanofibers on the SiO_2 nanofiber surface. Specifically, freeze-dried KGM/SiO_2 fibrous aerogels (KNFAs) were heated at 90 °C to fully deacetylate the KGM, and then carbonized at 850 °C to form carbonaceous fibrous networks consisting of SiO_2/carbon core–shell nanofibers, which had a final carbon content of about 40 wt%. After the carbonization process, the KGM was gradually decomposed, and nanofibers were highly entangled and assembled into a bulk aerogel with a honeycomb cellular structure (Fig. 11b). Yu *et al.*[77] reported morphology-retained carbonization of bacterial cellulose (BC) by engineering the pyrolysis chemistry of BC with conventional inorganic salts and preparing CNFAs that perfectly inherit the

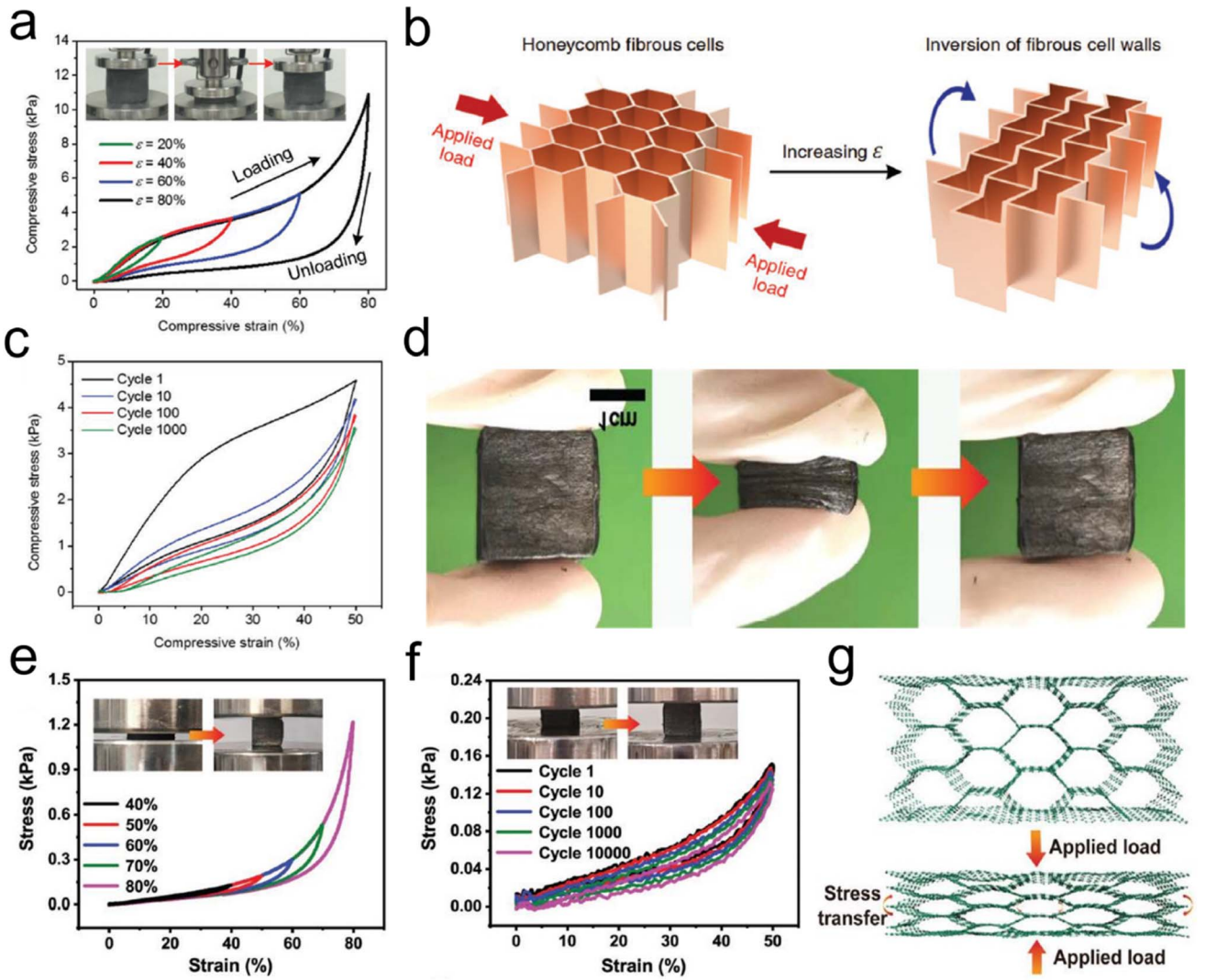

Fig. 12 Reversible compressibility of CNFAs. (a) Compressive σ *versus* ε curves for CNFAs along the loading direction. (b) Schematic demonstration of the inversion of the fibrous cell walls with compressive ε. (c) 1000 cyclic fatigue compressive test with an ε of 50%. Reproduced with permission.[60] Copyright 2017, Wiley-VCH. (d) Compression and recovery process of typical CNFAs. (e) Stress–strain curves of CNFAs at different compression strains. (f) Stress–strain curves at 80% strain for 100 cycles, and (g) schematic illustration showing the compressive deformation for the CNFAs. Reproduced with permission.[80] Copyright 2022, Wiley-VCH.

hierarchical structures of BC from macroscopic to microscopic scales (Fig. 11c). The integrated 3D fibrous structure of BC was formed naturally in the biological fermentation process,[78] while the honeycomb-like structure was induced by the freeze-drying process. After carbonization at high temperature, importantly, the hierarchical structure of BC (that is, the honeycomb cellular structure and the nanofiber junction structure) was inherited perfectly in the CNFAs (Fig. 11d). The inorganic salts could improve the CNFA yield of BC. Significantly, the CNFA yield increased from 7.3% (pure BC) to 31.4% when 10.3 wt% $NH_4H_2PO_4$ was incorporated. Chen *et al.*[79] reported the production of 3D interconnected N-self-doped carbon nanofiber (NCNF) aerogels with a silk cocoon-like node network by *in situ* growth of zeolitic imidazolate framework (ZIF-8) nanocrystals on BC, followed by a dry-freezing process and subsequent thermal treatment. During the carbonization of BC@ZIF-8 fibrous aerogels, plentiful micro- and meso-porous carbons were generated as energy storage nodes, while retaining the ideal shape and structure of ZIF-8 nanocrystals, and the BC was converted to highly conductive carbon nanofibers, forming 3D interconnected frameworks with a silk cocoon-like node morphology. Besides, Liu *et al.*[80] developed a bidirectional freezing and subsequent carbonization strategy to prepare ordered porous CNFAs with excellent mechanical compressibility and superhydrophilicity by combining cellulose nanofibers, CNTs, and reduced graphene oxide (RGO). After the carbonization process in flowing N_2, the final CNFAs were obtained, which contained a regular honeycomb porous structure with an aperture of about 50 μm.

2.5.3 Mechanical properties. CNFAs featuring a large surface area, high porosity, and good electrical conductivity have been extensively used in electrical fields, including supercapacitors, lithium secondary batteries, and flexible pressure sensors.[74,75] To construct an appropriate cellular architecture that can achieve the promising properties of CNFAs, various available cellular materials have been examined, and the high structural efficiency of natural honeycomb has attracted more researchers. Typically, Si *et al.*[60] reported that the CNFAs possessed robust mechanical properties with a structure allowing for large deformations without cracks (Fig. 12a). Similar to honeycomb-structured materials,[81,82] three main regimes were observed in Fig. 12a: an elastic linear regime for $\varepsilon < 20\%$ with an elastic modulus of 2.3 kPa corresponding to the elastic bending of the cell walls, a plateau regime for $20\% < \varepsilon < 60\%$ following elastic buckling of the cell walls, and a densification regime for $\varepsilon > 60\%$ with σ rising sharply. The maximum σ was 10.6 kPa at 80% strain, which was superior to those of other biomass-derived aerogels with similar densities.[83] Furthermore, the CNFAs were subjected to a fatigue hysteresis test for 1000 compressive cycles at a large ε of 50% at 1 Hz (Fig. 12c), and they showed relatively minor plastic deformations (4.3% in the 1000th cycle) at that level of strain. These results were ascribed to the inversion of the fibrous cell wall which occurred isotropically under compressive stress (Fig. 12b). Similarly, Liu *et al.*[80] utilized the bidirectional freezing strategy for preparing ordered porous CNFAs with excellent mechanical properties (Fig. 12d). The prepared CNFAs could undergo a broad compression strain owing to the ordered layered structure. The stress–strain curves at 40–80% strain gradually steepened with a higher compression strain (Fig. 12e). This was because the distance between the carbon aerogel sheets decreased with increasing strains in the initial elastic region under a low strain ($\varepsilon < 60\%$), but the microstructure remained stable. In the densifying region under high strains ($\varepsilon >$

Table 1 Summary of the preparation methods and their characters

Preparation method	Microstructure	Process parameters	Typical characteristics	Advantages	Disadvantages	Ref.
Electrospinning	Randomly	Spinning solution, high voltage power, collector	Lightweight, high specific surface area, large porosity, flexible, good tensile properties	Abundant raw materials, diverse fiber morphology (*e.g.*, core–shell and porous)	Electrostatic field interference, time-consuming, difficult solvent recovery	27
Solution blow spinning	Randomly	Spinning solution, high-velocity gas flow, collector	Lightweight, high specific area, large porosity, flexible, elastic, mechanical stability	Abundant raw materials, high-production, safety	Difficult solvent recovery	35
Freeze-drying	Randomly, anisotropic	Fiber dispersion, dispersion medium, binding agent	Lightweight, high specific surface area, large porosity, flexible, elastic, good mechanical stability	Abundant raw materials, simple process, high-production	Low-temperature, time-consuming	56
Thermally induced self-agglomeration	Randomly	Short polycaprolactone nanofibers	Lightweight, high specific surface area, large porosity, stiff, good mechanical stability	Sample process, without binding agents	Less raw materials, toxic solvent	65
Carbonization	Randomly, anisotropic	Shaped aerogels, high-temperature	Lightweight, high specific surface area, large porosity, elastic, flexible, good mechanical stability, electro-conductive	Abundant raw materials, novel function (*e.g.*, electrical conduction)	High-temperature (600–1400 °C), complex process	77

60%), the dense stacking within CNFAs led to a rapid increase in the elastic modulus and stress. Moreover, the prepared CNFAs could even withstand long-term compression for 10 000 cycles, with a high-stress retention of 86.1% at 30% and 85.3% at 50%, which further verified the superior compressibility and elasticity of CNFAs (Fig. 12f). The compressible and elastic mechanism of the CNFAs is proposed in Fig. 12g to illustrate their excellent structural stability. In the structural model, the regular honeycomb structure of CNFAs made it possible to avoid slipping and splitting along the perpendicular direction of compression, which was more conducive to the storage of elastic energy. Besides, Zhang *et al.*[76] prepared PAN/PVP derived hybrid CNFAs, in which PVP could act as an adhesive or "solder" to "weld" adjacent nanofibers. Correspondingly, the CNFAs could withstand a compressive strain (ε) of up to 80% and recover to their original height upon releasing the compression stress (σ). Cyclic compression tests of the CNFAs were performed by applying 100 loading–unloading compression cycles at a constant strain of 50%. Therefore, CNFAs featuring excellent structural stability are considered promising candidates do use in electronic fields.

In general, the recently reported fabrication strategies, involving electrospinning, solution blow spinning, freeze-drying, thermally induced self-agglomeration, and carbonization techniques have been widely adopted to prepare various 3D fibrous aerogels. Table 1 summarizes the advantages and disadvantages of the synthesis methods and the corresponding physical parameters, which provides great guidance to fully understand the differences among the preparation methods.

3. Applications of 3D fibrous aerogels

3.1 Air pollutant filtration

Air pollution caused by fine particulate matter (PM) and toxic gases has become an increasing public health hazard globally. PM, as a complex mixture, is typically categorized as $PM_{0.3}$, $PM_{2.5}$, and PM_{10}, which refer to particle sizes below 0.3, 2.5, and 10 μm, respectively. Among them, $PM_{0.3}$ is especially harmful because it can travel long distances, penetrate small airways, and carry various bacteria/viruses. To achieve efficient removal of PMs and toxic gases, the design of air filters with high selectivity and low cost has attracted considerable attention.[84,85] Generally, the fiber diameter for air filters needs to be considered for achieving the efficient capture of PMs. For $PM_{0.3}$ and $PM_{2.5}$, the diameter range of fibers is usually 20–200 nm and 50–2000 nm, respectively, so that the filter material can achieve a filtration efficiency greater than 99.99%.[86,87] To date, the existing fibrous filter media (*e.g.*, melt-blown polypropylene, PI, *etc.*) often suffer from an extremely low filtration efficiency toward poisonous $PM_{2.5}$ and $PM_{0.3}$ due to their microsized fiber diameters. Alternatively, electrospun fibrous membranes are deemed effective in capturing PMs based on their small fiber diameters, tunable porous structure, and ease of preparation from various materials. However, the electrospun air filtration materials exhibit a high-pressure drop due to the dense packing of nanofibers (with a limited porosity of <90%), finally giving rise to large energy consumption. At the forefront of advanced materials, a 3D fibrous aerogel featuring a large specific surface area, high porosity, and abundant interconnected channels, is developing into a more favorable candidate for air filters than 2D membranes.

The current relevant reports mainly focus on using electrospun nanofiber membranes to construct 3D fibrous aerogels for improving air filtration efficiency and selectivity. For example, Hu *et al.*[88] prepared silk nanofibril (SNF) aerogels with controlled structures and excellent mechanical resilience. The nanofibril network and hierarchical cellular structure of the prepared aerogels (Fig. 13a) were tuned by the assembly of SNFs and foreign PVA. The SNF aerogels exhibited a high filtration efficiency of 98% and quality factor towards $PM_{0.3}$ (Fig. 13b and c), which were far superior to those of PP nonwovens and commercial masks when the PM had sizes of 0.3–3 and 5–10 μm. Qian *et al.*[89] developed electrospun PI nanofibers as building blocks to construct PI fibrous aerogels with a hierarchically porous architecture, which achieved a capture efficiency of 99.9% for $PM_{2.5}$ and a low-pressure drop of 177 Pa. However, once massive particles are deposited or subjected to high airflow velocity, less solidity may cause the collapse of the cellular structure, as evidenced by the low compressive stress ($\approx$1.4 kPa at a strain of 60%) and modulus (6.1 kPa) of PI fibrous aerogels. Moreover, electrospun fibrous aerogels derived from PI and other materials (*e.g.*, PVA) all suffer from a mono-assembling structure parallel to the filtering direction, which would cause the inability to collect polydisperse fine particles as a uniform deposition pattern, resulting in a short service life.[90] To address these issues, Si *et al.*[91] proposed a biomimetic and bottom-up strategy to prepare superelastic and thermostable fibrous aerogels as cascade filters through assembling semi-interpenetrating polymer network (semi-IPN)-based nanofibers into a gradient architecture. The mechanical properties of fibrous aerogels were improved by tailoring the chain flexibility of heat-resistant semi-IPNs. The resultant semi-IPN-based gradient fibrous aerogels exhibited a high compressive stress of 7.9 kPa and high filtration efficiency of 99.97% towards $PM_{0.3}$. Similarly, Wang *et al.*[92] reported the preparation of cage-like structured aerogels (CSAs) by combining electrospun silica nanofibers, BC nanofibers, and the hydrophobic Si–O–Si elastic binder, which aimed at achieving excellent air filtration performance and the effective inactivation of airborne pathogens simultaneously. Fig. 13d demonstrates the antibacterial and antiviral air filtration process of the aerogels. When contaminated air came into contact with CSAs-Cl, the fine BC nanonets would intercept viruses and bacteria; meanwhile, the aerogels could release oxidative chlorine and kill pathogens by directly reacting with the vital bacterial cell constituents (such as enzymes and proteins). The resultant fibrous aerogels showed high filtration performance toward $PM_{0.3}$ (>99.97%, 189 Pa), and excellent antibacterial and antiviral activity (6 log reduction within 5 min contact) (Fig. 13e–h). These results all indicated that 3D fibrous aerogels could serve as a scalable biocidal air filter that not only intercepts but also effectively kills pathogens in infected air, revealing their practicability in antimicrobial air filtration. Zhang *et al.*[93] reported a novel hydroxyapatite (HAP) nanowire-based inorganic aerogel with

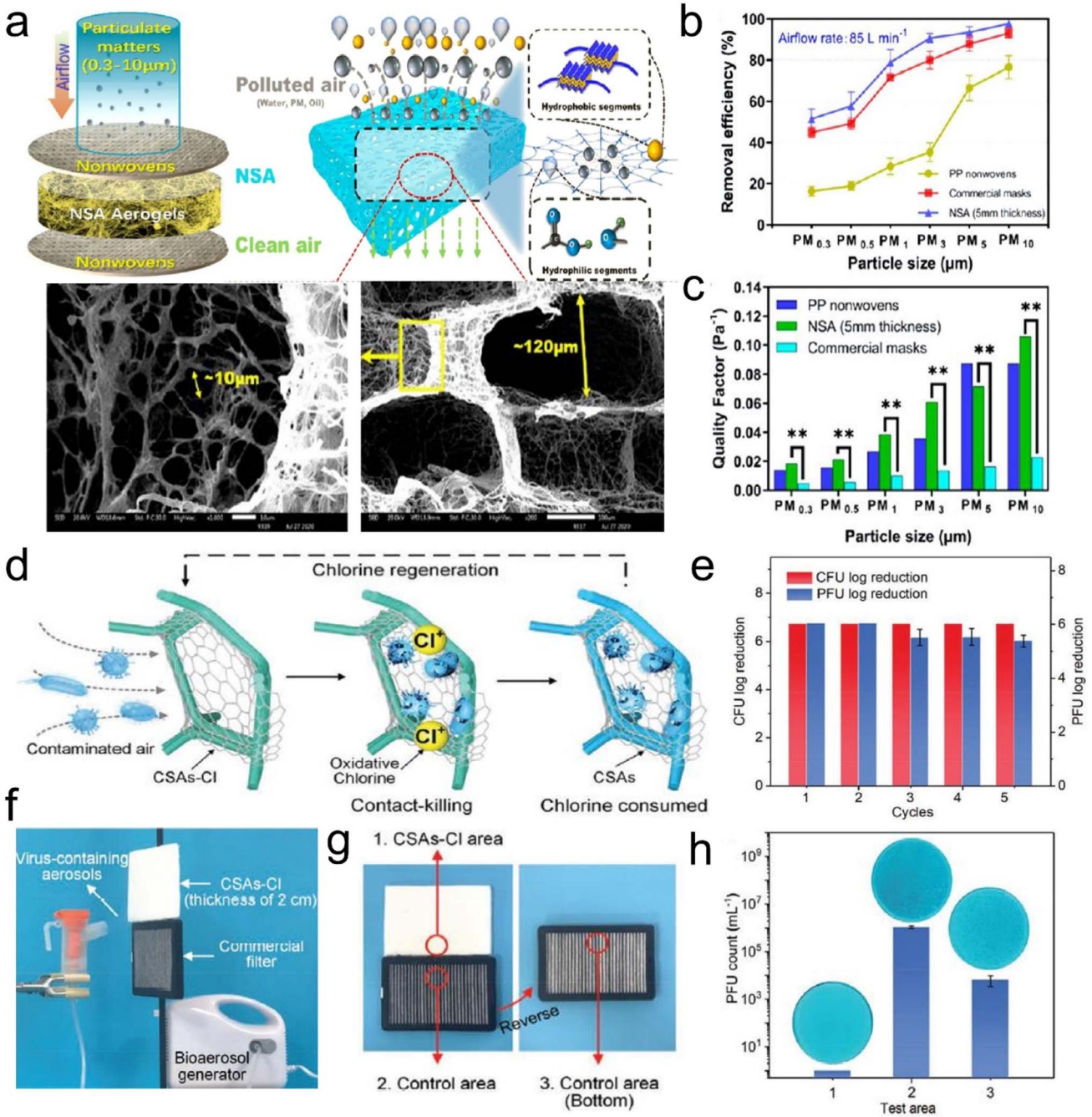

Fig. 13 3D fibrous aerogels used in air filtration. (a) Illustration of the contaminants captured by SNF aerogels. (b) Removal efficiency at 85 L min^{-1} for differently sized particles. (c) Quality factor of the three kinds of materials at 85 L min^{-1} for differently sized particles. Reproduced with permission.[88] Copyright 2021, American Chemical Society. (d) Illustration showing the air filtration procedure of the aerogels. (e) Renewable antibacterial and antiviral properties of CSAs-Cl. (f) Virus-containing aerosol generator and the antiviral test using an aerogel and 3 M filter. (g and h) The antiviral properties of the selected three areas of the filters. Reproduced with permission.[92] Copyright 2021, Wiley-VCH.

excellent elasticity, which was highly porous (porosity ≈ 99.7%) and ultralight (density 8.54 mg cm^{-3}, which is about 0.854% of water density). The as-prepared hydrophobic HAP nanowire aerogel filter had high PM filtration efficiency, low-pressure drop, good mechanical properties, and high biocompatibility; thus, it was promising for applications in breathing masks and air purifiers. Therefore, these advanced research studies have demonstrated that the development of 3D fibrous aerogels brings about an improved performance in the capture of air pollutants, which is ascribed to a combination of properties, such as large and highly open porosity, high specific surface area, polar–polar interaction with PMs, abundant cavities and efficient gas adsorption sites.

3.2 Thermal insulation

Decreasing heat transfer through advanced thermal insulators is an effective way to improve energy efficiency and reduce the world's total energy consumption.[94] Thermal insulation is also urgently needed for many personal thermal protection systems in harsh environments. Thermal insulators are generally defined as materials that retard the heat flow through conduction, convection, and radiation.[95–97] Trapped air pockets in the cellular fibrous structure of aerogels provide a region of insulation that not only effectively reduces the heat transfer *via* convection but also obstructs heat conduction pathways.[98] During heat convection, a bulk stream of gas driven by buoyancy and temperature differences moves around, but in 3D fibrous aerogels, with a large number of air-filled pockets, there is a small density difference to drive heat convection. The high surface area of the tortuous pores filled with low-density air blocks the heat conduction path and resists gas flow by minimizing its movement. Besides, the physically entangled and/or chemically crosslinked networks for 3D fibrous aerogels can considerably avoid stress concentration and show mechanical and flexible behavior. Thus, 3D fibrous aerogels are developing into a more favorable candidate as thermal insulators.

Organic polymer nanofiber-assembled 3D fibrous aerogels have shown promising thermal insulation properties. For example, Tuo *et al.*[99] reported a bottom-up strategy for the preparation of 3D ANF aerogels by a vacuum-assisted self-assembly technique. The obtained ANF aerogel was pressed to 25% of the original height ($\varepsilon = 75\%$), which could recover to 59.6% and 52.4% of the original height in the axial direction and the radial direction, respectively. The thermal conductivity (Fig. 14a) of the ANF aerogel in the radial and axial directions (25 °C) was 0.0418 ± 0.0006 and 0.0372 ± 0.0004 W m^{-1} K^{-1}, respectively. Jiang *et al.*[100] prepared hierarchically 3D fibrous aerogels using PI as a high-temperature stable polymer and PAA

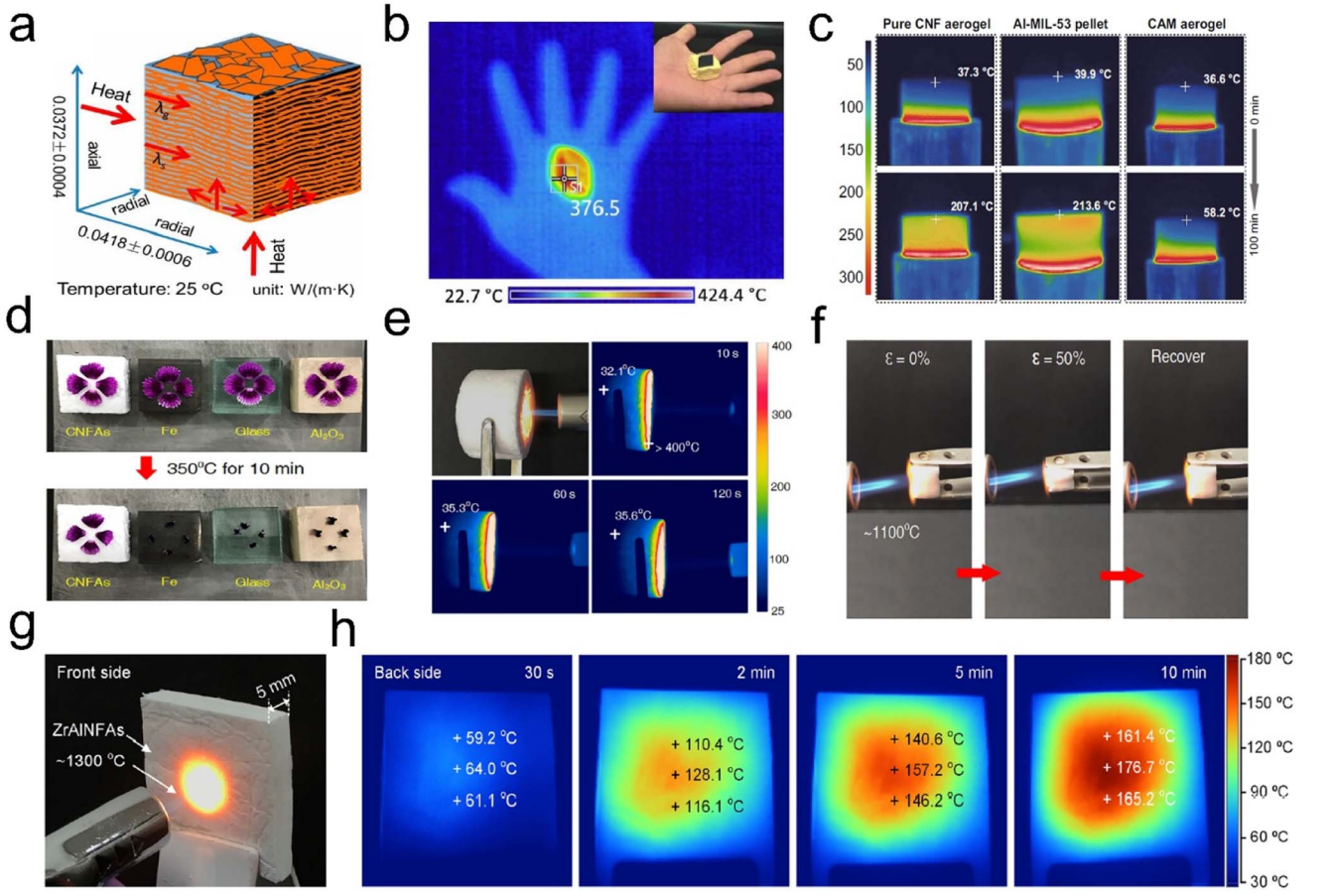

Fig. 14 Thermal insulation performance of 3D fibrous aerogels. (a) Thermal conductivity of the ANF aerogel in different directions. Reproduced with permission.[99] Copyright 2019, American Chemical Society. (b) Infrared camera image showing the thermal insulation of the PI aerogel: a hot iron plate (~376 °C) was held on hand with the assistance of the PI aerogel. Reproduced with permission.[100] Copyright 2017, American Chemical Society. (c) Infrared side-view images of the pure cellulose nanofiber aerogel, the pure Al-MIL-53 pellet, and the CAM aerogel, with the temperature of the top surfaces. Reproduced with permission.[101] Copyright 2020, Springer Nature. (d) Thermal insulation capacity of the ceramic fibrous aerogels compared with those of Fe, SiO_2, and Al_2O_3 materials for protecting fresh petals from withering. (e) Optical and infrared images of ceramic fibrous aerogels on a 350 °C heating stage for 30 min. (f) Optical and infrared images of ceramic fibrous aerogels exposed to a butane blowtorch for 120 s. Reproduced with permission.[56] Copyright 2020, Springer Nature. (g) Optical photograph of the front side subjected to a butane blowtorch flame. (h) Infrared images of the back side during a 10 min heating process. Reproduced with permission.[111] Copyright 2020, American Chemical Society.

as a binder. The 3D fibrous aerogels with a density of 10.1 mg cm^{-3} showed a low thermal conductivity of 0.026 W m^{-1} K^{-1} and thermal diffusivity of 1.009 mm^2 s^{-1}. As shown in Fig. 14b, a hot iron plate (~376 °C) could be held on hand with the assistance of the PI aerogel, and the gradient distribution of temperature from the plate to the 3D fibrous aerogels was observed when the PI aerogel was put on a heating plate (~400 °C). Zhou *et al.*[101] prepared hybrid aerogels (cellulose nanofiber@Al-MIL-53, CAM) by a stepwise assembly approach involving the coating and cross-linking of cellulose nanofibers with continuous nanolayers of MOFs. The CAM aerogels had a cellular network structure and hierarchical porosity, which endowed the aerogels with a relatively low thermal conductivity of ~40 mW m^{-1} K^{-1}. As shown in Fig. 14c, a 1 cm-thick section of the CAM aerogel was placed on a 300 °C heating stage. The temperature at the top surface of the Al-MIL-53 pellet and the pure cellulose nanofiber aerogel reached 207.1 and 213.6 °C, respectively. Remarkably, the temperature on the top surface of the CAM aerogel only slightly increased to 58.2 °C. However, some fibrous aerogels assembled from organic polymer nanofibers could not withstand high-temperature conditions (>900 °C), showing structural collapse and volume shrinkage to some extent. Therefore, 3D fibrous aerogels with sufficient mechanical robustness (both high strength and superelastic) and excellent high-temperature resistance are the critical roadblocks to their reliable application under industrial, aerospace, and even extreme environmental conditions.[102–104]

Recently, the emerging ceramic fibrous aerogels have become the most attractive candidates for thermal insulation because of their low thermal conductivity and excellent fire and corrosion resistance, which can bear extreme temperatures.[104–109] For example, Liu *et al.*[56] reported a scalable strategy to develop superelastic ceramic fibrous aerogels by combining SiO_2 nanofibers and aluminoborosilicate (AlBSi) matrices. The thermal conductivity of the aerogel was 0.025 W m^{-1} K^{-1}, which was closed to that of air under ambient conditions (0.023 W m^{-1} K^{-1}). As shown in Fig. 14d, fresh flower petals placed on the top of the ceramic fibrous aerogels only slightly shrivel up after being on a hot stage (350 °C) for 10 min, whereas other ceramic materials such as iron, glass, and Al_2O_3 scorch and carbonize these petals. The ceramic fibrous aerogels (15 mm thick) had superior thermal insulation against a high-temperature butane blowtorch flame, showing a relatively low temperature of 35 °C at the far end of the aerogels (Fig. 14e). The high-temperature elasticity and fire resistance of the ceramic fibrous aerogels were further assessed by *in situ* compression testing in the flame of a butane blowtorch (~1100 °C). As depicted in Fig. 14f, no ignition or structural collapse was observed when the aerogels were exposed to those high-temperature flames; moreover, they still exhibited good elastic resilience after several compression cycles upon flame burning, highlighting the temperature-invariant superelasticity. Similarly, Dou *et al.*[110] synthesized a hierarchical cellular structured silica fibrous aerogel using SiO_2 nanofibers and SiO_2 nanoparticle aerogels (SNAs) as the matrix and SiO_2 sol as the high-temperature nanoglue. The as-prepared ceramic fibrous aerogels showed ultralow thermal conductivity (23.27 mW m^{-1} K^{-1}) and temperature-invariant superelasticity from −196 to 1100 °C, making them ideal for thermal insulation applications. Besides, Si *et al.*[111] reported the facile creation of lamellar multiarch structured ZrO_2–Al_2O_3 fibrous aerogels (ZrAlNFAs) with temperature-invariant mechanical robustness through combining flexible ZrO_2–Al_2O_3 nanofibers with $Al(H_2PO_4)_3$ (AHP) matrices. Fig. 14g presents the optical photograph of the front side of ZrAlNFAs (thickness of 5 mm), which have been subjected to flames of about 1300 °C from a butane blowtorch. The back-side surface of the ZrAlNFAs showed a gentle increase in temperature from 60 °C for 30 s, 160 °C for 5 min, and finally an almost constant 180 °C with further heating after 10 min (Fig. 14h). The lamellar structure, high porosity (>98%), and all-ceramic components endowed the ZrAlNFAs with temperature-invariant compressibility, high fire resistance up to 1300 °C, a thermal conductivity as low as 0.0322 W m^{-1} K^{-1}, and high-temperature thermal insulation performance. Therefore, these research studies demonstrate that ceramic fibrous aerogels can be recognized as a promising alternative to the existing thermal insulation materials under extreme environments.

3.3 Pressure sensors

With the foreseeable prosperity of artificial intelligence, high-performance pressure sensors with light weight, mechanical compliance, high sensitivity, fast response, a wide response range, and stability have emerged, promising a myriad of applications such as artificial prosthetics, smart robots, electronic skin, and wearable electronics.[112–115] Aerogels with electricity properties are considered a promising material for pressure sensors combining high conductivity and mechanical properties. So far, CNTs or graphene aerogels/sponges have been widely reported as pressure sensors. However, they typically possess either large (tens of micrometers) or small (several micrometers or smaller) pores but not both, whereas the hierarchical structures that possess wide pore size distributions from small to large pores are desired for wide strain range strain/pressure sensors. Recently, fibrous aerogels with a 3D architecture are regarded as the most ideal candidate for pressure sensors because of their low density, high porosity, and excellent elasticity. Typically, Si *et al.*[60] prepared superelastic CNFAs with an ordered honeycomb-like structure by combining KGM and flexible SiO_2 nanofibers. This excellent mechanical stability could make the aerogels sense dynamic pressure with a wide pressure range and high sensitivity, which enabled real pressure signals (*e.g.*, human blood pulses) to be monitored in real time and *in situ* (Fig. 15a and b). Hou *et al.*[116] reported PI-derived CNFAs with high fatigue resistance and excellent flexibility, and the aerogels showed elasticity-dependent electrical resistance as piezoresistive stress sensors. However, the conductivities of these 3D CNFAs were deeply affected by the carbonization process and might not be accurately regulated. For the compressive strain sensor, high conductivity could lead to small change of conductivity and thus low sensitivity in sensing applications. Fong *et al.*[117] demonstrated a promising strategy for preparing highly porous 3D fibrous aerogels with tunable conductivity for making tactile pressure sensors.

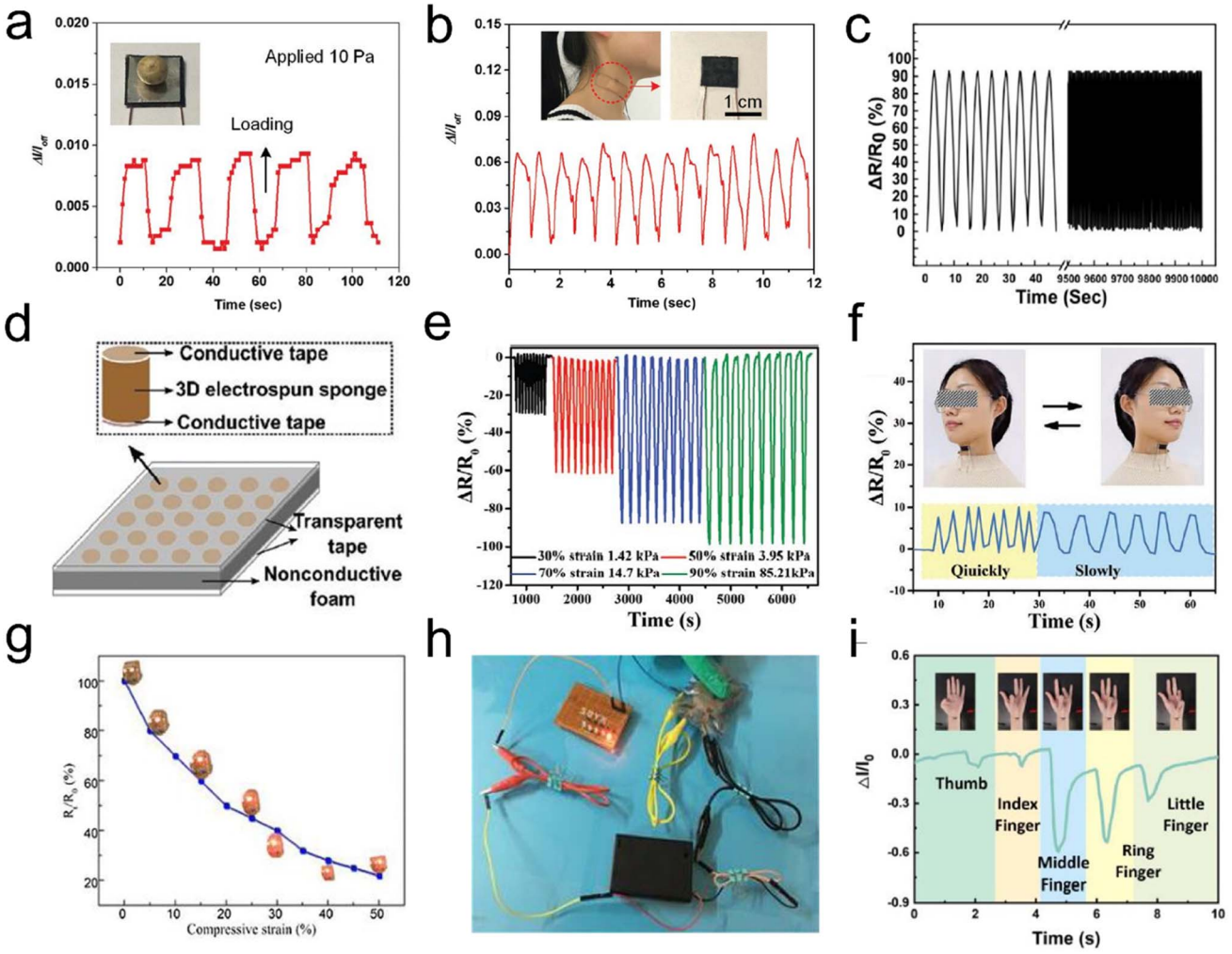

Fig. 15 3D fibrous aerogels used in pressure sensors. (a) Response and relaxation of the pressure sensor upon loading and unloading of a pea with a pressure of 10 Pa. (b) Measurement of the human neck pulse under normal conditions, indicating 72 beats per min. Reproduced with permission.[59] Copyright 2016, Wiley-VCH. (c) The resistance change of the 3D conductive aerogels. (d) Schematic of a proof-of-concept matrix of the sensor array. Reproduced with permission.[117] Copyright 2017, Royal Society of Chemistry. (e) Cyclic piezoresistive sensing performances of the PINF/MXene aerogel under different compression strain/pressure levels. (f) Sensing performances of the PINF/MXene aerogel served as a pressure sensor for the real-time detection of head shaking. Reproduced with permission.[118] Copyright 2021, Wiley-VCH. (g) The R_t/R_0 – compressive strain curve of the 3D fibrous aerogels. (h) Photographs of a circuit based on compressed 3D fibrous aerogels at different strains with a light lamp. Reproduced with permission.[120] Copyright 2017, Elsevier. (i) Bending signal of different fingers. Reproduced with permission.[121] Copyright 2022, Elsevier.

Within this design, the PAN and PI nanofibers showed mechanical resilience, and electrospun carbon nanofibers provided tunable electrical conductivity. The resistance of the 3D fibrous aerogels could vary from ~260 kΩ to ~200 Ω with the addition of carbon nanofibers. Under compressive strain, the resulting sensors based on these aerogels had high sensitivity over a wide range of compressive strain and stability (Fig. 15c). The tactile pressure sensor array (Fig. 15d) of 3D fibrous aerogels represented the advanced applications of these materials, indicating a promising candidate for the design of highly sensitive tactile sensing devices. This provides a new approach for designing 3D porous fibrous aerogels or aerogels with multiple functions by incorporating functional materials and fragmented nanofibers as building blocks.

For the purpose of preparing high-sensitivity flexible pressure sensors, active materials are generally considered. Different choices of active materials have an immediate and profound influence on their sensing performance. The traditional pressure sensors based on metals or semiconductors face the problems of poor flexibility and a narrow pressure range, which greatly limit their application in wearable devices. Currently, some conductive nanofillers (*e.g.*, MXene, graphene, CNTs, polypyrrole (Ppy), silver, copper, *etc.*) have been regarded as active materials, which strongly promote the development of flexible pressure sensors. Liu *et al.*[118] developed a conductive polyimide nanofiber (PINF)/MXene hybrid aerogel with a "layer-strut" bracing hierarchical fibrous cellular structure. Benefiting from the porous architecture and robust bonding between PINF

and Mxene, the PINF/MXene hybrid aerogel exhibited an ultralow density (9.98 mg cm^{-3}), intriguing temperature tolerance from 50 to 250 °C, superior compressibility and recoverability (up to 90% strain), and excellent fatigue resistance over 1000 cycles. The hybrid aerogel could be used as a pressure sensor, with an outstanding sensing capacity up to 90% strain (corresponding 85.21 kPa), ultralow detection limit of 0.5% strain (corresponding 0.01 kPa), robust fatigue resistance over 1000 cycles, excellent pressure stability, and reproductivity in extremely harsh environments (Fig. 15e and f). Similarly, Yang *et al.*[119] reported an MXene/ANF fibrous aerogel with high compressible resilience and appealing sensing performance up to 1000 cycles. The MXene/ANF fibrous aerogel based sensor demonstrated a wide detection range (2.0–80.0% compression strain), sensitive sensing properties (128 kPa^{-1}), and ultralow detection limit (100 Pa), which still played a flexible role in detecting human light movement and even vigorous sports after undergoing ultrahigh devastating pressures (~623 kPa). Besides, Yao *et al.*[120] reported the preparation of self-reporting Ag nanoparticles (AgNPs)/cellulose nanofiber aerogels as stress sensors. To test the electrical conductivity of 3D fibrous aerogels and exam the relationship between normalized electrical resistance (R_t/R_0) and compressive strain, the aerogels were connected with a lamp in a simple circuit (Fig. 15g). The R_t/R_0 dramatically decreased by 65% with an increase of strain to 20%. This result was ascribed to the fact that the compression could create numerous new temporary contacts among cellulose nanofibers and AgNPs paths in the whole aerogel, thereby reducing the electrical resistance. It was illumined with a light-emitting diode in a 3 V circuit, and its brightness fluctuated as the aerogel was compressed (Fig. 15h). Qin *et al.*[121] prepared a brand-new and high-performance flexible pressure sensor based on Ppy/CA fibrous hybrid aerogels. The prepared flexible pressure sensor could exhibit an ultra-high sensitivity (60.28 kPa^{-1}) and wide pressure range (0–24 kPa), which was suitable for realizing the real-time monitoring and identification of human motions (Fig. 15i). It can provide a broad application prospect in the field of wearable electronic devices due to its simple preparation process and excellent piezoresistive performance.

3.4 Triboelectric nanogenerators

Energy harvesting technologies of electromechanical transformation, such as triboelectric nanogenerators (TENGs), piezoelectric nanogenerators (PENGs), and electromagnetic generators (EMGs), have gained more attention due to the rapidly increasing demand for clean and sustainable energy resources for new electronic devices (*e.g.*, smart wearable self-powered sensors, mobile communication electronics, *etc.*).[122–126] Among these emerging technologies, TENGs have proven to be viable candidates for lightweight energy harvesting devices, wearable sensors, and health monitoring devices due to their low cost, light weight, flexible structures, and ease of fabrication, since first reported in 2012.[124] As is well known,

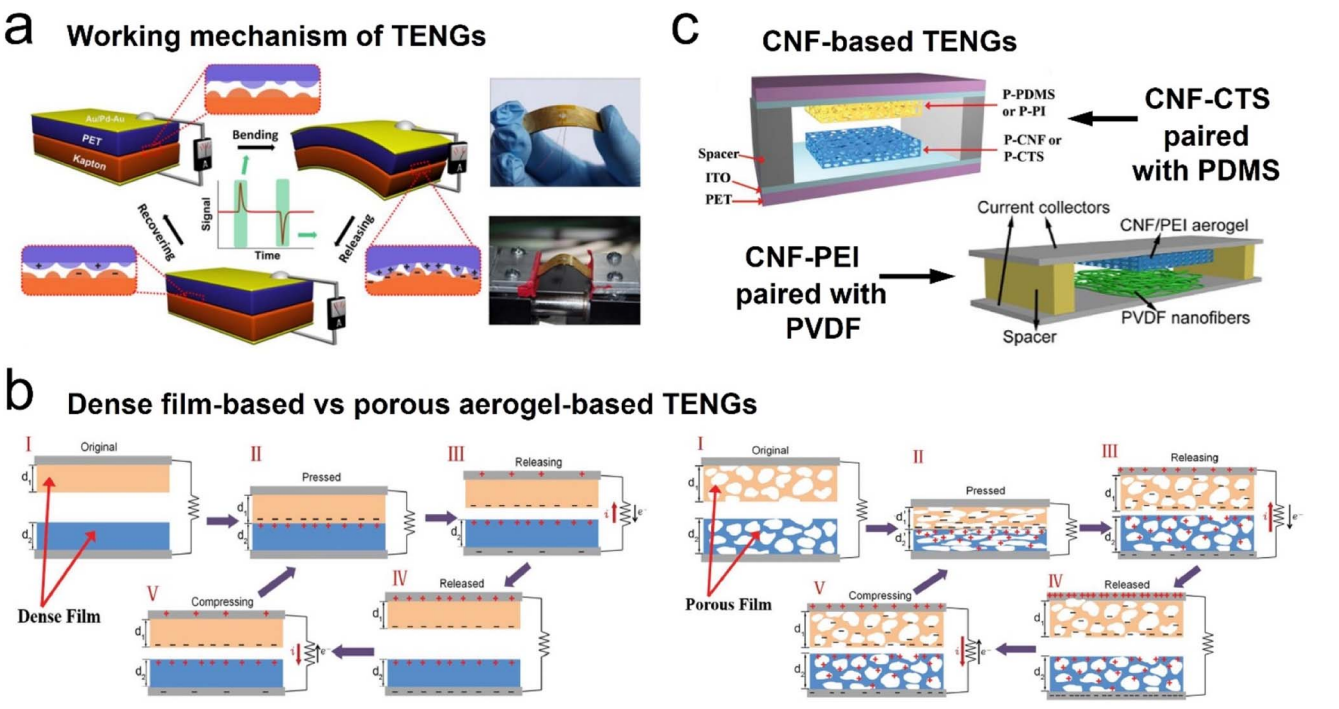

Fig. 16 Schematic illustration of the structure and working principle of the triboelectric generator. (a) Schematic illustration and working principle of TENGs. Reproduced with permission.[124] Copyright 2012, Elsevier. (b) Comparison of the surface charge density of dense film-based and porous aerogel-based TENGs. Reproduced with permission.[127] Copyright 2018, Wiley-VCH. (c) A schematic illustration of cellulose nanofibril-based TENGs: cellulose nanofibril–chitosan hybrid aerogels paired with PDMS or PI. Reproduced with permission.[127] Copyright 2018, Wiley-VCH. A schematic illustration of a cellulose nanofibril–polyethyleneimine (PEI) hybrid aerogel paired with PVDF. Reproduced with permission.[128] Copyright 2018, Elsevier.

several working modes for TENGs have been widely developed based on the same fundamental principle: vertical contact-separation mode, lateral-sliding mode, single-electrode mode, and freestanding triboelectric-layer mode.[125] Besides, with the aid of state-of-the-art material characterization techniques, the charge transfer mechanisms for TENGs could be categorized into three possible models, which are responsible for triboelectricity: electron transfer model, ion transfer model, and material transfer model. For 3D fibrous aerogel-based TENGs, the working mechanism and ion transfer model of the charge transfer mechanism are shown in Fig. 16. The physical fundamentals of TENGs are the triboelectric effect and the electrostatic induction between two layers of thin films that have dissimilar tribopolarities. The friction between the triboelectric surface films produces polarized charges, which result in inductive charges among electrodes (Fig. 16a). These inductive charges drive through the electrodes and consequently convert the mechanical energy to electricity. The triboelectric charge density created on the contact surfaces is the most important factor for the performance of the TENGs. Due to this reason, a variety of materials ranging from polymers to metals have been used in the fabrication of high-performance TENGs. Moreover, several physical and chemical techniques are developed to modify the contact surface morphology of TENGs, such as creating micro/nanopatterns on contact surfaces, molecular surface functionalization, doping nanomaterials into the contact surfaces, adding sublayers into the bulk friction materials, and using porous structures such as aerogels instead of films. Among all these, aerogels have received increased attention due to their porous structures. Fig. 16b shows how to use porous fibrous structures to increase the charge density on triboelectric surfaces compared to films. In the case of porous fibrous aerogel film-based triboelectric nanogenerators (*i.e.*, cellulose nanofibrils and polydimethylsiloxane (PDMS) in the present case), charges are not only induced on the contact surface upon contact, and additional charges on the porous surface of cellulose nanofibrils and PDMS will also be generated owing to the compression of pores with the associated electrostatic effects, resulting in a larger electrical potential difference between the top and bottom electrodes upon release, thereby leading to a much higher electrical output. Furthermore, the fibrous structure of 3D fibrous aerogels exhibited a higher deformation compared to the dense films under the same compressive stress, which will increase the relative capacitance, thus increasing the triboelectric output.[122,123] Therefore, 3D fibrous aerogels are considered the best porous materials for the generation of high output voltages and performances in the TENGs due to their flexibility, high surface area, and surface functional groups.

Typically, Zheng *et al.*[127] first introduced a novel approach, employing aerogels in both positive and negative triboelectric surfaces in the fabrication of TENGs to improve the power outputs. Highly porous cellulose nanofibril, chitosan (CTS), and cellulose nanofibril–aminosilane aerogels have been used as triboelectric positive materials paired with PDMS or highly porous (92% porosity) PI as the triboelectric negative material, as shown in Fig. 16c. Their work reveals that the porous structure of aerogels increases the electrostatic induction, and subsequently, the performance of TENGs. The cellulose nanofibril–PDMS and cellulose nanofibril–PI TENGs exhibited output voltages and currents of 22.3 V and 2.2 μA, and 39.3 V and 4.3 μA, respectively, which results in about 8 times and 14 times power enhancement, respectively. Their study showed that the output voltage and current increase with increasing porosity due to the increase in the contact area and the electrostatic induction in the aerogel pores.

Mi *et al.*[128] have built on the earlier work by developing an intriguing concept in their use of a cellulose nanofibril hybrid aerogel for TENG applications. The prepared cellulose nanofibril/PEI aerogels were the positive triboelectric material paired with electrospun PVDF nanofibers as the negative triboelectric material, and the operating principle of the cellulose nanofibril/PEI aerogel–PVDF nanofiber TENG was depicted as follows. Cellulose nanofibrils were reacted with branched PEI to introduce amino groups, which were strong electron donating groups. Unlike TENGs assembled with cellulose nanofibril aerogels, crosslinking cellulose nanofibrils using PEI results in 4.5 times improvement in the output voltage (Fig. 17a and b) and long-term stability (Fig. 17c). Similarly, Mi *et al.*[129] developed highly porous silk aerogel based TENGs (STENGs) with high output performance. The silk fibroin solution concentration had a significant influence on the aerogel morphology. The STENGs developed had a small unit size and high flexibility, which made it adaptable to different substrates and capable to be integrated into a wearable device. The STENGs made of silk aerogels had significantly high and stable voltage output (Fig. 17d–f). Moreover, silk fibroin can be used as an additive material to enhance the triboelectric output of the cellulose nanofibril aerogel based TENG due to its high tribopositivity. Besides, Mi *et al.*[130] developed another class of TENGs based on cellulose nanofibril–human hair (HH), and cellulose nanofibril–rabbit fur (RF) hybrid aerogels as the positive triboelectric material paired with a PI aerogel as the negative triboelectric material. The TENGs assembled using the cellulose nanofibril–RF hybrid aerogel exhibited the highest output voltage, current, and power density of 110 V, 11.3 μA, and 3.4 W m^{-2}, respectively, compared to cellulose nanofibril–silica fiber (SF) and cellulose nanofibril–HH at a comparatively low external pressure of 30 kPa due to the high specific surface area.

TENGs have been designed as power supply systems or self-powered sensors for applications in our surrounding areas at ambient temperature. However, their applications under harsh conditions, such as high-temperature environments in thermal power fields and aerospace, are still challenging. The positive tribo-materials of TENGs mainly include metals, carbon, and polymers, some of which may meet the requirements of fire resistance and thermal stability. By comparison, the negative tribo-materials of TENGs are mainly composed of polymeric materials, which become challenges for application under extreme conditions. For example, polytetrafluoroethylene (PTFE), as the most widely used negative tribo-material, will degrade into highly toxic substances above 400 °C or under the exposure to fire.[131] The operating temperature of PDMS, another commonly used negative tribo-material, is less than 200 °C.

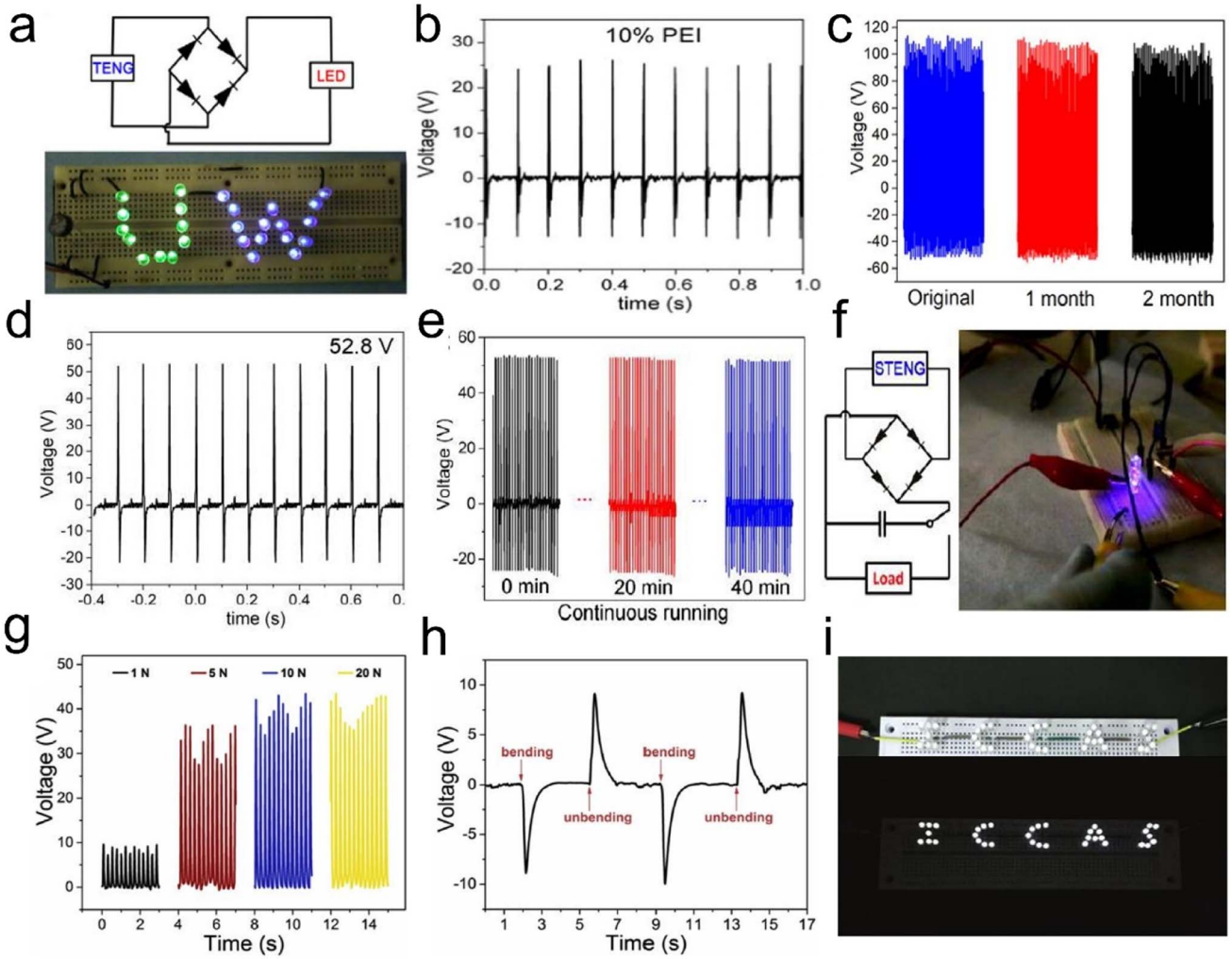

Fig. 17 Linear superposition tests and storage of electrical energy generated by 3D fibrous aerogel based TENGs and its application for driving a commercial LED. (a) Twenty-six green and blue LEDs were instantly turned on by a mini TENG. (b) Open circuit voltage of a cellulose nanofibril aerogel and cellulose nanofibril/PEI aerogel with 10% PEI. (c) Output performance stability test for the TENG over two months. Reproduced with permission.[128] Copyright 2018, Elsevier. (d) Triboelectric output voltage for silk aerogels prepared using silk fibroin solutions with a concentration of 2%. (e) Output voltage of STENGs in continuous running for 40 min. (f) Lighting of two LEDs using a 10 μF capacitor charged by a STENG. Reproduced with permission.[129] Copyright 2018, American Chemistry of Society. (g) PBOA/PEO TENGs were connected with a resistor (1 GΩ), and the pulse voltage on the resistor generated by the bending and unbending of fingers was recorded. (h) The open-circuit voltage and the short-circuit current density of PBOA/PEO TENGs. (i) Photographs of LED bulbs are lit by PBOA/PEO TENGs. Reproduced with permission.[133] Copyright 2019, Elsevier.

Hence, it is important to develop negative tribo-materials with high-temperature stability and flame resistance for applications of TENGs under extreme conditions. Poly(*p*-phenylene benzobisoxazole) (PBO) fibers have excellent thermal and mechanical performance, fire resistance, and a limiting oxygen index as high as 68, which is over twice that of aramids.[132] Qian *et al.*[133] first reported PBO aerogels (PBOAs) as the negative tribo-materials in TENGs. The resultant TENGs showed a maximum open circuit voltage, short-circuit current density, and charge density of 40 V, 2.9 mA m^{-2} and 72 μC m^{-2} (Fig. 17g and h), respectively. The device could light 36 LED bulbs and charge the capacitor to 10 V within 250 s (Fig. 17i). The device can also be used as a self-powered, highly sensitive sensor for monitoring human motion and even slight collisions with an impulse of only 3 μN s.

3.5 Supercapacitors

Supercapacitors are attracting considerable research interest as electrochemical energy storage devices.[134] The capacitance of supercapacitors mainly comes from the surface charge separation at the electrode/electrolyte interface (*e.g.*, electrochemical double layered capacitive behavior) and surface faradaic redox reactions (*e.g.*, pseudocapacitive behavior).[135,136] Carbon/graphite materials have excellent electrochemical double-layered capacitive behavior, while transition metal oxides, conductive polymers, and carbon materials doped with heteroatoms exhibit pseudocapacitive behavior.[137–139] Recently,

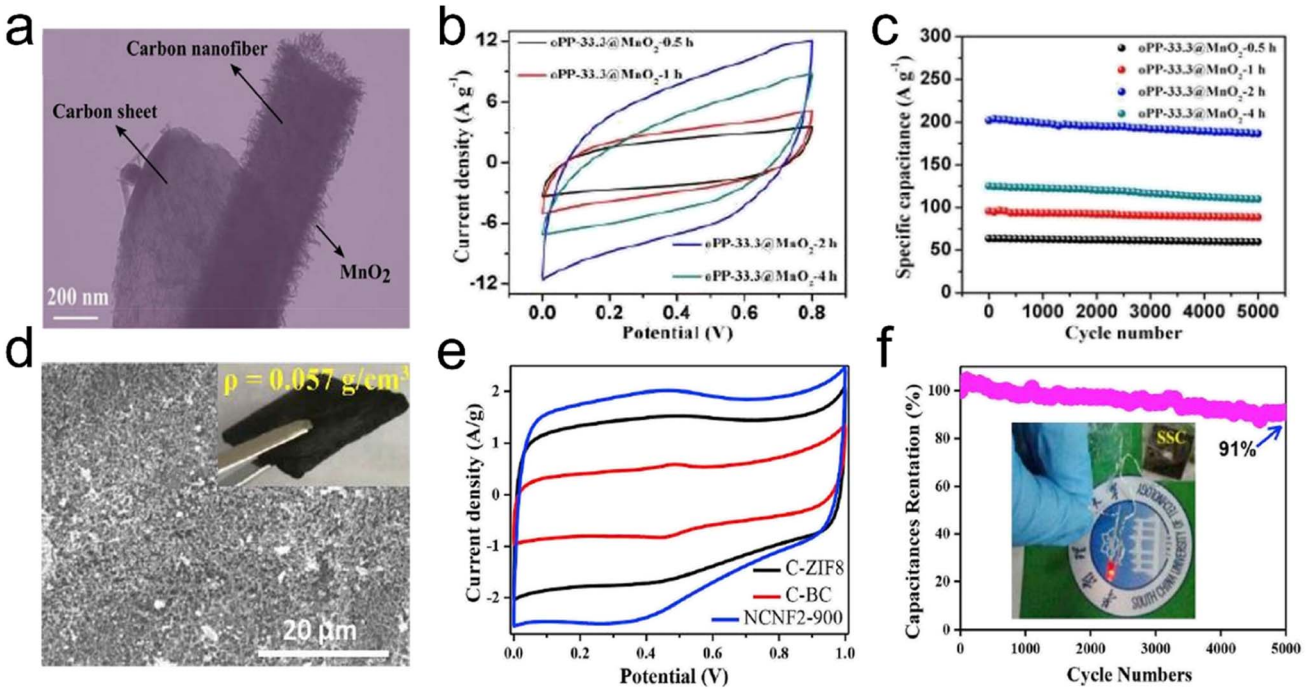

Fig. 18 3D fibrous aerogels as electrode materials for supercapacitors. (a) TEM image of an oPP-33.3@MnO_2-2h hybrid carbon aerogel. (b) *CV* curves for oPP-33.3@MnO_2-*x*h hybrid carbon aerogels at a scan rate of 50 mV s^{-1} (where $x = 0.5$, 1, 2, and 4, respectively). (c) Cycling stability of oPP-33.3@MnO_2-*x*h hybrid carbon aerogels at a scan rate of 50 mV s^{-1}. Reproduced with permission.[142] Copyright 2017, Royal Society of Chemistry. (d) SEM image of NCNFAs. (e) *CV* curves at 10 mV s^{-1} of the NCNFA electrode. (f) The symmetrical supercapacitor device measured at 2.5 A g^{-1} for 5000 cycles, and the inset graph shows a LED powered by the two in series. Reproduced with permission.[144] Copyright 2019, Elsevier.

carbon-containing CNT and graphene aerogels have been considered the most promising electrode materials for supercapacitors because of their combined advantages of a large internal surface area, small pore size, light weight, good electrical conductivity, and high mechanical as well as chemical stability.[140,141] The 3D interconnected architecture of aerogels can shorten the transport distances for ions and provide a consecutive pathway, therefore allowing for fast electron transport. Lai *et al.*[142] reported a novel carbon aerogel with a cellular structure, consisting of 1D oxidized polyacrylonitrile (o-PAN) derived carbon nanofibers and 2D PI originated carbon sheets. The interconnected o-PAN/PI (oPP) carbon aerogel possessed low density but enhanced mechanical strength, which could not only act as a versatile adsorbent but also as an ideal template for *in situ* growth of MnO_2 nanosheets to obtain oPP@MnO_2 hybrid carbon aerogels (Fig. 18a). The hybrid carbon aerogel had a rectangular *CV* curve with the largest proportions (Fig. 18b), reflecting excellent rate stability. Besides, the oPP-33.3@MnO_2-2h hybrid carbon aerogel showed a high retention of 92.4% after 5000 cycles (Fig. 18c), indicating excellent long cycling stability. The successful fabrication of oPP carbon aerogels has expanded the traditional electrospun lamellar membranes to 3D aerogels, providing a new strategy for developing nanofiber-based materials in energy storage toward energy storage and environmental protection applications. Xia *et al.*[143] reported a flexible electrode based on carbon fiber-reinforced cellulose nanofiber/multiwalled carbon nanotube-hybrid aerogels (CF-CNF/MWCNT-HAs). The 3D porous structure, excellent conductivity, binder-free nature, and high strength the CF-CNF/MWCNT-HAs enabled it to serve as a powerful platform for constructing flexible electrodes with good capacitive performance. The as-prepared CF-CNF/MWCNT/MnO_2 positive electrode and CF-CNF/MWCNT/active carbon (AC) negative electrode displayed remarkably high areal-specific capacitances (1745 and 1273 mF cm^{-2} at a current density of 1 mA cm^{-2}, respectively). Chen *et al.*[144] developed a low-cost, green, sustainable, and scalable approach to synthesize lightweight, highly porous, 3D interconnected N-self-doped carbon nanofiber aerogels (NCNFAs) with a silk cocoon-like node network by *in situ* growth of ZIF-8 nanocrystals on BC (PVA and acrylic acid (AA)). The *CV* curves for the NCNFAs had a roughly rectangular shape, including two apparent humps due to the pseudocapacitive effect (Fig. 18e). To show the practical application of the symmetrical supercapacitor, an LED was powered by two supercapacitors in series (inset in Fig. 18f). Furthermore, the all-sold-state symmetrical supercapacitor showed excellent capacitance retention, retaining 91% of the initial value after 5000 galvanostatic charge/discharge cycles.

Besides, to further enhance the performance of 3D structures as supercapacitor electrode materials suitable pores are made in carbon nanofibers by chemical/physical activation. The activation process is promisingly beneficial to form nanopores and mesopores in nanofibers, which are desired for supercapacitor applications. Specifically, nanopores would lead to

a high specific surface area, thereby benefitting the large capacitance, while mesopores would provide enhanced electrolyte penetration for high power density.[145] Another method is to develop 3D structures from transition metal oxide/sulfide nanofibers and conducting polymer nanofibers. Zhang *et al.*[146] developed a 3D highly conductive and elastic electrospun PAN/PVP based cellulose nanofiber aerogel (PVP as a solder to weld adjacent nanofibers) by freeze drying, carbonization, and CO_2 activation as a supercapacitor anode material. During the CO_2 activation at 900 °C, a fraction of carbon was burned off in the presence of CO_2 at the high temperature, resulting a high specific surface area of 437.2 $m^2\ g^{-1}$. The activated 3D anode material exhibited a high specific capacitance of 300 F g^{-1} at 0.3 A g^{-1}. Furthermore, the cellulose nanofiber surfaces were decorated with CNTs with the catalyst of metallic Co NPs, which were oxidized *in situ* to Co_3O_4 NPs. The hybrid aerogel as a hierarchical cathode showed a high specific capacitance of 2376 F g^{-1} at 1 A g^{-1}. By assembling the activated cellulose nanofiber aerogel as the anode and the hybrid aerogel as the cathode, the asymmetric supercapacitor exhibited a considerably high energy density of 48.1 W h kg^{-1} at 780.2 W kg^{-1}.

3.6 Electromagnetic interference shielding

Electromagnetic pollution has become a serious environmental issue due to the rapid development of various electronic devices and communication systems.[147] This problem of electromagnetic interference (EMI) not only threatens human health seriously but also affects the reliability and lifetime of sensitive electronic devices and systems. Therefore, it is desired to develop high-performance EMI shielding materials with lightweight and strong EM wave absorption ability.[147–149] Among

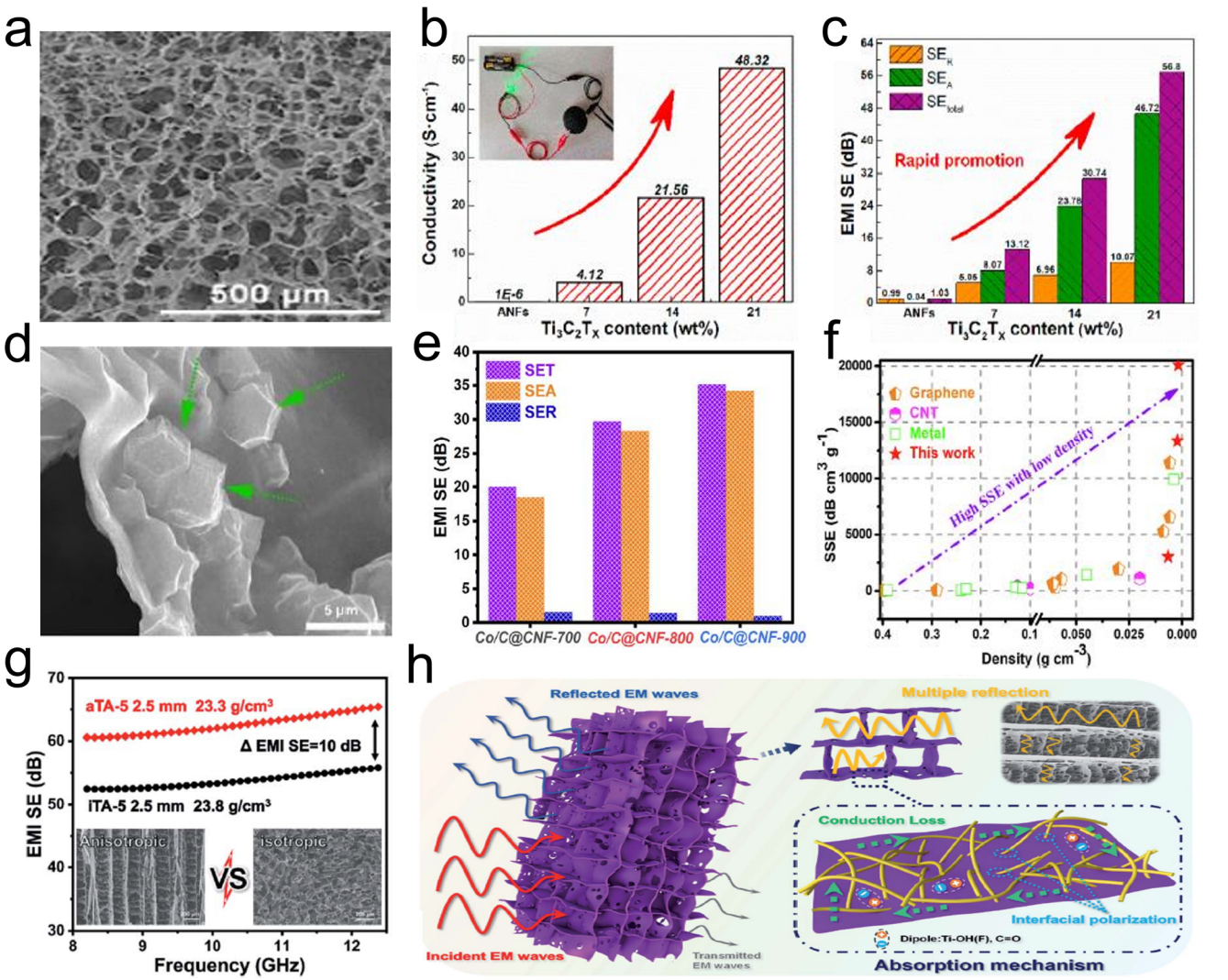

Fig. 19 3D fibrous hybrid aerogels for EMI. (a) SEM image, (b) histogram of electrical conductivity, and (c) comparison of microwave reflection (SER) and microwave absorption (SEA) of a $Ti_3C_2T_x$/ANF hybrid aerogel. Reproduced with permission.[58] Copyright 2017, Elsevier. (d) SEM image of the Co/C@/cellulose nanofiber aerogel. (e) Average SET, SEA, and SER values in the X-band of Co/C@cellulose nanofiber aerogels with various temperatures. (f) Comparison of the shielding performance of any aerogels/foams/sponges ever reported. Reproduced with permission.[76] Copyright 2020, Elsevier. (g) A comparison of the anisotropic and isotropic $Ti_3C_2T_x$/ANF aerogel. (h) EMI mechanism of the anisotropic $Ti_3C_2T_x$/ANF aerogel. Reproduced with permission.[150] Copyright 2022, Royal Society Chemistry.

EMI shielding materials, 3D fibrous aerogels with an interconnected network structure are known as a remarkable candidate to provide excellent EMI shielding, which not only provide a high specific surface and low density, but also have rich holes, which could enhance the dissipation of microwave energy in EMI shielding behavior.[150] Until now, various functional materials have been incorporated into 3D fibrous aerogel systems with low density and high porosity, including graphene, CNTs, MXene, and metal nanomaterials.[151,152] Lu *et al.*[153] developed a micro-porous structure MXene/ANF hybrid aerogel (Fig. 19a) through a freeze-drying approach. With increasing MXene ($Ti_3C_2T_x$) loading, $Ti_3C_2T_x$/ANF hybrid aerogels retained high electrical conductivity and efficient shielding capacity, whose EMI shielding effectiveness and specific EMI shielding effectiveness reached ~56.8 dB and 3645.7 dB cm^2 g^{-1} at a thickness of 1.9 mm in the X-band (Fig. 19b and c). Huang *et al.*[154] designed and prepared CTAB modified CNT/cellulose aerogels with a scaffold structure by controlling the concentration of cellulose in sodium hydroxide/urea solution, which exhibited a uniform outside surface and high porosity inside the structure. Furthermore, the aerogels showed an EMI shielding effectiveness of ~20.8 dB and a corresponding specific EMI shielding effectiveness as high as ~219 dB cm^3 g^{-1} with microwave absorption as the dominant EMI shielding mechanism in the microwave frequency range of 8.2–12.4 GHz at a density as low as 0.095 g cm^{-3}.

3D CNFAs prepared by high-temperature pyrolyzing biomass or polymer aerogels have attracted extensive academic interest and work efficiently as EMI shielding materials based on their excellent performance of ultralow density, prominent electrical conductivity, large specific surface area, and unique 3D carbon skeleton architecture. The abundant conjugate aromatic structure in the backbone endowed the ANF-derived carbon aerogel film with a high conductivity of 1029.5 S m^{-1}. Remarkably, the high electrical conductivity, as well as the 3D porous skin-core structure, which not only constructs the interconnected electron transmission paths but also significantly extends the propagation path of electromagnetic waves, endowed the carbon aerogel film with a high EMI shielding effectiveness (SE) of 41.4 dB at low density (54.4 mg cm^{-3}) and thin thickness (162 mm) with a high specific shielding effectiveness (SSE/t) of up to 47122.6 dB cm^2 g^{-1}. Fei *et al.*[149] reported a 3D ultralight Co/C@cellulose nanofiber aerogel consisting of interconnected carbon sheet networks embedded with Co/C nanoparticles (Fig. 19d), featuring superior electrical conductivity, low specific weight, and outstanding EMI shielding. The performance greatly depends on the carbonization temperature, which affects the graphitization degree and magnetic variation. The Co/C@cellulose nanofiber aerogel at a calcination temperature of 900 °C achieved the highest effectiveness of 35.1 dB at a density of only 1.74 mg cm^{-3}, with a good specific SE of 20172.4 dB cm^3 g^{-1} (Fig. 19e and f). Wan *et al.*[148] used pyrolyzed cellulose nanofiber aerogels as substrates to support some functional materials (*e.g.*, α-FeOOH, α-Fe_2O_3, and polypyrrole) for enhancing the EMI shielding performances of the carbonized composite aerogels. The composite carbon aerogels exhibited a highest SET of ~39.4 dB, which was several times higher than that of the individual component. An adsorption-dominant shielding mechanism was ascribed to a more effective complementarity between dielectric loss and magnetic loss from conductive and magnetic fillers well-distributed inside the carbonized porous conductive fibrous network of the aerogel, which was good for higher EM wave absorption and alleviating the secondary radiation. These carbonized CNFAs have become important parts for the construction of EMI shielding materials.

Besides, constructing an anisotropic fibrous aerogel is considered as a promising strategy for improving EMI shielding performances. Compared with the incomplete conductive network in a conventional isotropic aerogel, the anisotropic aerogel was endowed with a macroscopic ordered conductive network through the design of an anisotropic structure. The "cell wall" structure connecting the ordered structures not only optimized the integrity of the aerogel conductive network, but also increased the impedance mismatch interface and improved the multiple reflection efficiency of electromagnetic waves. Typically, Zhang *et al.*[150] prepared an ultralight, conductive $Ti_3C_2T_x$/ANF anisotropic aerogel by directional freezing and freeze-drying, which not only endowed it with excellent compressibility and superelasticity, but also built a macroscopic conductive network, thus increasing the impedance mismatch interface, and ensuring the EMI shielding performance of the device. At an ultra-low $Ti_3C_2T_x$ content (0.58 vol%), the conductivity of the $Ti_3C_2T_x$/ANF anisotropic aerogel reached a maximum of 854.9 S m^{-1} and the EMI SE reached 65.5 dB (Fig. 19g), which was the best efficiency value of an aerogel based on ANFs so far. Fig. 19h briefly shows the mechanism of the $Ti_3C_2T_x$/ANF anisotropic aerogel achieving high shielding performance. Based on directional freezing, ordered channels and array "cell wall" structures were formed in the aerogel, which introduced more impedance mismatch interfaces, thereby enhancing the multiple reflections of internal electromagnetic waves. Moreover, the integrated conductive network was formed with a long-range ordered anisotropic structure through the two-dimensional MXene sheet, resulting in a huge amount of electron migration, energy dissipation into heat, and conductive loss.

3.7 Adsorption of heavy metal ions and organic dyes

Worldwide water pollution and the scarcity of clean drinking water have led to a strong need for the development of energy-saving and cost-efficient water purification technologies.[155,156] Some heavy metals and organic dyes are a serious cause of concern due to their toxic effect on human beings, the aquatic life, and the ecosystem. Adsorption is an effective technique to remove these contaminants. 3D fibrous aerogels or aerogels are being explored as a novel adsorbent material for water treatment due to their attractive properties of a high specific surface area, large porosity, high adsorption capacity, and ease of recycling without secondary pollution. Typically, cellulose-based aerogels known as bio-aerogels are a group of organic aerogels with superior adsorption properties. Compared to traditional inorganic aerogels (*e.g.*, silica), bio-aerogels are reported to have high strength and do not break under

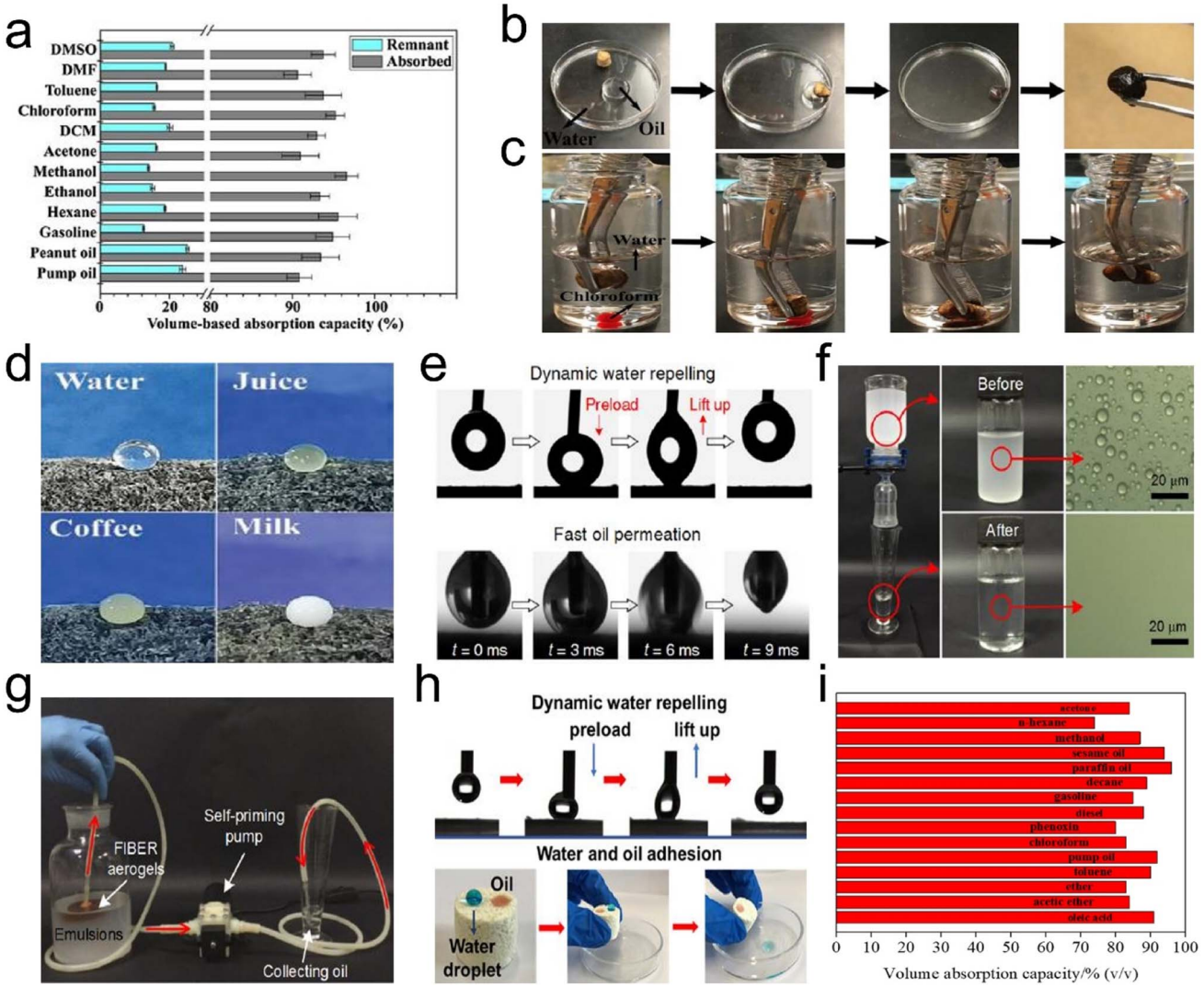

Fig. 20 Various functions of 3D fibrous aerogels for applications in water treatment. (a) Volume-based absorption capacities of a UECA on different organic compounds. (b) Removing pump oil from the surface of water. (c) Collecting chloroform (containing the dye of Sudan I) from the bottom of water. Reproduced with permission.[159] Copyright 2019, Elsevier. (d) Digital pictures showing the state of different liquid droplets on the surface of PINF/MXene hybrid aerogels. Reproduced with permission.[171] Copyright 2021, Wiley-VCH. (e) Photographs of dynamic measurements of water adhesion (top) and oil permeation (bottom) on the surface of the aerogels (2 wt% SiO_2 NPs). (f) Separation apparatus with the facile gravity-driven separation of water-in-oil emulsions using the aerogels and the microscopic images of emulsions before and after separation. (g) Photograph of the oil collection apparatus continuously collecting pure oil from water-in-oil emulsions. Reproduced with permission.[172] Copyright 2021, American Chemical Society. (h) Photographs of the dynamic measurements of water adhesion (top) and photograph of water and oil droplets on the aerogel surface (bottom). Reproduced with permission.[173] Copyright 2021, American Chemical Society. (i) Absorption efficiency of the carbon aerogels for various organic liquids. Reproduced with permission.[176] Copyright 2021, Elsevier.

compression with plastic deformation up to 80% strain before pore wall collapse.[157] Moreover, the production of aerogels from cellulose does not involve toxic compounds. She *et al.*[158] developed ecofriendly and recycled cellulose nanofiber aerogel adsorbents which were cross-linked by PVA and AA. The heavy metal ions were adsorbed on the cellulose nanofiber–PVA–AA adsorbents efficiently, and the maximum adsorption capacities for Cu^{2+} and Pb^{2+} approached 30.0 mg g^{-1} and 131.5 mg g^{-1}, respectively. Xu *et al.*[159] developed an ultralight electrospun cellulose aerogel (UECA) with high porosity (99.57%), low density (6.45 mg cm^{-3}), hydrophobic surface features (with a water contact angle of 141.2°), and excellent elasticity. The prepared UECA possessed super-high absorption capacity towards organic compounds (*e.g.*, oil and organic solvents) due to high porosity, low density, and desired surface hydrophobicity (Fig. 20a–c). Besides, due to the abundance of hydroxyl groups on native cellulose, they can be easily chemically modified to create improved versions of cellulose-based aerogels with enhanced adsorption ability, mechanical strength and the ability to re-generate for repeated use. Zhu *et al.*[160] prepared fibrous MOF hybrid aerogels through the sequential processes of ionic gelation, template synthesis of MOFs, and freeze-drying. When exposing to multivalent metal ions (*e.g.*, Zn^{2+}, Cu^{2+}, Co^{2+}, *etc.*), carboxylic cellulose nanofibers would interact

ionically with metal ions. These ionic interactions served as ionic cross-linkers and favored a "phase transition" from colloidal cellulose nanofibers to homogeneous fibrous MOF layers. Cellulose nanofibers seemed to be physically cross-linked by H-bonding and physical entanglement of cellulose nanofibers as well as strong interactions between MOF crystals and cellulose nanofibers. The resultant MOF aerogels (*e.g.*, HKUST-1, ZIF-8, ZIF-67, *etc.*) all demonstrated excellent adsorption performances towards organic dyes such as Rhodamine B, Methyl Violet, and Methylene Blue. Similarly, our group[161,162] reported that the *in situ* growth of nano-porous materials (*e.g.*, MnO_2, ZIF-67, *etc.*) on the ANF aerogel framework could improve the adsorption capacity of heavy metal ions (Pb^{2+}, Cu^{2+}, and Cr^{6+}) and organic dyes (methyl orange and crystal violet). He *et al.*[163] developed a PI amine dendrimer aerogel based on ANFs through an effective method, which showed a specific area larger than the ANF aerogel by 38.1% due to the formation of polyamide amine dendrimer nanofibers bridging between ANFs. Besides, electrospun polymer nanofiber-based aerogels are considered a promising absorbent due to their fantastic porosity characteristics. Xue *et al.*[164] reported novel fibrous aerogels prepared by freeze-drying technology and cross-linking with epichlorohydrin (ECH) *via* short PAN/PEI nanofibers, showing high mechanical stability and good mass transfer performance. The adsorption capacities of these prepared fibrous aerogels reached 242.71 mg g^{-1} (Cu^{2+}), 214.14 mg g^{-1} (Cr^{6+}), 258.36 mg g^{-1} (As^{5+}), and 183.06 mg g^{-1} (anionic dye methyl orange). The adsorbent still kept considerable adsorption efficiency after seven adsorption–regeneration cycles.

3.8 Oil–water separation

Oil spill from different sources, for example, from tankers or oil drilling, is regarded as one of the most severe water pollution problems. Efficient ways of separation of oil from water are therefore required to protect the marine environment and are a large challenge. Conventional methods such as oil skimmers, centrifuges, depth filters, sedimentation, and flotation are useful for the separation of immiscible oil/water mixtures, but are not effective for emulsified oil/water mixtures.[165,166] Membrane-based technologies, such as ultrafiltration which selectively allows materials of certain sizes to pass through the membrane pores on the basis of the size-sieving effect, have been successfully used to separate various industrial emulsions. However, these pressure-driven separation membranes suffer from low flux and energy consumption due to a small pore size (<0.3 μm).[167,168] Alternatively, interfacial super-wetting 3D fibrous aerogels with high porosity and tunable pore structures are generally regarded as effective media to selectively remove oil and water.[169] The developed interfacial super-wetting 3D fibrous aerogels are mainly divided into two different types due to their surface wettability and functions in handling different oil/water mixtures: (i) superhydrophobic–superoleophilic aerogels are used to absorb oil; (ii) superhydrophilic–underwater superoleophobic aerogels are used to eliminate the layered oil/water mixture and oil-in-water emulsions.[170]

The general methods to develop interfacial super-wetting 3D fibrous aerogels mainly include creating hierarchical structures (nano/microstructure) and surface chemistry modification. Typically, the secondary surface morphology (*e.g.*, wrinkled structure, nano/microstructure, branched structure, *etc.*) on the nanoscale is usually considered as one of the most important factors to the surface properties, which can endow 3D fibrous aerogels with excellent oil–water separation performances. For example, Liu *et al.*[171] prepared PINF/MXene hybrid aerogels with a typical "layerstrut" bracing hierarchical fibrous cellular structure. The surface of the hybrid aerogels immersed in water displayed strong light reflection, which was caused by the trapped air layer that led to total light reflection, preventing it from being wetted effectively. And the various liquid droplets, including water, juice, coffee, and milk, could retain a spherical shape on the surface of hybrid aerogels, demonstrating the hydrophobicity of the hybrid aerogels (Fig. 20d). The hybrid aerogels exhibited superior oil/water separation properties such as high adsorption capacity (55.85 to 135.29 g g^{-1}) and stable recyclability due to its hydrophobicity and robust hierarchical porous structure. Si *et al.*[172] developed superelastic and superhydrophobic PAN/SiO_2 fibrous aerogels with a hierarchical cellular structure. By the inclusion of hydrophobic SiO_2 NPs, the morphologies of the resultant fibrous aerogels were changed by creating nanoscaled rough structures on the surface of nanofibers. With increasing SiO_2 NP concentrations, the average pore size of aerogels quickly decreased from 18.9 to 4.2 μm; meanwhile, the specific surface area of fibrous aerogels increased dramatically from 2.66 to 76.54 m^2 g^{-1}. The PAN/SiO_2 fibrous aerogels exhibited superhydrophobic–superoleophilic wettability, which could separate surfactant-stabilized water-in-oil emulsions, solely using gravity, with a high flux that was several times higher than that of commercial filtration membranes driven by external pressure (Fig. 20e–g). Besides, Shen *et al.*[173] reported novel hybrid PI fibrous aerogels by reconstructing intrinsically lamellar-deposited electrospun nanofibers. The porous fibrous aerogels were further modified using trichloromethylsilane (TCMS) to generate silicone nanofilaments (SiNFs) on the surface of the PI nanofibers, which could enhance the hydrophobicity (water contact angle 151.7°) of the fibrous aerogels. SiNF-coated fibrous aerogels could collect a wide range of oily solvents with high absorption capacities up to 159 times their own weight (Fig. 20h). Similarly, Tai *et al.*[174] reported self-assembled superhydrophobic electrospun carbon–silica nanofiber aerogels, and the prepared aerogels exhibited superhydrophobicity with the average water contact angle being 155.4°. In contrast, a commercial polyurethane aerogel would sink below the water surface owing to its hydrophilicity. Finally, the prepared aerogels exhibited high sorption capacities of 65 to 140 times their own weight with larger sorption capacities for liquids of higher density (*e.g.*, benzyl alcohol) and cyclic distillation performance.

The surface chemistry modification of 3D fibrous aerogels can be tubed using low or high surface energy molecules with the aid of common techniques including dip-coating, solution immersion, chemical vapor deposition (CVD), carbonization, and so on.[170] For instance, Chhajed *et al.*[167] utilized stearic acid

chloride (SAC) as the dip-coating material to modify cellulose nanofiber aerogels, and the surface modification of cellulose nanofiber aerogels was carried out by esterification reaction dip coating. The SAC conjugated aerogels combined both superhydrophobic and oleophilic characteristics showed a contact angle of ~159° and ~0° with water and oil, respectively. The prepared aerogels were found to be very efficient in separating a series of oil/water mixtures and various organic solvents with excellent selectivity and recyclability. Qiao *et al.*[168] reported a superhydrophobic, elastic, and anisotropic cellulose nanofiber aerogel. Specifically, directional freeze-drying, soaking in polydimethylsiloxane (PDMS) solution, and heat treatment were applied to obtain anisotropic hybrid aerogel sheets and blocks with superhydrophobicity and high elasticity. The hybrid fibrous aerogels could realize continuous oil/water separation by filtration with a flux up to 2800 L m^{-2} h^{-1} and a separation efficiency of 99.9%. Deuber *et al.*[175] prepared pullulan/PVA fibrous aerogels modified using trichloro(octyl)silane (TOS) *via* a CVD method, which exhibited a hydrophobic surface and showed a high absorption capacity of 430 m^3 m^{-3}. Long *et al.*[176] developed a hydrophobic carbon aerogel derived from deep eutectic solvent (DES) modified cellulose nanofibers under a low carbonization temperature of 350 °C. The as-prepared carbon aerogel showed a high volume absorption capability

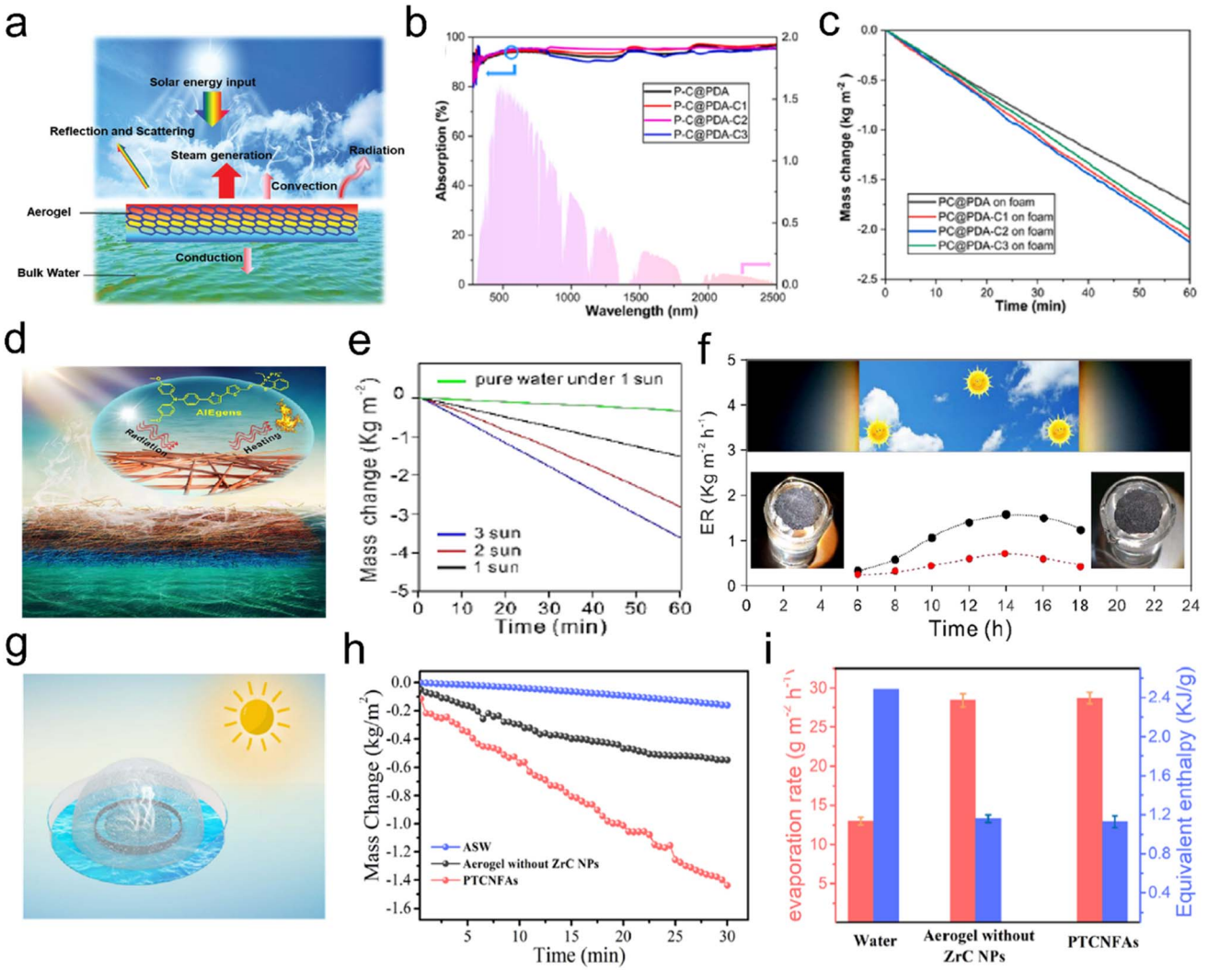

Fig. 21 3D fibrous aerogels applied in interfacial solar vapor generation. (a) Schematic illustration of tailoring aerogels for interfacial solar vapor generation. Reproduced with permission.[181] Copyright 2019, Wiley-VCH. (b) UV-vis-NIR absorption spectra of different fibrous aerogels and spectrum of AM 1.5 G. (c) Mass change of different aerogels standing on foam. Reproduced with permission.[183] Copyright 2022, Elsevier. (d) Schematic of solar steam generation. (e) The mass loss of water over time under different illumination intensities. (f) Evaporation rate of 3D fibrous aerogels (black spots) at 6:00 to 18:00 for over a day (red spots show the evaporation rate of a blank beaker without 3D fibrous aerogels). The inset shows the photograph images of the 3D fibrous aerogels at the beginning and end under irradiation of sunlight for one day, and no salt deposition was observed. Reproduced with permission.[184] Copyright 2020, American Chemical Society. (g) Schematic of the solar vapor generation device which is based on the PTCNFAs under 1 sun irradiation. (h) Mass change of evaporated vapor over time. (i) Water evaporation rate ratio under dark conditions and the calculated equivalent enthalpy. Reproduced with permission.[185] Copyright 2020, American Chemical Society.

for organic pollutants and oils ranging from 74% to 95% (Fig. 20i). Besides, Zhou *et al.*[177] reported an anisotropic lamellar hydrophobic and lipophilic graphene/PVA/cellulose nanofiber carbon aerogel prepared by directional freeze-drying and carbonization processes. The directional freeze-drying process led to a lamellar interpenetrated 3D porous structure, which endowed the carbon aerogel with high adsorption capacity (155–288 times of its weight), good compressibility (95% recovery after repeating 15 cycles at 50% strain in parallel to the freezing direction) and recyclability (oil retention rate reached 88.8% after 10 absorption–compression cycles).

3.9 Interfacial solar vapor generation

Interfacial solar vapor generation is intensely pursued as one of the most promising technologies to provide portable clean water solution for water-stressed areas.[178–180] With carefully tailored solar absorbers, the energy of solar irradiation can be absorbed and converted into heat, which can be utilized to vaporize water in the interfacial area of water and air.[181] Aerogels with highly porous structures had several intrinsic superiority ideal for interfacial solar vapor generation (Fig. 21a). First, the fibrous networks of the aerogels can reduce the light reflection and improve light scattering inside pores of aerogels, promoting the absorption of solar energy. Second, the highly porous features can confine the generated heat in the interfacial region of water and air and reduce conduction heat loss.[182] Third, the interconnected pores inside aerogels can offer plenty of channels for fast water transportation and vapor escape, which endow aerogels with lightweight properties and make aerogels naturally float on the water surface without any support.[182]

In the past few years, 3D fibrous aerogels have been widely developed for interfacial solar vapor generation, achieving improved energy conversion efficiency. Qin *et al.*[183] prepared luffa-inspired electrospun PAN/CNT nanofiber-based aerogels with a hierarchical pore structure using an eco-friendly cross-linking and easy freeze-drying approach. The fibrous aerogels combined the synergistic photothermal effect of polydopamine (PDA) and CNTs, leading to a high light absorption of 94.8% (Fig. 21b). Furthermore, the 3D interconnected structure formed from nanofibers greatly reduced the enthalpy of vaporization. The prepared fibrous aerogels showed a fast evaporation rate of 2.13 kg m^{-2} h^{-1} and a high solar-vapor conversion efficiency of 94.5% under one sun (Fig. 21c). Tang *et al.*[184] demonstrated 3D fibrous aerogels by doping an aggregation-induced emission (AIE) photothermal molecule, which could float on the water surface and continuously self-pump water (Fig. 21d). The prepared 3D fibrous aerogels had a high evaporation rate (1.43 kg m^{-2} h^{-1}), solar-to-vapor conversion efficiency (86.5%) under irradiation of 1 sun, and a high evaporation rate (10.9 kg m^{-2} h^{-1}) under natural sunlight (Fig. 21e). Besides, the outdoor experiment on the roof was carried out from 05:00 to 19:00 under natural sunlight. As depicted in Fig. 21f, the evaporation rate of the 3D fibrous aerogels at 06:00 was only 0.17 kg m^{-2} h^{-1}, which agrees well with the dark-condition data. The average seawater evaporation rate was calculated to be 1.09 kg m^{-2} h^{-1}, revealing an enhanced evaporation, compared with that under blank test conditions. Wang *et al.*[185] reported photothermal conversion fibrous aerogels (PTCNFAs) with vertically aligned microchannels as a solar steam generator (Fig. 21g). Benefiting from the excellent mechanical properties, high water-transfer rates, and outstanding photothermal properties, the PTCNFAs were more convenient in application and exhibit an efficient solar water evaporation rate (2.89 kg m^{-2} h^{-1}) (Fig. 21h), while the energy efficiency under 1 sun was about 90.3% (Fig. 21i). Our group[186] fabricated an all-in-one solar-driven interfacial evaporator from a hybrid fibrous aerogel of ANFs, CNTs, and AuNPs. The fibrous aerogels showed a high evaporation rate of 1.53 kg m^{-2} h^{-1} and an evaporation efficiency of 91.3% under 1 sun irradiation. Moreover, the evaporator demonstrates a high purification capacity for wastewater with dyes and heavy metal ions. These research studies all demonstrate that 3D fibrous aerogels may provide a novel structured photothermal conversion material for the solar steam generation application to meet the demands of environmentally friendly treatment of seawater or sewage.

4. Summary and future outlook

In the past few decades, a large number of 3D fibrous aerogels composed of versatile nanofibers have attracted widespread attention and have been extensively researched due to their promising future in a wide range of applications. Great achievements have been made in the research on 3D fibrous aerogels through continuous efforts. Up to now, many approaches have been proposed to fabricate different types of 3D fibrous aerogels with designed structures, mainly involving electrospinning, solution blow spinning, freeze-drying, thermally induced self-agglomeration, and carbonization. Based on the combined merits of ultra-low density, a high specific area, large porosity, mechanical stability, and controllable physical/chemical characteristics, the developed 3D fibrous aerogels have been widely applied in energy (*e.g.*, pressure sensors, triboelectric nanogenerators, supercapacitors, electromagnetic interference shielding, *etc.*) and the environment (*e.g.*, air filtration, thermal insulation, oil–water separation, interfacial solar vapor generation, *etc.*). Therefore, we review the advanced research and progress from the preparation methods to the multifunctional applications of 3D fibrous aerogels.

Despite the current huge advances, many momentous issues and challenges still remain and need to be further resolved by future enormous efforts. First, although the way of utilizing nanofibers as building blocks to construct 3D fibrous aerogels has improved the mechanical strength of monolithic materials to a certain extent, the mechanical strength and fatigue durability are still not strong enough to satisfy the requirements of highly effective practical applications, and therefore the mechanical properties of 3D fibrous aerogels should be ulteriorly strengthened. Second, the porous structure greatly affects the application performance of 3D fibrous aerogels due to its influences on the mass transfer and mechanical strength properties of 3D fibrous aerogels; however, precisely controlling

the porous structure of 3D fibrous aerogels is still a great challenge, which needs to be addressed imminently. Furthermore, most of the fabrication and application research studies of the current 3D fibrous aerogel materials are at the laboratory study level, and thus, large-scale and high-quality production of 3D fibrous aerogels with controlled structures is highly needed. 3D fibrous aerogels are expected to enter the market first in those areas in which they can provide significant performance improvements and create high value.

We anticipate that the summarized preparation methods and multifunctional application study of 3D fibrous aerogels, together with the well-selected references and some personal opinions, will furnish the relevant researchers with some guidance for the further study on the fabrication and application of high-performance 3D fibrous aerogels. Although a lot of challenges want to stop us, we believe that the overall goal of the preparation of multifarious 3D fibrous aerogels with precisely regulated porous structures, excellent mechanical properties, and highly effective performance will be achieved through our relentless searching and continual efforts, and the large-scale application of 3D fibrous aerogels will be achieved in the near future.

Conflicts of interest

The authors declare no conflict of interest.

Acknowledgements

We would like to thank the National Natural Science Foundation of China (51603148 and 51873152), Tianjin Science and Technology Project (20YDTPJC01380), and Tianjin Research Innovation Project for Postgraduate Students (2021YJSB224).

References

1 K. J. D. France, T. Hoare and E. D. Cranston, *Chem. Mater.*, 2017, **29**, 4609–4631.
2 V. Rahmanian, T. Pirzada, S. Y. Wang and S. A. Khan, *Adv. Mater.*, 2021, **33**, 2102892.
3 A. C. Pierre and G. M. Pajonk, *Chem. Rev.*, 2002, **102**, 4243–4266.
4 H. Sun, Z. Xu and C. Gao, *Adv. Mater.*, 2013, **25**, 2554–2560.
5 H. Tetik, Y. Wang, X. Sun, D. Cao, N. Shah, H. L. Zhu, F. Qian and D. Lin, *Adv. Funct. Mater.*, 2021, **31**, 2103410.
6 N. Hüsing and U. Schubert, *Angew. Chem., Int. Ed.*, 1998, **37**, 3071–3082.
7 J. Fricke and A. Emmerling, *Adv. Mater.*, 1991, **3**, 10–18.
8 S. S. Kistler, *J. Phys. Chem.*, 1932, **5**, 600–603.
9 H. D. Gesser and P. C. Goswami, *Chem. Rev.*, 1989, **89**, 765–788.
10 Y. T. Niu, F. Z. Li, W. X. Zhao and W. Cheng, *Nanoscale*, 2021, **13**, 7430.
11 W. Liu, A. K. Herrmann, N. C. Bigall, P. Rodriguez, D. Wen, M. Oezaslan, T. J. Schmidt, N. Gaponik and A. Eychmüller, *Acc. Chem. Res.*, 2015, **48**, 154.
12 Y. Tang, K. L. Yeo, Y. Chen, L. W. Yap, W. Xiong and W. Cheng, *J. Mater. Chem. A*, 2013, **1**, 6723–6726.
13 J. L. Mohanan, I. U. Arachchige and S. L. Brock, *Science*, 2005, **307**, 397–400.
14 C. Ziegler, A. Wolf, W. Liu, A. K. Herrmann, N. Gaponik and A. Eychmüller, *Angew. Chem., Int. Ed.*, 2017, **56**, 13200–13221.
15 F. Rechberger and M. Niederberger, *Nanoscale Horiz.*, 2017, **2**, 6–30.
16 M. B. Bryning, D. E. Milkie, M. F. Islam, L. A. Hough, J. M. Kikkawa and A. G. Yodh, *Adv. Mater.*, 2007, **19**, 661–664.
17 S. M. Jung, H. Y. Jung, M. S. Dresselhaus, Y. J. Jung and J. Kong, *Sci. Rep.*, 2012, **2**, 849.
18 S. M. Jung, H. Y. Jung, W. Fang, M. S. Dresselhaus and J. Kong, *Nano Lett.*, 2014, **14**, 1810–1817.
19 J. Z. Li, L. L. Wang, L. Li, C. C. Lv, I. V. Zatovsky and W. Han, *ACS Appl. Mater. Interfaces*, 2019, **11**, 8072–8080.
20 A. Menzel, K. Subannajui, F. Güder, D. Moser, O. Paul and M. Zacharias, *Adv. Funct. Mater.*, 2011, **21**, 4342–4348.
21 J. T. Schiphorst, M. V. D. Broek, T. D. Koning, J. N. Murphy, A. Schenning and A. C. C. Esteves, *J. Mater. Chem. A*, 2016, **4**, 8676–8681.
22 Y. Chen, L. Zhang, Y. Yang, B. Pang, W. Xu, G. Duan, S. Jiang and K. Zhang, *Adv. Mater.*, 2021, **33**, 2005569.
23 D. Li, T. Wu, N. He, J. Wang, W. Chen and L. He, *Colloids Surf., B*, 2014, **121**, 432–443.
24 N. Lavoine and L. Bergström, *J. Mater. Chem. A*, 2017, **5**, 16105–16117.
25 B. Dong, L. Gwee, D. S. Cruz, K. I. Winey and Y. A. Elabd, *Nano Lett.*, 2010, **10**, 3787.
26 Y. F. Li, Q. H. Li and Z. C. Tan, *J. Power Sources*, 2019, **443**, 227262.
27 A. Mohammed Al-Dhahebi, J. Ling and S. G. Krishnan, *Appl. Phys. Rev.*, 2022, **9**, 011319.
28 D. Li and Y. Xia, *Adv. Mater.*, 2004, **16**, 1151–1170.
29 S. Agarwal, J. H. Wendorff and A. Greiner, *Adv. Mater.*, 2009, **21**, 3343–3351.
30 L. Zhao, H. Y. Wu, W. L. Jiao, X. Yin, Y. Si, J. Y. Yu and B. Ding, *Compos. Commun.*, 2021, **25**, 100681.
31 H. Y. Wu, L. Zhao, Y. Si, S. C. Zhang, J. Y. Yu and B. Ding, *Compos. Commun.*, 2021, **25**, 100766.
32 R. Q. Liu, X. X. Wang, J. Fu, Q. Q. Zhang, W. Z. Song, Y. Xu, Y. Q. Chen, S. Ramakrishnal and Y. Z. Long, *Nanomaterials*, 2019, **9**, 1090.
33 Y. Gao, H. F. Xiang, X. X. Wang, K. Yan, Q. Liu, X. Li, R. Q. Liu, M. Yu and Y. Z. Long, *Chem. Eng. J.*, 2020, **387**, 124052.
34 B. Khalid, X. P. Bai, H. H. Wei, Y. Huang, H. Wu and Y. Cui, *Nano Lett.*, 2017, **17**, 1140–1148.
35 Y. Gao, J. Zhang, Y. Su, H. Wang, X. Wang, L. Huang, M. Yu, S. Ramakrishna and Y. Long, *Mater. Horiz.*, 2021, **8**, 426–446.
36 J. J. Xue, T. Wu, Y. Q. Dai and Y. N. Xia, *Chem. Rev.*, 2019, **119**, 5298–5415.
37 S. L. Chen, H. Q. Hou, F. Harnisch, S. A. Patil, A. A. Carmona-Martinez, S. Agarwal, Y. Y. Zhang, S. Sinha-

Ray, A. L. Yarin, A. Greiner and U. Schroder, *Energy Environ. Sci.*, 2011, **4**, 1417.
38 X. P. Zhuang, K. F. Jia, B. W. Cheng, X. Feng, S. J. Shi and B. Zhang, *Chem. Eng. J.*, 2014, **237**, 308–311.
39 S. C. Park, M. J. Kim, K. Choi, J. Kim and S. O. Choi, *RSC Adv.*, 2018, **8**, 32470–32480.
40 H. L. Wang, S. Lin, S. Yang, X. D. Yang, J. N. Song, D. Wang, H. Y. Wang, Z. L. Liu, B. Li, M. H. Fang, N. Wang and H. Wu, *Small*, 2018, **14**, 1800258.
41 G. D. Zhao, H. J. Zhao, X. P. Zhuang, L. Shi, B. W. Cheng, X. L. Xu and Y. Yin, *J. Mater. Chem. A*, 2021, **9**, 3729.
42 Z. W. Li, Z. W. Cui, L. H. Zhao, N. Hussain, Y. Z. Zhao, C. Yang, X. Y. Jiang, L. Li, J. N. Song, B. P. Zhang, Z. K. Cheng and H. Wu, *Sci. Adv.*, 2022, **8**, e3690.
43 Y. Huang, J. N. Song, C. Yang, Y. Z. Long and H. Wu, *Mater. Today*, 2019, **28**, 98–113.
44 Y. X. Hu, B. Luo, D. L. Ye, X. B. Zhu, M. Q. Lyu and L. Z. Wang, *Adv. Mater.*, 2017, **29**, 1606132.
45 C. Cheng, S. Li, A. Thomas, N. A. Kotov and R. Haag, *Chem. Rev.*, 2017, **117**, 1826–1914.
46 S. Deville, E. Saiz, R. K. Nalla and A. P. Tomsia, *Science*, 2006, **311**, 5156.
47 J. T. Schiphorst, M. V. D. Broek, T. D. Koning, J. N. Murphy, A. Schenning and A. C. C. Esteves, *J. Mater. Chem. A*, 2016, **4**, 8676–8681.
48 S. Deville, *Adv. Eng. Mater.*, 2008, **10**, 155–169.
49 V. Chabot, D. Higgins, A. Yu, X. Xiao, Z. Chen and J. Zhang, *Energy Environ. Sci.*, 2014, **7**, 1564–1596.
50 L. F. Chen, Y. Feng, H. W. Liang, Z. Y. Wu and S. H. Yu, *Adv. Energy Mater.*, 2017, **7**, 1700826.
51 S. Nardecchia, D. Carriazo, M. L. Ferrer, M. C. Gutierrez and F. Monte, *Chem. Soc. Rev.*, 2013, **42**, 794–830.
52 G. Nyström, M. P. Fernández-Ronco, S. Bolisetty, M. Mazzotti and R. Mezzenga, *Adv. Mater.*, 2016, **28**, 472–478.
53 S. M. Jung, D. J. Preston, H. Y. Jung, Z. Deng, E. N. Wang and J. Kong, *Adv. Mater.*, 2016, **28**, 1413–1419.
54 G. Wei and P. X. Ma, *Adv. Funct. Mater.*, 2008, **18**, 3566–3582.
55 J. Han, C. Zhou, Y. Wu, F. Liu and Q. Wu, *Biomacromolecules*, 2013, **14**, 1529–1540.
56 C. Liu, S. Wang, N. Wang, J. Y. Yu, Y. T. Liu and B. Ding, *Nano-Micro Lett.*, 2022, **14**, 194.
57 T. Xu, Y. C. Ding, Z. Wang, Y. Zhao, W. D. Wu, H. Fong and Z. T. Zhu, *J. Mater. Chem. C*, 2017, **5**, 10288–10294.
58 F. Deuber, S. Mousavi, M. Hofer and C. Adlhart, *ChemistrySelect*, 2016, **1**, 5595.
59 Q. X. Fu, Y. Si, C. Duan, Z. S. Yan, L. F. Liu, J. Y. Yu and B. Ding, *Adv. Funct. Mater.*, 2019, **13**, 1808234.
60 Y. Si, X. Q. Wang, C. C. Yan, L. Yang, J. Y. Yu and B. Ding, *Adv. Mater.*, 2016, **28**, 9512–9518.
61 H. F. Qin, Y. F. Zhang, J. G. Jiang, L. L. Wang, M. Y. Song, R. Bi, P. H. Zhu and F. Jiang, *Adv. Funct. Mater.*, 2021, **31**, 2106269.
62 F. Wang, L. Dou, J. W. Dai, Y. Y. Li, L. Q. Huang, Y. Si, J. Y. Yu and B. Ding, *Angew. Chem., Int. Ed.*, 2020, **132**, 8362.
63 L. Wang, M. Y. Zhang, B. Yang, J. J. Tan and X. Y. Ding, *ACS Nano*, 2020, **14**, 10633–10647.
64 G. Zu, J. Shen, L. Zou, W. Wang, Y. Lian, Z. Zhang and A. Du, *Chem. Mater.*, 2013, **25**, 4757–4764.
65 T. Xu, J. M. Miszuk, Y. Zhao, H. L. Sun and H. Fong, *Adv. Healthcare Mater.*, 2015, **4**, 2237.
66 T. Xu, Z. P. Liang, B. Ding, Q. Feng and H. Fong, *Polymer*, 2018, **151**, 299–306.
67 Q. Q. Yao, J. G. L. Cosme, T. Xu, J. M. Miszuk, P. H. S. Picciani, H. Fong and H. L. Sun, *Biomaterials*, 2017, **115**, 115–127.
68 J. M. Miszuk, T. Xu, Q. Q. Yao, F. Fang, J. D. Childs, Z. K. Hong, J. N. Tao, H. Fong and H. L. Sun, *Appl. Mater. Today*, 2018, **10**, 194–202.
69 X. Zheng, H. Lee, T. H. Weisgraber, M. Shusteff, J. DeOtte, E. B. Duoss, J. D. Kuntz, M. M. Biener, Q. Ge and J. A. Jackson, *Science*, 2014, **344**, 1373–1377.
70 D. Wang, H. Y. Peng, B. Yu, K. Q. Zhou, H. F. Pan, L. P. Zhang, M. Li, M. M. Liu, A. L. Tian and S. H. Fu, *Chem. Eng. J.*, 2020, **389**, 124449.
71 M. Zhang, D. Z. Yang, S. Y. Zhang, T. Xu, Y. Z. Shi, Y. X. Liu, W. Chang and Z. Z. Yu, *Carbon*, 2020, **158**, 873–884.
72 M. A. Khalily, H. Eren, S. Akbayrak, H. H. Susapto, N. Biyikli, S. Ozkar and M. O. Guler, *Angew. Chem., Int. Ed.*, 2016, **128**, 12445–12449.
73 Y. Si, J. Yu, X. Tang, J. Ge and B. Ding, *Nat. Commun.*, 2014, **5**, 5802.
74 G. Duan, S. Jiang, V. Jerome, J. H. Wendorff, A. Fathi, J. Uhm, V. Altstadt, M. Herling, J. Breu and R. Freitag, *Adv. Funct. Mater.*, 2015, **25**, 2850–2856.
75 H. L. Gao, L. Xu, F. Long, Z. Pan, Y. X. Du, Y. Lu, J. Ge and S. H. Yu, *Angew. Chem., Int. Ed.*, 2014, **126**, 4649–4654.
76 M. Zhang, D. Z. Yang, S. Y. Zhang, T. Xu, Y. Z. Shi, Y. X. Liu, W. Chang and Z. Z. Yu, *Carbon*, 2020, **158**, 873–884.
77 C. Li, Y. W. Ding, B. C. Hu, Z. Y. Wu, H. L. Gao, H. W. Liang, J. F. Chen and S. H. Yu, *Adv. Mater.*, 2020, **32**, 1904331.
78 M. Iguchi, S. Yamanaka and A. Budhiono, *J. Mater. Sci.*, 2000, **35**, 261–270.
79 H. Chen, T. Liu, J. R. Mou, W. J. Zhang, Z. J. Jiang, J. Liu, J. L. Huang and M. L. Liu, *Nano Energy*, 2019, **63**, 103836.
80 H. Y. Liu, T. Xu, C. Y. Cai, K. Liu, W. Liu, M. Zhang, H. S. Du, C. L. Si and K. Zhang, *Adv. Funct. Mater.*, 2022, 2113082.
81 L. Qiu, J. Z. Liu, S. L. Y. Chang, Y. Wu and D. Li, *Nat. Commun.*, 2012, **3**, 1241.
82 K. H. Kim, Y. Oh and M. F. Islam, *Nat. Nanotechnol.*, 2012, **7**, 562–566.
83 R. J. White, N. Brun, V. L. Budarin, J. H. Clark and M. M. Titirici, *ChemSusChem*, 2014, **7**, 670.
84 D. E. Gordon, G. M. Jang, M. Bouhaddou, J. Xu, K. Obernier, K. M. White, M. J. O'Meara, V. V. Rezelj, J. Z. Guo, D. L. Swaney, T. A. Tummino, R. Huttenhain, R. M. Kaake, A. L. Richards and B. Tutuncuoglu, *Nature*, 2020, **583**, 459–468.
85 P. Li, J. Li, X. Feng, J. Li, Y. Hao, J. Zhang, H. Wang, A. Yin, J. Zhou, X. Ma and B. Wang, *Nat. Commun.*, 2019, **10**, 2177.

86 T. Lu, J. X. Cui, Q. L. Qu, Y. L. Wang, J. Zhang, R. H. Xiong, W. J. Ma and C. B. Huang, *ACS Appl. Mater. Interfaces*, 2021, **13**, 23293–23313.
87 C. Liu, P. C. Hsu, H. W. Lee, M. Ye, G. Zheng, N. Liu, W. Li and Y. Cui, *Nat. Commun.*, 2015, **6**, 6205.
88 Z. N. Hu, S. Q. Yan, X. F. Li, R. C. You, Q. Zhang and D. L. Kaplan, *ACS Nano*, 2021, **15**, 8171–8183.
89 Z. C. Qian, Z. Wang, Y. Chen, S. R. Tong, M. F. Ge, N. Zhao and J. Xu, *J. Mater. Chem. A*, 2018, **6**, 828–832.
90 F. Deuber, S. Mousavi, L. Federer, M. Hofer and C. Adlhart, *ACS Appl. Mater. Interfaces*, 2018, **10**, 9069–9076.
91 Y. Y. Li, L. T. Cao, X. Yin, Y. Si, J. Y. Yu and B. Ding, *Adv. Funct. Mater.*, 2020, **30**, 1910426.
92 F. Wang, Y. Si, J. Y. Yu and B. Ding, *Adv. Funct. Mater.*, 2021, **31**, 2107223.
93 Y. G. Zhang, Y. J. Zhu, Z. C. Xiong, J. Wu and F. Chen, *ACS Appl. Mater. Interfaces*, 2018, **10**, 13019–13027.
94 Z. W. Liu, J. Lyu, D. Fang and X. T. Zhang, *ACS Nano*, 2019, **13**, 5703–5711.
95 B. Wicklein, A. Kocjan, G. Salazar-Alvarez, F. Carosio, G. Camino, M. Antonietti and L. Bergström, *Nat. Nanotechnol.*, 2015, **10**, 277.
96 Y. Si, X. Wang, L. Dou, J. Yu and B. Ding, *Sci. Adv.*, 2018, **4**, eaas8925.
97 T. Pirzada, Z. Ashrafi, W. Y. Xie and S. A. Khan, *Adv. Funct. Mater.*, 2019, **33**, 1907359.
98 M. Dilamian, M. Joghataei, Z. Ashrafib, C. Bohr, S. Mathur and H. Maleki, *Appl. Mater. Today*, 2021, **22**, 100964.
99 C. J. Xie, L. Y. He, Y. F. Shi, Z. X. Guo, T. Qiu and X. L. Tuo, *ACS Nano*, 2019, **13**, 7811–7824.
100 S. H. Jiang, B. Uch, S. Agarwal and A. Greiner, *ACS Appl. Mater. Interfaces*, 2017, **9**, 32308–32315.
101 S. Y. Zhou, V. A. Kalkavoura, M. V. T. Costa, L. Bergström, M. Strømme and C. Xu, *Nano-Micro Lett.*, 2020, **12**, 9.
102 M. A. B. Meador, E. F. Fabrizio, F. Ilhan, A. Dass, G. H. Zhang, P. Vassilaras, J. C. Johnston and N. Leventis, *Chem. Mater.*, 2005, **17**, 1085–1098.
103 S. Zhao, Z. Zhang, G. Sebe, R. Wu, R. V. R. Virtudazo, P. Tingaut and M. M. Koebel, *Adv. Funct. Mater.*, 2015, **25**, 2326–2334.
104 C. Ziegler, S. Klosz, L. Borchardt, M. Oschatz, S. Kaskel, M. Friedrich, R. Kriegel, T. Keilhauer, M. Armbruester and A. Eychmueller, *Adv. Funct. Mater.*, 2016, **26**, 1014–1020.
105 J. Laskowski, B. Milow and L. Ratke, *J. Non-Cryst. Solids*, 2016, **441**, 42–48.
106 L. Su, M. Z. Li, H. J. Wang, M. Niu, D. Lu and Z. X. Cai, *ACS Appl. Mater. Interfaces*, 2019, **11**, 15795–15803.
107 B. Wicklein, A. Kocjan, G. Salazar-Alvarez, F. Carosio, G. Camino, M. Antonietti and L. Bergström, *Nat. Nanotechnol.*, 2015, **10**, 277–283.
108 L. Su, H. Wang, M. Niu, M. Ma, X. Fan, Z. Shi and S. Guo, *ACS Nano*, 2018, **12**, 3103–3111.
109 Y. Si, X. Wang, L. Dou, J. Yu and B. Ding, *Sci. Adv.*, 2018, **4**, eaas8925.
110 L. Dou, X. X. Zhang, X. T. Cheng, Z. M. Ma, X. Q. Wang, Y. Si, J. Y. Yu and B. Ding, *ACS Appl. Mater. Interfaces*, 2019, **11**, 29056–29064.
111 X. X. Zhang, F. Wang, L. Dou, X. T. Cheng, Y. Si, J. Y. Yu and B. Ding, *ACS Nano*, 2020, **14**, 15616–15625.
112 H. Jin, N. Matsuhisa, S. Lee, M. Abbas, T. Yokota and T. Someya, *Adv. Mater.*, 2017, **29**, 1605848.
113 M. Liu, X. Pu, C. Jiang, T. Liu, X. Huang, L. Chen, C. Du, J. Sun, W. Hu and Z. Wang, *Adv. Mater.*, 2017, **29**, 1703700.
114 X. Wang, L. Dong, H. Zhang, R. Yu, C. Pan and Z. L. Wang, *Adv. Sci.*, 2015, **2**, 1500169.
115 C. F. Wang, C. H. Wang, Z. L. Huang and S. Xu, *Adv. Mater.*, 2018, **30**, 1801368.
116 X. Hou, R. Zhang and D. Fang, *Ceram. Int.*, 2020, **46**, 2122–2127.
117 T. Xu, Y. C. Ding, Z. Wang, Y. Zhao, W. D. Wu, H. Fong and Z. T. Zhu, *J. Mater. Chem. C*, 2017, **5**, 10288–10294.
118 H. Liu, X. Y. Chen, Y. J. Zheng, D. B. Zhang, Y. Zhao, C. F. Wang, C. F. Pan, C. T. Liu and C. Y. Shen, *Adv. Funct. Mater.*, 2021, **31**, 2008006.
119 L. Wang, M. Y. Zhang, B. Yang, J. J. Tan and X. T. Ding, *ACS Nano*, 2020, **14**, 10633–10647.
120 Q. F. Yao, B. T. Fan, Y. Xiong, C. Wang, H. W. Wang, C. D. Jin and Q. F. Sun, *Carbohydr. Polym.*, 2017, **168**, 265–273.
121 Z. Qin, Y. H. Lv, X. H. Fang, B. Zhao, F. X. Niu, L. Z. Min and K. Pan, *Chem. Eng. J.*, 2022, **427**, 131650.
122 K. Y. Lee, J. Chun, J. H. Lee, K. N. Kim, N. R. Kang, J. Y. Kim, M. H. Kim, K. S. Shin, M. K. Gupta, J. M. Baik and S. W. Kim, *Adv. Mater.*, 2014, **26**, 5037.
123 X. He, X. Mu, Q. Wen, Z. Wen, J. Yang, C. Hu and H. Shi, *Nano Res.*, 2016, **9**, 3714.
124 F. R. Fan, Z. Q. Tian and Z. L. Wang, *Nano Energy*, 2012, **1**, 328–334.
125 W. G. Kim, D. W. Kim, I. W. Tcho, J. K. Kim, M. S. Kim and Y. K. Choi, *ACS Nano*, 2021, **15**, 258–287.
126 K. Shi, H. Zou, B. Sun, P. Jiang, J. He and X. Huang, *Adv. Funct. Mater.*, 2020, **30**, 1904536.
127 Q. Zheng, L. Fang, H. Guo, K. Yang, Z. Cai, M. A. B. Meador and S. Gong, *Adv. Funct. Mater.*, 2018, **28**, 1706365.
128 H. Y. Mi, X. Jing, Q. Zheng, L. Fang, H. X. Huang, L. S. Turng and S. Gong, *Nano Energy*, 2018, **48**, 327–336.
129 H. Y. Mi, H. Li, X. Jing, P. Hee, P. Y. Feng, X. M. Tao, Y. J. Liu, C. T. Liu and C. Y. Shen, *Ind. Eng. Chem. Res.*, 2020, **59**, 12399–12408.
130 H. Y. Mi, X. Jing, Z. Cai, Y. Liu, L. S. Turng and S. Gong, *Nanoscale*, 2018, **10**, 23131–23140.
131 L. Odochian, C. Moldoveanu and G. Carja, *Thermochim. Acta*, 2013, **558**, 22–28.
132 X. D. Hu, S. E. Jenkins, B. G. Min, M. B. Polk and S. Kumar, *Macromol. Mater. Eng.*, 2003, **288**, 823–843.
133 Z. C. Qian, R. Li, J. Guo, Z. Wang, X. F. Li, C. C. Li, N. Zhao and J. Xu, *Nano Energy*, 2019, **64**, 103900.
134 W. Raza, F. Ali, N. Raza, Y. W. Luo, E. E. Kwon, J. H. Yang, S. Kumar, A. Mehmood and K. Kim, *Nano Energy*, 2018, **52**, 441–473.
135 S. Chu, Y. Cui and N. Liu, *Nat. Mater.*, 2017, **16**, 16–22.

136 F. Li, J. Chen, X. Wang, M. Xue and G. Chen, *Adv. Funct. Mater.*, 2015, **25**, 4601–4606.
137 L. Sorensen, G. F. Strouse and A. E. Stiegman, *Adv. Mater.*, 2006, **18**, 1965–1967.
138 P. S. Kumar, J. Sundaramurthy, S. Sundarrajan, V. J. Babu, G. Singh, S. I. Allakhverdiev and S. Ramakrishna, *Energy Environ. Sci.*, 2014, **7**, 3192–3222.
139 G. G. Duan, S. H. Jiang, V. Jérôme, J. H. Wendorff, A. Fathi, J. Uhm, V. Altstädt, M. Herling, J. Breu, R. Freitag, S. Agarwal and A. Greiner, *Adv. Funct. Mater.*, 2015, **25**, 2850–2856.
140 H. Pang, Y. Z. Zhang, W. Y. Lai, Z. Hu and W. Huang, *Nano Energy*, 2015, **15**, 303–312.
141 H. Y. Sun, Z. Xu and C. Gao, *Adv. Mater.*, 2013, **25**, 2554–2560.
142 F. L. Lai, Y. E. Miao, Y. P. Huang, L. Z. Zuo, H. H. Gu, Y. E. Miao and T. X. Liu, *J. Mater. Chem. A*, 2016, **4**, 15861–15869.
143 L. Y. Xia, X. L. Li, Y. Q. Wu, S. H. Hua, Y. Liao, L. Huang, Y. Qing and X. H. Lu, *Chem. Eng. J.*, 2020, **379**, 122325.
144 H. Chen, T. Liu, J. R. Mou, W. J. Zhang, Z. J. Jiang, J. Liu, J. L. Huang and M. L. Liu, *Nano Energy*, 2019, **63**, 103836.
145 X. F. Lu, C. Wang, F. Favier and N. Pinna, *Adv. Energy Mater.*, 2017, **7**, 1601301.
146 M. Zhang, D. Z. Yang, S. Y. Zhang, T. Xu, Y. Z. Shi, Y. X. Liu, W. Chang and Z. Z. Yu, *Carbon*, 2020, **158**, 873–884.
147 J. C. Shu, W. Q. Cao and M. S. Cao, *Adv. Funct. Mater.*, 2021, **31**, 2100470.
148 C. Wan and J. Li, *Carbohydr. Polym.*, 2017, **161**, 158–165.
149 Y. Fei, M. Liang, L. W. Yan, Y. Chen and H. W. Zou, *Chem. Eng. J.*, 2020, **392**, 124815.
150 Y. Q. Du, J. Xu, J. Y. Fang, Y. T. Zhang, X. Y. Liu, P. Y. Zuo and Q. X. Zhuang, *J. Mater. Chem. A*, 2022, **10**, 6690–6700.
151 Y. J. Wan, P. L. Zhu, S. H. Yu, R. Sun, C. P. Wong and W. H. Liao, *Small*, 2018, **14**, 1800534.
152 Z. Zeng, T. Wu, D. Han, Q. Ren, G. Siqueira and G. Nyström, *ACS Nano*, 2020, **14**, 2927–2938.
153 Z. Q. Lu, F. F. Jia, L. H. Zhuo, D. D. Ning, K. Gao and F. Xie, *Composites, Part B*, 2021, **217**, 108853.
154 H. D. Huang, C. Y. Liu, D. Zhou, X. Jiang, G. J. Zhong, Di. X. Yan and Z. M. Li, *J. Mater. Chem. A*, 2015, **3**, 4983–4991.
155 S. Bolisetty, M. Peydayesh and R. Mezzenga, *Chem. Soc. Rev.*, 2019, **48**, 463–487.
156 R. Das, C. D. Vecitis, A. Schulze, B. Cao, A. F. Ismail, X. Lu, J. Chen and S. Ramakrishna, *Chem. Soc. Rev.*, 2017, **46**, 6946–7020.
157 H. I. Syeda and P. S. Yap, *Sci. Total Environ.*, 2022, **807**, 150606.
158 J. R. She, C. H. Tian, Y. Q. Wu, X. J. Li, S. Luo, Y. Qing and Z. Jiang, *J. Nanosci. Nanotechnol.*, 2018, **18**, 4167–4175.
159 T. Xu, Z. Wang, Y. C. Ding, W. H. Xu, W. D. Wu, Z. T. Zhu and H. Fong, *Carbohydr. Polym.*, 2018, **179**, 164–172.
160 L. T. Zhu, L. Zong, X. C. Wu, M. J. Li, H. S. Wang, J. You and C. X. Li, *ACS Nano*, 2018, **12**, 4462–4468.
161 G. D. Zhao, H. J. Zhao, L. Shi, B. W. Cheng, X. L. Xu and X. P. Zhuang, *Sep. Purif. Technol.*, 2021, **274**, 119054.
162 G. D. Zhao, H. J. Zhao, L. Shi, B. W. Cheng, X. L. Xu and X. P. Zhuang, *J. Colloid Interface Sci.*, 2021, **600**, 403–411.
163 Z. C. He, F. Wu, S. J. Guan, L. Liu, J. Li and Y. D. Huang, *J. Mater. Chem. A*, 2021, **9**, 13320–13331.
164 L. Q. Xue, J. Ren, S. G. Wang, D. H. Qu, Z. L. Wei, Q. B. Yang and Y. X. Li, *J. Porous Mater.*, 2020, **27**, 1589–1599.
165 A. K. Kota, G. Kwon, W. Choi, J. M. Mabry and A. Tuteja, *Nat. Commun.*, 2012, **3**, 1025.
166 W. Zhang, Y. Zhu, X. Liu, D. Wang, J. Li, L. Jiang and J. Jin, *Angew. Chem., Int. Ed.*, 2014, **53**, 856–860.
167 M. Chhajed, C. Yadav, A. K. Agrawal and P. K. Maji, *Carbohydr. Polym.*, 2019, **226**, 115286.
168 A. Qiao, R. L. Huang, A. Penkova, W. Qi, Z. M. He and R. X. Su, *Sep. Purif. Technol.*, 2022, **295**, 121266.
169 X. Jin, A. Al-Qatatsheh, K. Subhani and N. V. Salim, *Chem. Eng. J.*, 2021, **412**, 128635.
170 Y. H. Guan, F. Q. Cheng and Z. H. Pan, *Polymers*, 2019, **11**, 806.
171 H. Liu, X. Y. Chen, Y. J. Zheng, D. B. Zhang, Y. Zhao, C. F. Wang, C. F. Pan, C. T. Liu and C. Y. Shen, *Adv. Funct. Mater.*, 2021, **31**, 2008006.
172 Y. Si, Q. X. Fu, X. Q. Wang, J. Zhu, J. Y. Yu, G. Sun and B. Ding, *ACS Nano*, 2015, **9**, 3791–3799.
173 Y. Shen, D. W. Li, L. L. Wang, Y. Q. Zhou, F. Liu, H. P. Wu, B. Y. Deng and Q. S. Liu, *ACS Appl. Mater. Interfaces*, 2021, **13**, 20489–20500.
174 M. H. Tai, B. Y. L. Tan, J. Juay, D. D. Sun and J. O. Leckie, *Chem. - Eur. J.*, 2015, **21**, 5395–5402.
175 F. Deuber, S. Mousavi, L. Federer and C. Adlhart, *Adv. Mater. Interfaces*, 2017, **4**, 1700065.
176 S. S. Long, Y. C. Feng, Y. Z. Liu, L. L. Zheng, L. H. Gan, J. Liu, X. H. Zeng and M. N. Long, *Sep. Purif. Technol.*, 2021, **254**, 117577.
177 L. J. Zhou and Z. Y. Xu, *J. Hazard. Mater.*, 2020, **388**, 121804.
178 H. Ghasemi, G. Ni, A. Marconnet, J. Loomis, S. Yerci, N. Miljkovic and G. Chen, *Nat. Commun.*, 2014, **5**, 4449.
179 Y. Liu, S. Yu, R. Feng, A. Bernard, Y. Liu, Y. Zhang, H. Duan, W. Shang, P. Tao, C. Song and T. Deng, *Adv. Mater.*, 2015, **27**, 2768–2774.
180 L. Zhang, B. Tang, J. Wu, R. Li and P. Wang, *Adv. Mater.*, 2015, **27**, 4889–4894.
181 X. Z. Hu and J. Zhu, *Adv. Funct. Mater.*, 2020, **30**, 1907234.
182 B. Wicklein, A. Kocjan, G. Salazar-Alvarez, F. Carosio, G. Camino, M. Antonietti and L. Bergström, *Nat. Nanotechnol.*, 2015, **10**, 277–283.
183 Y. Liu, H. J. Liu, J. Xiong, A. L. Li, R. W. Wang, L. M. Wang, X. H. Qin and J. Y. Yu, *Chem. Eng. J.*, 2022, **427**, 131539.
184 H. X. Li, H. F. Wen, J. Lia, J. C. Huang, D. Wang and B. Z. Tang, *ACS Appl. Mater. Interfaces*, 2020, **12**, 26033–26040.
185 T. Mei, J. H. Chen, Q. H. Zhao and D. Wang, *ACS Appl. Mater. Interfaces*, 2020, **12**, 42686–42695.
186 L. Shi, K. Sun, G. Y. Zhang, M. Jiang, X. L. Xu and X. P. Zhuang, *J. Colloid Interface Sci.*, 2022, **624**, 377–384.